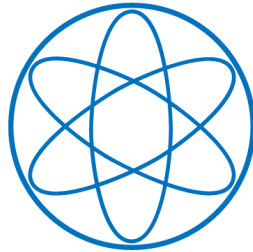


LEHRSTUHL E15  
PHYSIK - DEPARTMENT



Low-background gamma  
spectroscopy for the neutrino  
oscillation experiment  
**DOUBLE CHOOZ**

DIPLOMARBEIT

MARTIN HOFMANN

20. NOVEMBER 2007



TECHNISCHE UNIVERSITÄT  
MÜNCHEN



*The worthwhile problems are the ones  
you can really solve or help solve,  
the ones you can really contribute something to.*

- RICHARD FEYNMAN



## Abstract

Since the postulation of the neutrino by Wolfgang Pauli in 1930 and its first direct observation achieved by Clyde Cowan and Frederick Reines in 1956, neutrino physics has made great strides. Nowadays the focus is no longer on the mere understanding of the underlying physical processes, but precision experiments quantifying the last unknown parameters of the theory are performed. Many experimentally observed phenomena, like the lack of solar electron neutrinos or the dependence of the atmospheric  $\nu_\mu$ -flux on the zenith angle, are known to be caused by neutrino oscillations, the periodical change of flavour during the propagation of the neutrinos in space. Today the enhanced understanding of Pauli's "ghost particle" and its properties provide the opportunity to use neutrinos as a new and unique probe in a huge variety of fields, amongst them astrophysics, geophysics and cosmology.

In Chapter 1 the role of the neutrinos in the standard model of particle physics is briefly described. The neutrino oscillation formula and experiments having measured some of the oscillation parameters are discussed. Finally, the focus will be on possible experiments, which are able to determine the still unknown third mixing angle  $\vartheta_{13}$ .

One of these experiments, DOUBLE CHOOZ, and its physics program is presented in more detail in Chapter 2. DOUBLE CHOOZ uses low-energetic electron antineutrinos from a nuclear power plant to search for neutrino oscillations due to  $\vartheta_{13}$  on a baseline of 1050 metres. The detector concept foresees two identical detectors, a near detector for monitoring the electron antineutrino flux and its spectral shape and a far detector, measuring the effects of neutrino oscillations on this flux and its shape. The intended sensitivity of DOUBLE CHOOZ is  $\sin^2(2\vartheta_{13}) \leq 0.03$  after three years of data taking.

Chapter 3 gives an overview of the detector system used for low-background gamma spectroscopy. This system consists of a germanium detector with a relative efficiency of 150.5% and an energy resolution of 2.189 keV at 1.33 MeV (measured with an analogue main amplifier with a shaping time constant of 8  $\mu$ s). For background reduction the germanium detector is surrounded by several active and passive shieldings, amongst them an active muon-veto and an anti-Compton veto system. The whole detector system is located in the underground laboratory of the Technische Universität München in Garching. The balancing procedure for the anti-Compton veto, consisting of sodium-iodide scintillation crystals with PMTs, is presented, as well as the calibration of the plastic scintillator panels used as muon-veto. Finally, the designed NIM-based analogue read-out electronics is described

and compared to the newly installed digital signal processor system DSP 9660A, which replaces the analogue main amplifier and ADC. With this new system an unrivalled energy resolution of 1.764 keV at 1.33 MeV could be achieved.

The Monte Carlo simulation, developed for a determination of the detector efficiency, will be presented in Chapter 4. It is based on the software package GEANT4 from CERN and includes all relevant particles and interactions. Measurements with calibration sources have been done in order to test the simulation for its accuracy. The comparison between the simulated and the measured values showed, that the simulation is rather accurate for gamma energies above  $\sim 200$  keV, but suffers from some problems for low-energetic gamma rays.

Chapter 5 finally focuses on the results of the low-background gamma spectroscopy measurements. Long-term measurements without any artificial source were performed in order to determine the experimental background. Samples of the liquid scintillator LAB, the mineral oil tetradecane and the wave-length shifters PPO and bisMSB were investigated concerning their concentration of radioactive isotopes. These samples concern materials, which are intended to be used in the DOUBLE CHOOZ experiment. Therefore the investigation is of high importance, as radioactivity of the detector components poses one of the most important sources of accidental background in DOUBLE CHOOZ. For the isotopes from the  $^{238}\text{U}$ -, the  $^{232}\text{Th}$ - and the  $^{235}\text{U}$ -decay chains, as well as for  $^{40}\text{K}$ , upper limits on the mass concentrations have been found to be in the order of  $10^{-9}$  g/g for all investigated samples, in the case of  $^{40}\text{K}$  in LAB and tetradecane, as well as  $^{235}\text{U}$  in LAB even  $10^{-10}$  g/g. These results implicate, that both wave-length shifters can be used for the muon veto system of the DOUBLE CHOOZ detectors without any additional purification. Furthermore, the mass concentration of  $^{40}\text{K}$  in bisMSB allows its utilisation in the inner volumes of the detector (neutrino target and gamma catcher). The upper limits on the mass concentrations obtained for the organic liquids are above the allowed concentrations in DOUBLE CHOOZ, hence no conclusions can be given yet, whether purification is necessary or not. Some possible updates for future measurements are discussed, leading to an improvement of the reachable sensitivity.

# Contents

<b>1</b>	<b>Introduction: The standard model of particle physics &amp; neutrino oscillations</b>	<b>1</b>
1.1	The fundamental particles and forces . . . . .	1
1.2	Neutrino oscillations . . . . .	5
1.2.1	Theoretical derivation of the oscillation formula . . . . .	5
1.2.2	Already known oscillation parameters and their measurement . . . . .	8
1.2.3	Possible experiments to determine $\vartheta_{13}$ . . . . .	13
<b>2</b>	<b>The DOUBLE CHOOZ Experiment</b>	<b>17</b>
2.1	Neutrino physics with DOUBLE CHOOZ: Signal and background . . . . .	17
2.2	Detector site & setup . . . . .	21
<b>3</b>	<b>Detector setup and calibration for low-background gamma spectroscopy</b>	<b>25</b>
3.1	The detector system at a glance . . . . .	25
3.2	The germanium detector . . . . .	27
3.3	Anti-Compton veto . . . . .	30
3.3.1	General layout and working principle . . . . .	30
3.3.2	Calibration and balancing procedure . . . . .	31
3.4	Muon-veto system . . . . .	37
3.4.1	Overview of the setup . . . . .	37
3.4.2	Calibration . . . . .	39
3.5	Read-out electronics for signal processing . . . . .	42
3.5.1	Analogue part of the electronics . . . . .	42
3.5.2	Digital signal processing with the DSP 9660A . . . . .	46
<b>4</b>	<b>Monte-Carlo Simulation for the determination of the detector efficiency</b>	<b>49</b>
4.1	The source code . . . . .	49

---

4.2	Simulated detector efficiencies versus measured values . . . . .	51
<b>5</b>	<b>Results and discussion of the low-background gamma spectroscopy</b>	<b>61</b>
5.1	Ambient background activity . . . . .	61
5.2	Performed measurements and results . . . . .	66
5.2.1	Investigated samples . . . . .	66
5.2.2	Calculation of radioactivities . . . . .	75
5.3	Discussion of the results . . . . .	86
5.3.1	General discussion of the results . . . . .	86
5.3.2	Consequences for the DOUBLE CHOOZ experiment . . . . .	88
<b>6</b>	<b>Conclusion &amp; Outlook</b>	<b>93</b>
<b>A</b>	<b>Balancing of the anti-Compton veto</b>	<b>99</b>
<b>B</b>	<b>Calibration of the muon-veto system</b>	<b>105</b>
<b>C</b>	<b>Simulation of an isotropic source</b>	<b>109</b>
<b>D</b>	<b>Gamma lines</b>	<b>113</b>
<b>E</b>	<b>Decay chains</b>	<b>117</b>
<b>F</b>	<b>Decay schemes of selected isotopes</b>	<b>123</b>
<b>G</b>	<b>Glossar</b>	<b>127</b>
	<b>List of Figures</b>	<b>130</b>
	<b>List of Tables</b>	<b>132</b>
	<b>Bibliography</b>	<b>133</b>

# Chapter 1

## Introduction: The standard model of particle physics & neutrino oscillations

### 1.1 The fundamental particles and forces

In the standard model of particle physics all the matter consists of 12 different elementary particles [Alt05a, Hal84], which are listed in Tab. 1.1.

<i>1. Generation</i>	<i>2. Generation</i>	<i>3. Generation</i>
LEPTONS		
$\nu_e$ electron neutrino	$\nu_\mu$ muon neutrino	$\nu_\tau$ tau neutrino
$e^-$ electron	$\mu^-$ muon	$\tau^-$ tau
QUARKS		
$u$ up quark	$c$ charm quark	$t$ top quark
$d$ down quark	$s$ strange quark	$b$ bottom quark

Table 1.1: *The 12 fundamental fermions grouped into three generations. Only the particles from the first generation are stable, those from the second and third generation decay with the lifetime given in Tab. 1.2.*

These fundamental components of matter are the quarks, appearing in three different colours and making up the hadronic matter, and the leptons.

All of them have spin  $\frac{1}{2}$  (they are fermions described by Fermi-Dirac statistics) and can be grouped into three generations, also called "families", according to increasing mass<sup>1</sup>. Their properties are displayed in table 1.2. The stable matter surrounding and including ourselves is made up of particles of the first generation<sup>2</sup>.

To each fermion there is an antifermion with same mass and lifetime but opposite electrical charge, colour and third component of weak isospin.

Besides these fermionic fields there exist also the gauge bosons mediating the four fundamental forces, see tables 1.3 and 1.4: the electromagnetic and the weak interaction, which can be unified to the electroweak interaction (the so-called Glashow-Salam-Weinberg mechanism; [Ait89, Alt05a, Wei74]), the strong interaction described by the theory of quantum chromodynamics (QCD; cf. [Ait89, Alt05a]) and the gravitation, which is normally not regarded in the standard model.

While the gravitation and the weak interaction act on all types of fermions, the electromagnetic forces do not affect the uncharged neutrinos and the strong interaction only couples to coloured particles, i.e. the quarks, not to leptons.

Within the standard model there exists also one so far not experimentally identified particle, the Higgs boson with spin 0, being the mediator of the particle rest masses [Ait89, Alt05a, Sch95].

---

<sup>1</sup>Here and in the following  $\hbar = c = 1$  is used. The masses are, for example, given in units of energy.

<sup>2</sup>The situation is a bit more difficult for the neutrinos: as will be explained in chapter 1.2, the flavour eigenstates are not equal to the mass eigenstates. For massive neutrinos only the lightest mass eigenstate is stable, the other ones decay, e.g.  $\nu_3 \rightarrow \nu_1 + \gamma$ , where  $\nu_i$  denotes the mass eigenstates and  $\nu_1$  is assumed to be the lightest one (normal hierarchy) [Obe92].

PROPERTIES OF THE LEPTONS AND QUARKS					
particle	mass	life time	charge	weak isospin	colour
$\nu_{e,L}$	$< 2.2 \text{ eV}$	$> 7 \cdot 10^9 \text{ s/eV}$	0	$(1/2, +1/2)$	0
$e_L^-$	511 keV	stable	-1	$(1/2, -1/2)$	0
$\nu_{\mu,L}$	$< 0.18 \text{ MeV}$	$> 7 \cdot 10^9 \text{ s/eV}$	0	$(1/2, +1/2)$	0
$\mu_L^-$	105.7 MeV	2.2 $\mu\text{s}$	-1	$(1/2, -1/2)$	0
$\nu_{\tau,L}$	$< 18.2 \text{ MeV}$	$> 7 \cdot 10^9 \text{ s/eV}$	0	$(1/2, +1/2)$	0
$\tau_L^-$	1777 MeV	290 fs	-1	$(1/2, -1/2)$	0
$e_R^-$	511 keV	stable	-1	$(0, 0)$	0
$\mu_R^-$	105.7 MeV	2.2 $\mu\text{s}$	-1	$(0, 0)$	0
$\tau_R^-$	1777 MeV	290 fs	-1	$(0, 0)$	0
$u_L$	$\sim 5 \text{ MeV}$		2/3	$(1/2, +1/2)$	r,g,b
$d_L$	$\sim 7 \text{ MeV}$		-1/3	$(1/2, -1/2)$	r,g,b
$c_L$	$\sim 1.4 \text{ GeV}$		2/3	$(1/2, +1/2)$	r,g,b
$s_L$	$\sim 150 \text{ MeV}$		-1/3	$(1/2, -1/2)$	r,g,b
$t_L$	174 GeV		2/3	$(1/2, +1/2)$	r,g,b
$b_L$	$\sim 4.5 \text{ GeV}$		-1/3	$(1/2, -1/2)$	r,g,b
$u_R$	$\sim 5 \text{ MeV}$		2/3	$(0, 0)$	r,g,b
$d_R$	$\sim 7 \text{ MeV}$		-1/3	$(0, 0)$	r,g,b
$c_R$	$\sim 1.4 \text{ GeV}$		2/3	$(0, 0)$	r,g,b
$s_R$	$\sim 150 \text{ MeV}$		-1/3	$(0, 0)$	r,g,b
$t_R$	174 GeV		2/3	$(0, 0)$	r,g,b
$b_R$	$\sim 4.5 \text{ GeV}$		-1/3	$(0, 0)$	r,g,b

Table 1.2: *Properties of the fundamental fermions. The last three columns exhibit the generalised charges: electric charge, weak isospin as charge of the weak interaction and colour as charge of the strong interaction. The weak interaction is parity violating and acts differently on lefthanded and righthanded particles, where the lefthanded ones can be combined to doublets, while the righthanded ones are singlets. In the standard model neutrinos are considered as massless and appear only as lefthanded particles. The mass limits given in this table for the different neutrino flavours are obtained in direct (kinematic) measurements. From neutrino oscillations (see chapter 1.2) it is known, that neutrinos are massive. Therein, the boundaries on the masses are much more stringent: for the mass eigenvalues of the neutrinos one has  $m_1 < 2.2 \text{ eV}$ ,  $9 \text{ meV} < m_2 < 2.2 \text{ eV}$  and  $51 \text{ meV} < m_3 < 2.2 \text{ eV}$  (in normal hierarchy). All data taken from [PDG07].*

<i>Inter- action</i>	<b>strong</b>	<b>electro- magnetic</b>	<b>weak</b>	<b>Gravi- tation</b>
<i>Relative strength (at low energies)</i>	1	$10^{-3}$	$10^{-5}$	$10^{-38}$
<i>Range</i>	1 fm	$\infty$	$10^{-3}$ fm	$\infty$
<i>acts on</i>	quarks & gluons	all charged particles	quarks, leptons (except $\nu_R$ ), $W^\pm$ , $Z^0$ , Higgs	all particles
<i>Gauge boson</i>	8 gluons (g)	photon ( $\gamma$ )	$W^\pm$ , $Z^0$	graviton
<i>Theory</i>	Quantum chromo- dynamics (QCD)	Quantum electro- dynamics (QED)	Glashow- Salam- Weinberg theory (GSW)	General Relativity (GRT)
<i>Gauge group</i>	$SU(3)_c$	$U(1)_Q$	$SU(2)_L \otimes$ $U(1)_Y$	-

Table 1.3: *The 12 different gauge bosons of the standard model as well as the Higgs boson and the graviton. These gauge bosons mediate the fundamental forces, described by the above-mentioned gauge theories. Only the gravitation could not be quantised yet as well as the graviton was not observed experimentally up to now.*

PROPERTIES OF THE BOSONS						
particle	spin	mass [GeV]	life time [s]	charge	weak isospin	colour
<i>photon</i>	1	0	stable	0	(0, 0)	0
$Z^0$	1	91	$2.6 \cdot 10^{-25}$	0	(1, 0)	0
$W^\pm$	1	80	$3.1 \cdot 10^{-25}$	$\pm 1$	(1, $\pm 1$ )	0
<i>gluon</i>	1	0		0	(0, 0)	$r\bar{g}, g\bar{r}, b\bar{r},$ $r\bar{b}, b\bar{g}, g\bar{b},$ $r\bar{r} - g\bar{g},$ $r\bar{r} + g\bar{g} - b\bar{b}$
<i>Higgs</i>	0	>114	?	0	$(\frac{1}{2}, -\frac{1}{2})$	0
<i>graviton</i>	2	0	stable?	0	(0, 0)?	0

Table 1.4: *Properties of the gauge bosons, including the hypothetical graviton and Higgs boson. The values for the weak isospin given for the photon and the  $Z^0$  are not quite correct, as these particles are an orthogonal mixture of  $B^0$  (weak isospin (0,0)) and the  $W_3$  (weak isospin (1,0)), cf. [Ait89, Wei74].*

## 1.2 Neutrino oscillations

### 1.2.1 Theoretical derivation of the oscillation formula

The three neutrinos named above ( $\nu_e, \nu_\mu, \nu_\tau$ ) are the eigenstates of the weak interaction, the so-called flavour eigenstates. From oscillation experiments<sup>3</sup> it is known that these flavour eigenstates are not identical to the mass eigenstates ( $\nu_1, \nu_2, \nu_3$ ). The mixing between these two is described by a mixing matrix, the Pontecorvo-Maki-Nakagawa-Sakata matrix (PMNS matrix) [Akh00, Akh06, Bil78, Bil99, Sch97]:

$$\begin{pmatrix} \nu_e \\ \nu_\mu \\ \nu_\tau \end{pmatrix} = \underbrace{\begin{pmatrix} U_{e1} & U_{e2} & U_{e3} \\ U_{\mu1} & U_{\mu2} & U_{\mu3} \\ U_{\tau1} & U_{\tau2} & U_{\tau3} \end{pmatrix}}_{PMNS - Matrix} \begin{pmatrix} \nu_1 \\ \nu_2 \\ \nu_3 \end{pmatrix} \quad (1.1)$$

<sup>3</sup>see section 1.2.2 on page 8.

$$\begin{aligned}
 \begin{pmatrix} U_{e1} & U_{e2} & U_{e3} \\ U_{\mu 1} & U_{\mu 2} & U_{\mu 3} \\ U_{\tau 1} & U_{\tau 2} & U_{\tau 3} \end{pmatrix} &= \begin{pmatrix} 1 & 0 & 0 \\ 0 & c_{23} & s_{23} \\ 0 & -s_{23} & c_{23} \end{pmatrix} \begin{pmatrix} c_{13} & 0 & s_{13}e^{-i\delta} \\ 0 & 1 & 0 \\ -s_{13}e^{i\delta} & 0 & c_{13} \end{pmatrix} \times \\
 &\times \begin{pmatrix} c_{12} & s_{12} & 0 \\ -s_{12} & c_{12} & 0 \\ 0 & 0 & 1 \end{pmatrix} \begin{pmatrix} e^{\frac{i}{2}\alpha_1} & 0 & 0 \\ 0 & e^{\frac{i}{2}\alpha_2} & 0 \\ 0 & 0 & 1 \end{pmatrix} \quad (1.2)
 \end{aligned}$$

The PMNS matrix contains three different mixing angles  $\vartheta_{ij}$  (in eq. (1.2)  $\sin(\vartheta_{ij})$  is abbreviated by  $s_{ij}$  and  $\cos(\vartheta_{ij})$  by  $c_{ij}$ ) between the three generations and one CP violating phase  $\delta$ . The two phases  $\alpha_1$  and  $\alpha_2$  in the last part of the PMNS matrix are the Majorana phases, which only occur in the case, that neutrinos are Majorana particles [Akh00, Doi81, Sch97]. These phases will be neglected in the following, as they do not play any role in the neutrino oscillation formula.

The mass eigenstates are responsible for the neutrino propagation and the flavour eigenstates for neutrino production and detection. Equation (1.1) can be written as

$$|\nu_\alpha\rangle = \sum_{i=1}^3 U_{\alpha i} |\nu_i\rangle, \quad (1.3)$$

where  $|\nu_\alpha\rangle$  denotes the flavour eigenstates ( $\alpha = e, \mu, \tau$ ),  $|\nu_i\rangle$  the mass eigenstates ( $i = 1, 2, 3$ ) and  $U_{\alpha i}$  the elements of the PMNS matrix. For antineutrinos the complex conjugated matrix elements  $U_{\alpha i}^*$  have to be taken. The time evolution of the mass eigenstates is given by the solution of the Dirac equation:

$$|\nu_i(t)\rangle = e^{-iE_i t} |\nu_i(t=0)\rangle \quad (1.4)$$

Hereby  $E_i$  stands for the energy of the neutrino given by

$$E_i = \sqrt{\vec{p}_i^2 + m_i^2} \stackrel{m_i \ll |\vec{p}_i|}{\approx} |\vec{p}_i| + \frac{m_i^2}{2|\vec{p}_i|} \stackrel{|\vec{p}_i| \approx E_{\nu_i}}{\approx} E_{\nu_i} + \frac{m_i^2}{2E_{\nu_i}} \quad (1.5)$$

Inserting equation (1.4) in eq. (1.3) gives the time evolution of the flavour eigenstate:

$$|\nu_\alpha(t)\rangle = \sum_{i=1}^3 U_{\alpha i} e^{-iE_i t} |\nu_i(t=0)\rangle \quad (1.6)$$

As the detection of a neutrino occurs via its weak eigenstate, one has to calculate the transition amplitude from the flavour eigenstate  $\nu_\alpha$  to  $\nu_\beta$  by projecting the result for  $|\nu_\alpha(t)\rangle$  (eq. (1.6)) on the flavour eigenstate  $\langle\nu_\beta|$ :

$$A_{\alpha\rightarrow\beta} = \langle\nu_\beta|\nu_\alpha(t)\rangle = \sum_{i,j=1}^3 U_{\alpha i} U_{\beta j}^* \delta_{ij} e^{-iE_i t} = \sum_{i=1}^3 U_{\alpha i} U_{\beta i}^* e^{-iE_i t} \quad (1.7)$$

To get the transition probability it is necessary to calculate  $|A_{\alpha\rightarrow\beta}|^2$ :

$$P(\nu_\alpha \rightarrow \nu_\beta) = |A_{\alpha\rightarrow\beta}|^2 = \sum_{i=1}^3 |U_{\alpha i} U_{\beta i}^*|^2 + 2 \Re \sum_{j>i} U_{\alpha i} U_{\beta i}^* U_{\alpha j}^* U_{\beta j} e^{-i\Delta_{ij}} \quad (1.8)$$

with

$$\Delta_{ij} = (E_i - E_j) t \approx \frac{m_i^2 - m_j^2}{2E} t \stackrel{L=t}{=} \Delta m_{ij}^2 \frac{L}{2E} \quad (1.9)$$

where  $L$  denotes the distance between source and detector<sup>4</sup>. Here a simplification was made: equations (1.8) and (1.9) are valid under the assumption that the different mass eigenstates have the same momentum. This assumption is not completely correct (see [Akh00] on p.22f). Correctly, eq. (1.4) has to be written as [Giu04]

$$|\nu_i(t)\rangle = e^{-iE_i t + ip_i L} |\nu_i(t=0)\rangle \quad (1.10)$$

Using the full formalism of quantum field theory, it can be shown [Giu04], that the approximation  $L=t$  is applicable for ultrarelativistic neutrinos. Thus the correct phase in eq. (1.10) becomes

$$p_i L - E_i t \approx (p_i - E_i) L = -\frac{E_i^2 - p_i^2}{E_i + p_i} L = -\frac{m_i^2}{E_i + p_i} L \stackrel{m_i \ll p_i}{\approx} -\frac{m_i^2}{2E} L \quad (1.11)$$

leading to exactly the same results as the "standard" derivation.

From equation (1.8) it can be seen, that if not all  $\Delta m_{ij}^2$  are equal zero (this implies massive neutrinos!) there exist oscillations between the different flavour eigenstates of the neutrinos. The amplitudes of these oscillations are given by the mixing angles  $\vartheta_{ij}$  (contained in the matrix elements  $U_{\alpha i}$ ) while the oscillation frequencies are determined by the mass square differences  $\Delta m_{ij}^2$ .

---

<sup>4</sup>Again  $c = 1$  was used.

### 1.2.2 Already known oscillation parameters and their measurement

From various experiments two mixing angles and the absolute values of the mass square differences are already known (table 1.5):

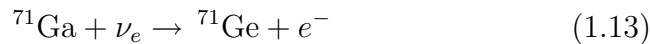
<i>Oscillation parameter</i>	<i>value (90% C.L.)</i>	<i>known from</i>
$\sin^2(2\vartheta_{12})$	$0.86^{+0.03}_{-0.04}$	<i>solar neutrinos, KamLAND</i>
$\sin^2(2\vartheta_{23})$	$> 0.92$	<i>K2K, atmospheric neutrinos</i>
$\Delta m_{21}^2$	$(8.0 \pm 0.3) \cdot 10^{-5} eV^2$	<i>KamLAND, solar neutrinos</i>
$\Delta m_{32}^2$	$(1.9 \text{ to } 3.0) \cdot 10^{-3} eV^2$	<i>Super-Kamiokande, MINOS</i>
$\sin^2(2\vartheta_{13})$	$< 0.19$	<i>CHOOZ</i>

Table 1.5: *The already known parameters characterizing neutrino oscillations, as well as the current best constraint on  $\vartheta_{13}$  from the CHOOZ experiment (for  $\Delta m_{32}^2 = 1.9 \cdot 10^{-3} eV^2$ ) [Apo99]. Due to the MSW effect in the sun [Akh00, Sch97] the sign of  $\Delta m_{21}^2$  is known to be positive, this means  $m_2$  is heavier than  $m_1$ . The sign of  $\Delta m_{32}^2$  and the value of the CP-violating phase  $\delta$  are still unknown. All data taken from [PDG07].*

- **Radiochemical Experiments:** The first hints for oscillations of solar neutrinos came from radiochemical experiments [Sch97]. These experiments use the electron neutrino capture on a target nucleus and obtain information on the electron neutrino flux by counting the number of reaction products in a certain measuring time. The first experiment, performed by Ray Davis, was the Chlorine solar neutrino experiment in the Homestake mine (4400 m.w.e.) [Cle98, Dav68]. It used 390 m<sup>3</sup> of liquid tetrachloroethylene (C<sub>2</sub>Cl<sub>4</sub>) as neutrino target. The essential reaction (with an energy threshold of 814 keV) is:



The three experiments **SAGE** (**S**oviet-**A**merican **G**allium **E**xperiment, [Aba91]), **GALLEX** (**G**allium **E**xperiment, [Ans92]) and its successor **GNO** (**G**allium **N**eutrino **O**bservatory, [Alt00, Alt05]) used the isotope  ${}^{71}\text{Ga}$ , which has a rather low energy threshold of 233 keV for electron-neutrino capture:



SAGE used metallic gallium, GALLEX and GNO a gallium chloride solution as neutrino target. The produced argon and germanium nuclei, respectively, are afterwards extracted from the chlorine/gallium with chemical methods. As  ${}^{37}\text{Ar}$  and  ${}^{71}\text{Ge}$  are unstable, the number of nuclei produced can be determined by measuring their decay using proportional counters. All these experiments published a deficit in the solar electron neutrino flux [Abd02, Alt05, Cle98, Ham99], which could finally be explained by neutrino oscillations with  $\sin^2(2\vartheta_{12}) = 0.89$ . The radiochemical experiments give only weak constraints on the mass square differences, as the neutrino flux is integrated over long measuring times.

- **KamLAND:** The **K**amioka **L**iquid Scintillator **A**nti **N**eutrino **D**etector (KamLAND, [Sue04]) is a 1 kiloton neutrino detector in the Kamioka underground mine (2700 m.w.e. overburden) near Toyama, Japan. It measured low-energy reactor antineutrinos from the surrounding nuclear power plants in Japan and South Korea with an average distance of 180 km. In 2002 a large neutrino deficit was found [Egu03], most likely explained by neutrino oscillations with  $\sin^2(2\vartheta_{12}) = 1$  and  $\Delta m_{21}^2 = 6.9 \cdot 10^{-5} \text{ eV}^2$ . This helped to verify the MSW LMA solution for solar neutrinos.
- **Super-Kamiokande:** KamLAND is not the only experiment in the Kamioka mine, but also the Super-Kamiokande detector is located there. Originally meant to search for proton decay (Kamiokande stands for **K**amioka **N**ucleon **D**ecay **E**xperiment) this 50 kiloton water Cherenkov detector became a very useful tool for neutrino physics [Ish04]. Since its completion in 1996 it measured mainly atmospheric neutrinos and solar  ${}^8\text{B}$  neutrinos. Due to its directional sensitivity Super-Kamiokande was able to take a picture of the sun in "neutrino light", which can be seen in figure 1.1.

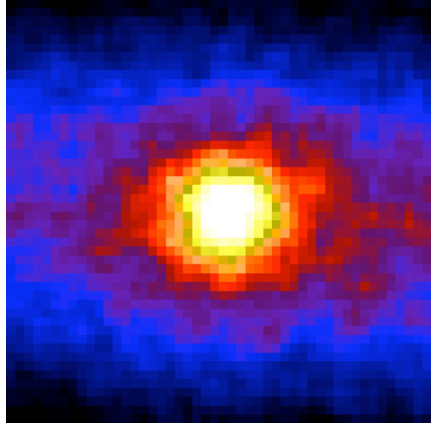


Figure 1.1: *Picture of the sun taken by the Super-Kamiokande detector in "neutrino light", from [Svo99].*

In a water Cherenkov detector neutrinos scatter off an electron via neutral weak interaction or create a fast lepton (electron or muon; tau leptons are in most cases too heavy to be produced) via charged weak interaction. If the velocity of this lepton exceeds the speed of light in water, it emits Cherenkov radiation detected by photomultiplier tubes. Detectors of this type have directional sensitivity but a rather high energy threshold.

The best fit to the Super-Kamiokande data is given by  $\sin^2(2\vartheta_{23}) = 1$  and  $\Delta m_{32}^2 = 2.5 \cdot 10^{-3} \text{ eV}^2$ .

- **K2K:** Super-Kamiokande does not only measure neutrinos from natural sources but also serves as target for a neutrino beam coming from the KEK accelerator facility in Tsubaka near Tokyo, which is 250 km away from the Kamioka mine [Ahn06] (K2K stands for **K**EK **t**o **K**amioka). The neutrino beam is an almost pure  $\nu_\mu$  beam, as the neutrinos are produced by decaying mesons:



These pions are produced by high-energetic protons ( $\sim 12 \text{ GeV}$ ) interacting in an aluminium target. Muons and remaining pions are finally absorbed in a beam dump.

K2K started operation in 1999 and has since that confirmed the Super-Kamiokande data. The best fit point within the physical region is  $(\Delta m_{32}^2, \sin^2(2\vartheta_{23})) = (2.8 \cdot 10^{-3} \text{ eV}^2, 1.0)$ .

- ***SNO***: In Ontario, Canada, the Sudbury Neutrino Observatory (SNO), a 1 kiloton heavy water Cherenkov detector is arranged in a nickel mine with a shielding of  $\sim 6000$  m.w.e. [Ahm02]. The usage of heavy water has a major advantage: Besides the elastic scattering off electrons, neutrinos can interact with the deuterium nuclei. While the neutral current interaction  $\nu_x + d \rightarrow p + n + \nu_x$  is possible for all neutrino flavours, the charged current interaction  $\nu_e + d \rightarrow 2p + e^-$  can only occur for electron neutrinos. For this reason it is possible to measure the whole neutrino flux coming from the sun, as well as solely the electron neutrino flux. Thus SNO was able to finally solve the solar neutrino problem in 2001.
- ***Borexino***: The Borexino detector in the Gran Sasso underground laboratory (overburden: 3500 m.w.e.) is a 300 ton liquid scintillator detector [Ali00] with the main aim to measure the  ${}^7\text{Be}$ -neutrino flux from the sun with an up to now unrivalled sensitivity. Borexino started data taking in May 2007 and recently first results on the  ${}^7\text{Be}$ -neutrino flux could be published [Bor07], being consistent with the predictions of the standard solar model and neutrino oscillations with MSW LMA parameters: Borexino measured  $47 \pm 7_{stat} \pm 12_{sys}$  counts per day and 100 tons of target mass in the relevant energy window, while one would expect  $49 \pm 4$  counts/day $\cdot$ 100 t from the theory. Without any neutrino oscillations the expectation value is  $75 \pm 4$  counts/day $\cdot$ 100 t. Borexino will be able to set further constraints on the solar neutrino oscillation parameters in the next years.
- ***MINOS***: Determining a very precise value of  $\Delta m_{32}^2$  was the major contribution to neutrino physics from the Main Injector Neutrino Oscillation Search (MINOS) experiment [Min07]: the best fit value is  $2.38 \cdot 10^{-3} \text{ eV}^2$ . Like K2K it also uses an accelerator as neutrino source, in this case Fermilab's NuMI  $\nu_\mu$  beam. The MINOS detector itself is split up into two parts: a near detector at Fermilab for beam monitoring and a far detector in the Soudan mine underground laboratory in Minnesota (baseline: 735 km). Both detectors are magnetized steel calorimeters with plastic scintillator layers for read-out.
- ***CHOOZ***: The current best constraint for  $\vartheta_{13}$  comes from the CHOOZ experiment, a reactor antineutrino disappearance experiment in France [Apo03]. CHOOZ used a 5-ton gadolinium loaded liquid scintillator target at a distance of  $\sim 1$  km to the reactor cores, shielded by 17 tons of buffer liquid, an active muon-veto and low-activity sand. After 16 months of data taking no evidence for neutrino oscillations in the

$\bar{\nu}_e$ -disappearance mode could be found leading to exclusion values of  $\Delta m_{32}^2 > 7 \cdot 10^{-4} \text{ eV}^2$  for maximum mixing and  $\sin^2(2\vartheta_{13}) > 0.1$  for large  $\Delta m_{32}^2$ , see fig. 1.2.

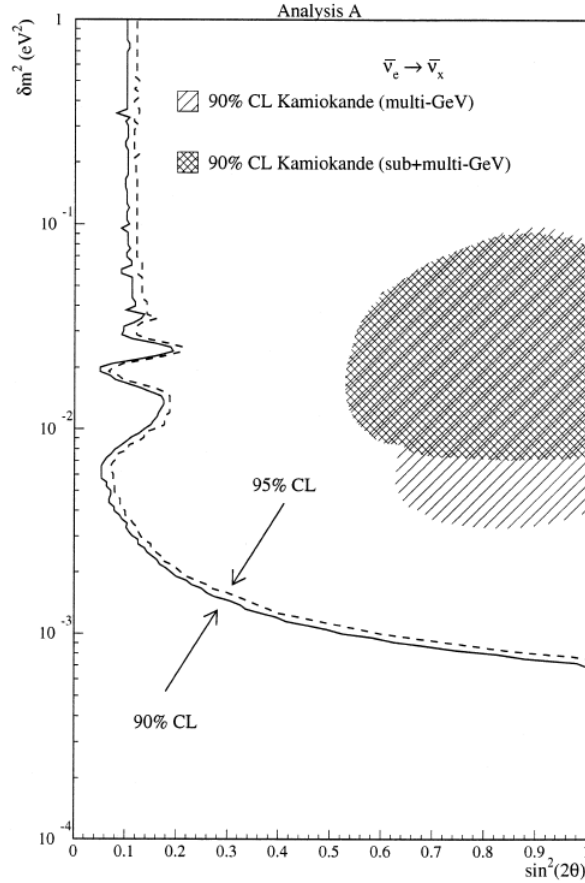


Figure 1.2: *Exclusion plot of the CHOOZ reactor neutrino experiment [Apo99], including the Kamiokande allowed region for  $\nu_\mu \rightarrow \nu_e$  oscillations [Fuk94].*

### 1.2.3 Possible experiments to determine $\vartheta_{13}$

The measurement of  $\vartheta_{13}$  is quite challenging as it is very small compared to the other two neutrino mixing angles. In the near future two ways to determine this last missing mixing angle look promising:

- ***Superbeam experiments:*** In the so-called superbeam long baseline experiments a very intensive neutrino or antineutrino beam from an accelerator laboratory is used for oscillation experiments. Such a beam mainly consists of high-energetic muon (anti)neutrinos, making appearance experiments with electron (anti)neutrinos possible. Using eq. (1.8) and including matter induced effects<sup>5</sup> the transition probability  $P(\nu_\mu \rightarrow \nu_e)$  is [Hub02]

$$\begin{aligned}
P(\nu_\mu \rightarrow \nu_e) &\simeq \sin^2(2\vartheta_{13}) \cdot \sin^2(\vartheta_{23}) \cdot \sin^2\beta \\
&\pm \alpha \cdot \sin(2\vartheta_{13}) \cdot \sin(\delta) \cdot \sin(2\vartheta_{12}) \cdot \\
&\quad \cdot \sin(2\vartheta_{23}) \cdot \beta \cdot \sin^2\beta \\
&- \alpha \cdot \sin(2\vartheta_{13}) \cdot \cos(\delta) \cdot \sin(2\vartheta_{12}) \cdot \\
&\quad \cdot \sin(2\vartheta_{23}) \cdot \beta \cdot \cos\beta \cdot \sin\beta \\
&+ \alpha^2 \cdot \cos^2(\vartheta_{23}) \cdot \sin^2(2\vartheta_{12}) \cdot \beta^2
\end{aligned} \tag{1.15}$$

where the abbreviations  $\alpha = \frac{\Delta m_{21}^2}{\Delta m_{32}^2}$  and  $\beta = \frac{\Delta m_{32}^2 L}{4E}$  as well as the approximations  $\cos(\vartheta_{13}) \approx 1$  and  $\sin(\alpha \cdot \beta) \approx \alpha \cdot \beta$  are used.  $L$  is again the distance between source and detector. In the second term the plus (minus) sign is valid for antineutrinos (neutrinos). Equation (1.15) shows clearly the interference of the oscillations between the three different mass eigenstates of the neutrinos.

From this formula can be seen, that superbeam experiments offer the opportunity to measure  $\vartheta_{13}$ , as well as  $\Delta m_{32}^2$ , the CP-violating phase  $\delta$ ,  $\vartheta_{23}$  and the mass hierarchy, that is the sign of  $\Delta m_{32}^2$ . But also a great disadvantage becomes clear: these experiments suffer from parameter correlations and degeneracies (solutions in the parameter space disconnected from the best-fit region [Hub02]). Changes in one parameter can always be compensated by changing another one in a different term of the sum. That is why it is of great interest to obtain additional information on  $\vartheta_{13}$  by another experimental method.

---

<sup>5</sup>The baselines of superbeam experiments are always secants through the earth.

Planned superbeam experiments are the **T2K** experiment (Tokai to Kamioka) in Japan [Oya05] and the **NuMI**-off-axis project (Neutrinos at Main Injector) in the US [Kop05]. The detector for T2K is the Super-Kamiokande water Cherenkov detector already described above. Source of the neutrino beam is the J-PARC 50 GeV proton synchrotron in JAEA, Tokai, which is 295 km away from the Kamioka mine. The experiment is planned to start in 2009. It is quite similar to the K2K project (see page 10), except for a higher beam energy (50 GeV primary proton energy instead of 12 GeV), a higher beam intensity (planned: two orders of magnitude larger than in K2K) and an off-axis beam configuration, that means the beam direction is adjusted to be  $2^\circ$  to  $3^\circ$  off the direct line of sight to the Super-Kamiokande detector. The off-axis beam provides a strong suppression of neutrinos with higher energies, which is desirable because for neutrino energies of  $\sim 1$  GeV the first oscillation maximum appears at 300 km, corresponding nearly exactly to the length of the baseline. Furthermore it is planned to build a near detector at a distance of 2 km to monitor the flux, spectrum and direction of the neutrino beam. The intended sensitivity of T2K after five years of measurement is  $\sin^2(2\vartheta_{13}) \approx 0.023$ .

The NuMI facility at Fermilab started operating in 2005 and has been delivering an intense  $\nu_\mu$  beam of variable energy (2-20 GeV) for different neutrino detectors, among them MINOS. It is planned to build a 30 kiloton off-axis liquid scintillator detector, **NO $\nu$ A** (NuMI Off-axis  $\nu_e$  Apppearance experiment), in Ash River, Minnesota with a baseline of  $\sim 810$  km. This far detector will be accompanied by a smaller near detector identical in structure for beam monitoring. Construction of the far detector shall be finished in 2010, that of the full detector in 2011 [Nov05].

- **Reactor neutrino experiments:** In a nuclear power plant the elements  $^{235}\text{U}$  and  $^{239}\text{Pu}$  are used for nuclear fission by thermal neutrons. Subsequently, fission products undergo beta decay because of their neutron excess. In these decays electron antineutrinos are released. These antineutrinos provide another possibility to measure  $\vartheta_{13}$ , due to their intensive flux and low energies (typically below 8 MeV) [Obe06]. The small energies as well as short baselines guarantee the absence of matter oscillation effects. However, the low energies of antineutrinos from nuclear power plants have a major disadvantage: As the energy is not sufficient to produce muons or tau leptons only disappearance experiments are possible.

Expanding formula (1.8) on page 7 for low energies and short baselines gives us the survival probability for an electron antineutrino as a function of the baseline  $L$  and the neutrino energy  $E$  [Bil01]:

$$\begin{aligned}
P(\bar{\nu}_e \rightarrow \bar{\nu}_e) &= 1 - 4 \cdot \sin^2 \vartheta_{13} \cdot \cos^2 \vartheta_{13} \cdot \sin^2 \left( \frac{\Delta m_{32}^2 L}{4E} \right) \\
&- \cos^4 \vartheta_{13} \cdot \sin^2(2\vartheta_{12}) \cdot \sin^2 \left( \frac{\Delta m_{21}^2 L}{4E} \right) \quad (1.16) \\
&+ 2 \sin^2 \vartheta_{13} \cdot \cos^2 \vartheta_{13} \cdot \sin^2 \vartheta_{12} \cdot \\
&\cdot \left( \cos \left( \frac{\Delta m_{32}^2 L}{2E} - \frac{\Delta m_{21}^2 L}{2E} \right) - \cos \left( \frac{\Delta m_{32}^2 L}{2E} \right) \right)
\end{aligned}$$

The second term in the first line of eq. (1.16) describes the atmospheric driven oscillations and is the most important term of the order of  $10^{-1}$  for typical values of  $L$  over  $E$  for reactor neutrino experiments. The second line in (1.16) includes the solar driven oscillations while the last contribution is an interference term between the first two. Both the second and the third contribution are of the order of  $10^{-3}$  and can be neglected to first approximation for short baselines  $L$ .

Equation (1.16) shows the great advantage of reactor neutrino experiments: to good approximation, the survival probability  $P(\bar{\nu}_e \rightarrow \bar{\nu}_e)$  is free from parameter correlations (e.g. with  $\delta$ ) as well as degeneracies. Together with the absence of matter effects this provides a clean measurement of  $\vartheta_{13}$ . Limiting factors in all reactor neutrino experiments are the statistical and systematical uncertainties.

For the next years, several reactor neutrino experiments are planned, among them the projects in Daya Bay and Angra. The Daya Bay reactor complex near Hong Kong, China, has, at present, four reactor cores with a total thermal power of 11.6 GW. The experimental concept foresees 3 different detector sites: two near detector sites to monitor the antineutrino flux and one far detector site (consisting of four identical detectors) for measuring  $\vartheta_{13}$  (910 m.w.e. overburden). All detectors will contain liquid scintillator, in each case 20 tons, as neutrino target. It is intended to have the system online end of 2010 and to reach a sensitivity of  $\sin^2(2\vartheta_{13}) < 0.01$  after 3 years of data taking [Day07].

Quite similar to the Daya Bay project is the proposed antineutrino detector at the Angra dos Reis nuclear reactor facility in Brazil with a total thermal power of 6 GW on two blocks. Angra is also intended

to have the common near and far liquid scintillator detector configuration as well as an additional one-ton very near detector (50 metres baseline) for cross checks. The far detector site will have an overburden of  $\sim 2000$  m.w.e. and will contain a 500 ton detector. Angra is planned to start data taking in 2013 and to reach a sensitivity down to  $\sin^2(2\vartheta_{13}) = 0.006$  [Anj05].

# Chapter 2

## The DOUBLE CHOOZ Experiment

### 2.1 Neutrino physics with DOUBLE CHOOZ: Signal and background

The most advanced reactor neutrino experiment<sup>1</sup> meant to measure  $\vartheta_{13}$  is DOUBLE CHOOZ in the French Ardennes [And04, Ard04, Ard06, Ber04, Obe06], see map in figure 2.1.

DOUBLE CHOOZ uses two liquid-scintillator underground detectors, one near detector for antineutrino flux monitoring and one far detector being sensitive on neutrino oscillations due to  $\vartheta_{13}$ . Figure 2.2 shows the survival probability  $P(\bar{\nu}_e \rightarrow \bar{\nu}_e)$  (equation (1.16) on page 15) for an electron antineutrino as a function of  $\frac{L}{E}$  for three different values of  $\Delta m_{32}^2$ , where L is the baseline and E the neutrino energy. The arrows indicate the positions of the two DOUBLE CHOOZ detectors.

The position of the far detector is chosen in such a manner, that the effects coming from neutrino oscillations due to  $\vartheta_{13}$  are (nearly) maximal, leading to the best possible sensitivity. At the location of the near detector all oscillation effects to good approximation can be neglected making a monitoring of the total antineutrino flux from the reactor feasible, as well as the determination of its spectral shape and time variations. The measurement of  $\vartheta_{13}$  does not only rely on the deviation of the energy-integrated flux from the  $1/r^2$  law at the location of the far detector, but also investigates the distortions of the antineutrino energy spectrum caused by the energy dependend oscillations. This improves the reachable sensitivity enormously.

---

<sup>1</sup>For a comparison between the different experiments see [Las06].



Figure 2.1: Map of northern France and southern Belgium. The red circle shows the location of the Chooz reactor site, where the DOUBLE CHOOZ experiment is being set up.

The intended sensitivity of DOUBLE CHOOZ is  $\sin^2(2\vartheta_{13}) \leq 0.03$  (at 90% C.L. for  $\Delta m_{32}^2 = 2.0 \cdot 10^{-3} \text{ eV}^2$ ) after three years of data taking [Ard06], see figure 2.3 on page 20.

In a liquid scintillator the electron antineutrinos can undergo inverse beta decay

$$\bar{\nu}_e + p^+ \rightarrow e^+ + n \quad (2.1)$$

with an energy threshold of 1.8 MeV. The reaction products, the positron and the neutron, are used for a delayed coincidence measurement. In the detector the energy deposited by the positron is the sum of its kinetic energy  $E_{e^+}$  and the energy of the gamma rays released after the annihilation with an electron<sup>2</sup>. Thus the energy of the positron signal exceeds at least 1 MeV,

<sup>2</sup>Annihilation in flight does not cause problems, as the detector works like a calorimeter and measures always the total energy of an event.

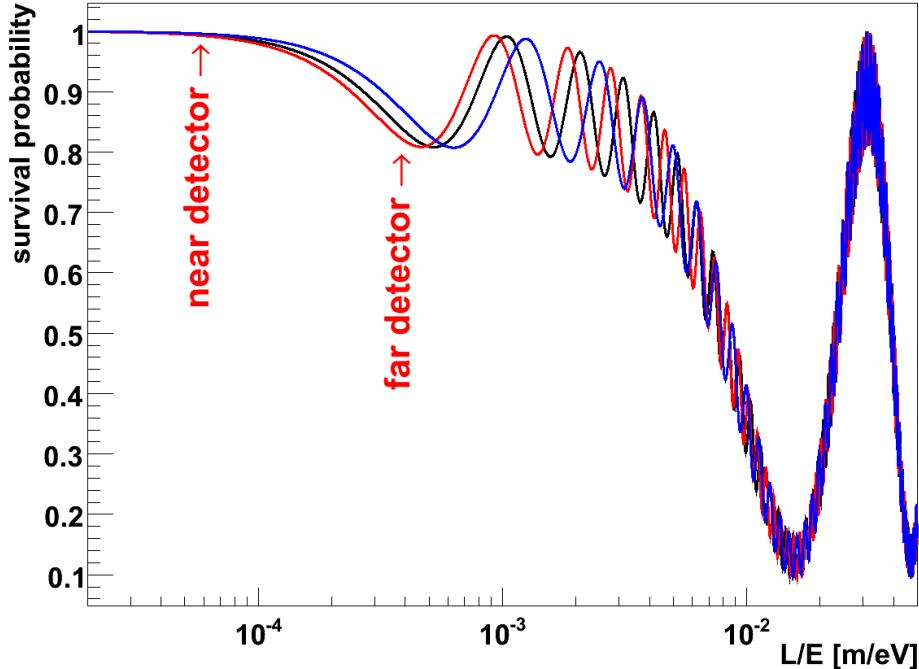
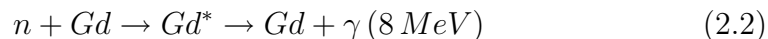


Figure 2.2: Probability for an electron antineutrino to be detected again as electron antineutrino plotted as a function of baseline  $L$  over neutrino energy  $E$  on a logarithmic scale. The positions of the two detectors are shown, too. The black curve shows the survival probability for  $\Delta m_{32}^2 = 2.4 \cdot 10^{-3} \text{ eV}^2$ , the blue curve for  $\Delta m_{32}^2 = 2.0 \cdot 10^{-3} \text{ eV}^2$  and the red one for  $\Delta m_{32}^2 = 2.7 \cdot 10^{-3} \text{ eV}^2$ . Plotted for  $\sin^2(2\vartheta_{13}) = 0.19$  (CHOOZ limit).

which can define a lower threshold for this event class and allows to exclude events below this threshold. This energy deposition happens quite fast and serves as prompt signal. A delayed coincidence signal occurs, when the produced neutron is captured by a gadolinium nucleus in the scintillator, releasing gamma quanta with a total energy of about 8 MeV and a mean multiplicity of  $\sim 3-4$ :



The time interval between these two signals is of the order of 2-100  $\mu\text{s}$ , while the spacing should be less than 1 metre [And04]. Using this method of delayed coincidence provides the opportunity to greatly reduce the number of background events.

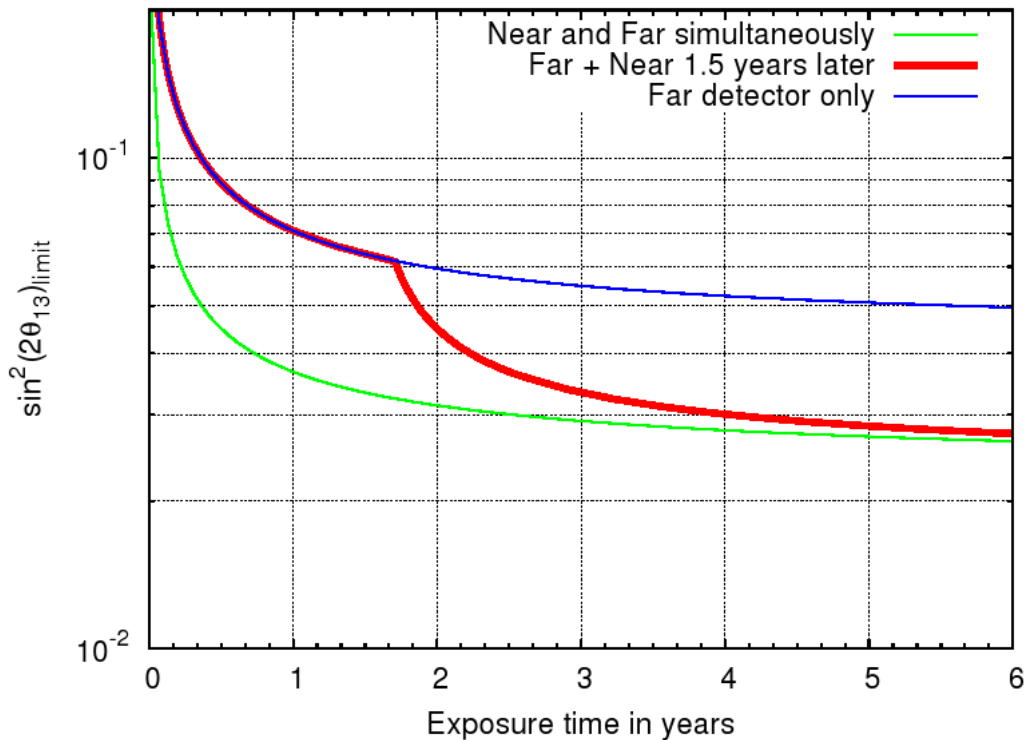


Figure 2.3: *Intended sensitivity of the DOUBLE CHOOZ project (red curve). At first the far detector will be set up. Roughly one and a half years later the near detector shall be finished, diminishing the systematic uncertainties and thus increasing the reachable sensitivity. From [Ard06].*

Measuring the total energy of the positron provides the needed information on the energy of the incoming electron antineutrino:

$$E_{\bar{\nu}_e} \simeq E_{e^+} + 511 \text{ keV} + (m_n - m_{p^+}) \quad (2.3)$$

Here the kinetic energy of the neutron was neglected, an approximation which is valid for small neutrino energies.

The reachable sensitivity in measuring  $\vartheta_{13}$  is limited by systematical and statistical uncertainties. While the latter can be reduced by increasing detector mass and measuring time, systematical errors are the main challenge for the detector design. Many of the uncertainties, the CHOOZ experiment [Apo03] suffered from, can be cancelled or greatly reduced by the utilization of the near detector, for example the uncertainty in the absolute reactor neutrino flux or of the cross section of the inverse beta decay. But one major contribution to the systematical error remains: background events mimicking

the antineutrino signal. This background can be separated into two classes, accidental background and correlated events.

Correlated background events are caused by cosmic muons. Muons not hitting the detector directly can produce fast neutrons in the surrounding rock material. These neutrons are able to enter the inner parts of the detector without being identified in the inner veto system as they are uncharged and do not deposit energy in the liquid scintillator. Finally in the neutrino target the neutrons can cause a proton recoil, mimicking the prompt positron signal (when in the right energy interval), and can then be captured on gadolinium. Such an event will be misidentified as neutrino event.

But also muons hitting the neutrino target directly and being identified correctly by the veto system might be harmful: they can produce long-lived unstable isotopes by spallation processes on the  $^{12}\text{C}$  nuclei of the liquid scintillator. Some of these isotopes, like  $^8\text{He}$ ,  $^9\text{Li}$  or  $^{11}\text{Li}$ , decay via  $\beta$ -n-cascades, producing exactly the same signature as an electron antineutrino. The major problem here is their long half-life (in the order of 100 ms or longer), which makes it impossible to veto the whole detector for several half-lives. Otherwise the detector dead-time would reach 100%.

Accidental background is mainly created by beta and gamma rays from natural radioactivity (like uranium and thorium and their daughter isotopes in the liquid scintillator or  $^{40}\text{K}$  in the PMT glasses) with energies above 1 MeV followed by some event creating an 8 MeV signal, like slow neutrons or high energetic gammas produced by muons. Alpha radiation does not contribute, as its visible energy in the liquid scintillator is quenched below 1 MeV, the positron threshold [Ard04]. In contrast to the correlated background the rate of accidental events can be measured in-situ. In order to avoid or, at least, decrease accidental background one has to carefully look for detector materials containing as little radioactivity as possible. The aim is to have a single event rate of less than 10 counts per second for events with an energy  $> 1$  MeV in the whole detector. This leads to strong limits on the radioactivity of the detector materials, especially for the liquid scintillators.

## 2.2 Detector site & setup

The nuclear power station in Chooz (see fig. 2.1) has two pressurized water reactors with a total thermal power output of 8.5 GW. At a distance of 1050 metres from the reactor cores an underground laboratory with an overburden of about 300 m.w.e. is located, where the far detector will be set up. The near detector shall be installed close to the reactor cores in an artificial cave with an overburden of at least 50 m.w.e. The shielding against cosmic rays

has to be built in such a manner, that the signal to background ratio exceeds 100. Both detectors are identical in structure, only the volumes of the inner veto differ slightly. Figure 2.4 shows a cross section of the planned detectors:

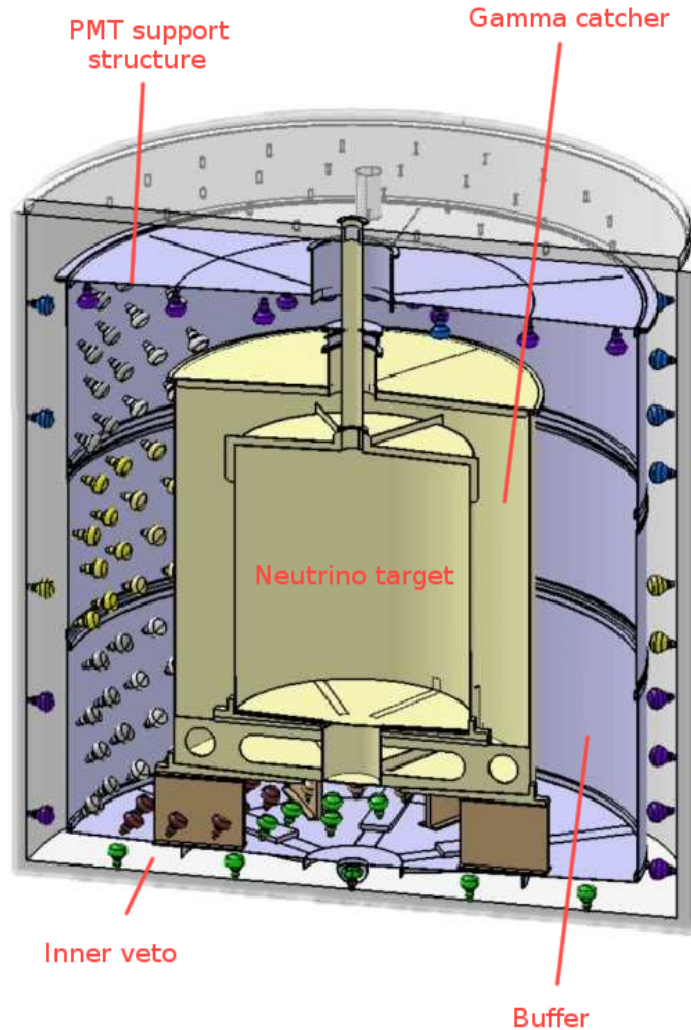


Figure 2.4: *Cross section of the DOUBLE CHOOZ detectors. From inside to outside: neutrino target, gamma catcher, buffer liquid, PMT support structure, and muon-veto. This veto is referred to as inner veto, while the so-called outer veto covering the detector on top (see text) is not shown here. From [Ard06].*

The DOUBLE CHOOZ detectors consist of four concentric cylindrical volumes. The innermost cylinder, the so-called neutrino target, is made of acrylic and filled with  $10.3 \text{ m}^3$  of 0.1% gadolinium loaded liquid scintillator. It is surrounded by another acrylic vessel filled with  $22.6 \text{ m}^3$  of non-loaded scintillator providing the same light yield as the neutrino target. This volume serves as gamma catcher for the gamma rays released after the neutron capture on gadolinium and ensures a homogeneous detector response<sup>3</sup>. These two volumes are surrounded by a steel tube, carrying 534 photomultiplier tubes for read-out. It is filled with  $114.2 \text{ m}^3$  of a non-scintillating liquid, the so-called buffer, in order to keep the gamma quanta from the radioactivity in the PMTs away from the target region.

The outermost volume,  $90 \text{ m}^3$  of liquid scintillator (with 78 photomultipliers) for the far detector and slightly more for the near detector, is serving as an active muon-veto (inner veto). Furthermore, the whole detector will be covered on top with layers of gas-filled wire proportional chambers. This outer veto system does not only provide redundancy for the inner veto, but also allows a higher tracking resolution and can tag even those muons, which merely pass near the detector and might produce fast neutrons.

---

<sup>3</sup>Homogeneous detector response means, that the visible energy after a neutron capture on gadolinium is always the same. Without the gamma catcher this visible energy would depend on the position of the event in the detector: for neutron events in the middle of the neutrino target the whole 8 MeV gamma energy could be seen, while for events taking place at the edge of the neutrino target some energy could be "lost" due to escaping gamma rays.



# Chapter 3

## Detector setup and calibration for low-background gamma spectroscopy

### 3.1 The detector system at a glance

The low-background measurements for the DOUBLE CHOOZ experiment are performed with a semi-conductor detector made of germanium. It is located at the Garching underground laboratory and surrounded by several active and passive shielding systems in order to reduce the background and thus increase the reachable sensitivity. Fig. 3.1 shows the open detection system, where the individual parts are marked in different colours.

The germanium detector, the gamma spectroscopy is done with, is a high-purity detector with a relative counting efficiency<sup>1</sup> of 150.5%. It is placed inside a 1.5 mm thick evacuated magnesium housing and operated at liquid nitrogen temperature. This germanium detector will be described in more detail in section 3.2.

For suppression of the background coming from Compton-scattered events in the germanium crystal, a sodium-iodide scintillation counter shielded with copper and aluminium and read out with 7 photomultipliers is used as anti-Compton veto (see section 3.3). Both the germanium and the sodium-iodide detectors are arranged within a 15 cm thick lead shielding, thus greatly reducing the background from external gamma sources in the laboratory. The innermost 5 cm of the lead are made of ultra pure lead from Poland with a specific activity of radioactive  $^{210}\text{Pb}$  of less than 5 Bq/kg [Lan07].  $^{210}\text{Pb}$  decays into  $^{210}\text{Bi}$ , releasing gamma rays with an energy of 45.6 keV, as well

---

<sup>1</sup>The definition of the relative counting efficiency is given on page 27 in section 3.2.

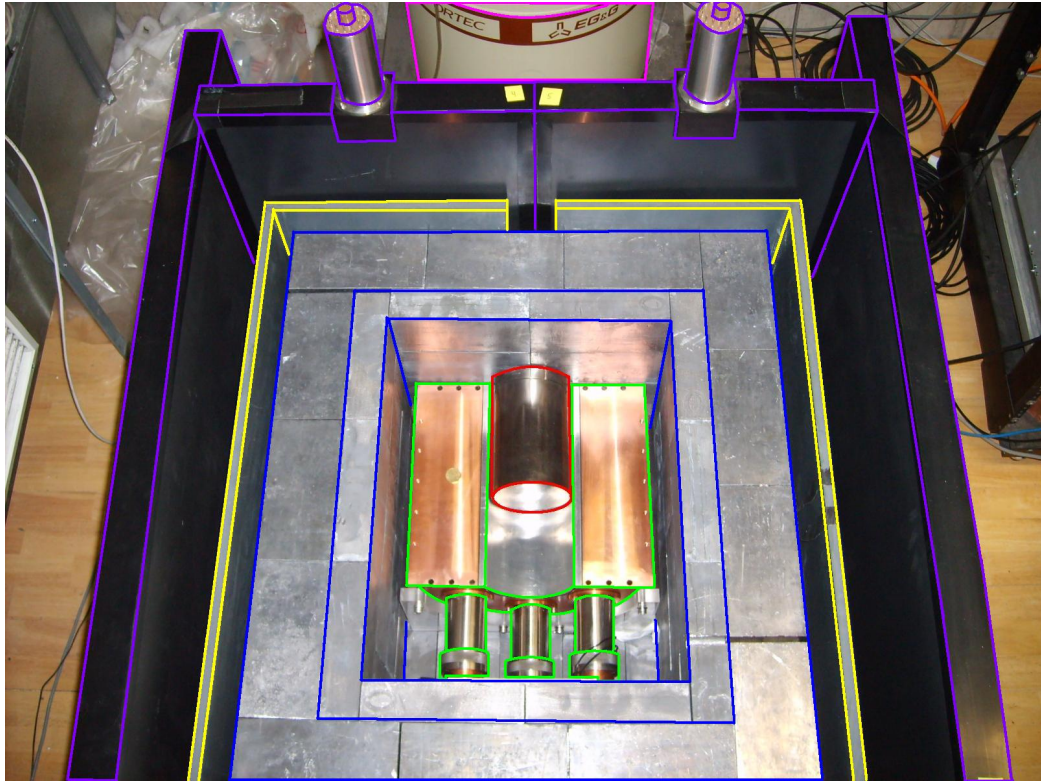


Figure 3.1: *The whole detection system with opened top cover. The part marked in red in the middle of the picture is the magnesium housing containing the germanium crystal. It is enclosed by the sodium-iodide scintillation counters in a copper and aluminium shielding (marked in green), the lead shielding (blue), the PVC box (yellow) and the active muon-veto system (purple). On the top of the picture the dewar for the liquid nitrogen supply can be seen (pink). To obtain an imagination of the size of the individual parts a 50 Eurocent coin was placed on the left side of the copper housing of the anti-Compton veto system.*

as X-ray fluorescence quanta from  $^{210}\text{Bi}$  (77.1 keV and 87.3 keV) due to internal conversion. Since gamma quanta of such a low energy are unable to penetrate 5 cm of lead, it is sufficient to use the low-activity lead only on the inside of the shielding. Thus the gammas from  $^{210}\text{Pb}$  produced in the outer part of the shielding will not reach the germanium detector at all.

The next part outwards is a 10 mm thick plastic box made out of polyvinyl chloride (PVC) sealed with silicone and rubber. This box serves as a shelter against the radioactive noble gas radon. To blow the air and with it the radon out of the box it is flushed before and also during operation with the evaporating nitrogen from the dewar containing the LN2 supply for the germanium detector. The nitrogen flux is about 166 litres gas per hour. The process takes quite a long time (at least 48 hours) and is done before each measurement.

Another severe background is coming from cosmic rays: While the hadronic component of the cosmic radiation is absorbed by the overburden of the underground laboratory, muons can easily penetrate into the detector and produce a signal either directly via ionization or by creating secondary particles interacting in the germanium crystal. These muons cannot be blocked, but using an active muon-veto system those events in the recorded spectra can be eliminated. Therefore the whole detector system, except for the bottom, is surrounded by plastic scintillator panels equipped with PMTs (see section 3.4).

The entire construction including the read-out electronics and measuring computer is located in the Garching underground laboratory. This lab provides an overburden of approximately six meters of soil, corresponding to 15 m.w.e. and being sufficient to nearly completely shield the hadronic components of the cosmic radiation and to reduce the energy-integrated muon flux by roughly a factor of three [Hen99]. Figure 3.2 shows two photographs of the underground lab and the experiments arranged there.

## 3.2 The germanium detector

The HPGe detector used for the low-background gamma spectroscopy is an "Ortec GEM" p-type detector (serial number: 35-P40627A). It is operated at liquid nitrogen temperature (77 K) to reduce thermal noise with an operation bias of +2000 V. The germanium detector has a relative counting efficiency of 150.5%, which means that the probability for a gamma ray to deposit its full energy within the germanium crystal is about one and a half times higher than that for a sodium-iodide crystal of cylindrical shape with 3" length and 3" diameter (the convention to assign 100% efficiency to such a sodium-iodide



Figure 3.2: *Photographs of the Garching underground laboratory. On the lefthand side, the detector system used for this diploma thesis can be seen (in front), as well as two further germanium detectors in their shieldings (back). The picture on the righthand side shows the insert of a  $^3\text{He}/^4\text{He}$  dilution refrigerator (back) for low-temperature experiments together with the gas-handling system and read-out electronics. In front, a silicon counter, also being within a lead assembly, can be seen.*

counter was made for historical reasons [Kno00]).

The high counting efficiency is reached by using a large crystal with an active volume of  $618\text{ cm}^3$  or 3275 grammes of pure germanium. The crystal itself has a diameter of 89.5 mm and a length of 99.0 mm with an inner bore of 8.1 mm diameter (see fig. 3.3). To protect its surface it is housed in an evacuated magnesium cylinder, also serving as entrance window for incoming gamma rays. The thickness of this window (1.5 mm at the frontside) leads to a lower detection threshold of approximately 15 keV, as for gamma quanta of an energy less than this value the penetration probability drops well below 5%.

The energy resolution obtained with this germanium detector is 2.189 keV at 1.33 MeV (gamma line from  $^{60}\text{Co}$ ; measured with a shaping time constant of the analogue main amplifier of  $8\ \mu\text{s}$ ) and 955 eV at 122 keV (gamma line from  $^{57}\text{Co}$ ). Furthermore the detector achieves a peak-to-Compton ratio of 93.9 for 1.33 MeV gamma rays; this means the intensity of the photopeak is more than 90 times higher than that of the corresponding Compton edge. Calibration of the germanium detector is carried out using calibration sources as well as gamma lines from the ambient radioactivity (e.g. the 2.6 MeV line from  $^{208}\text{Tl}$ ).

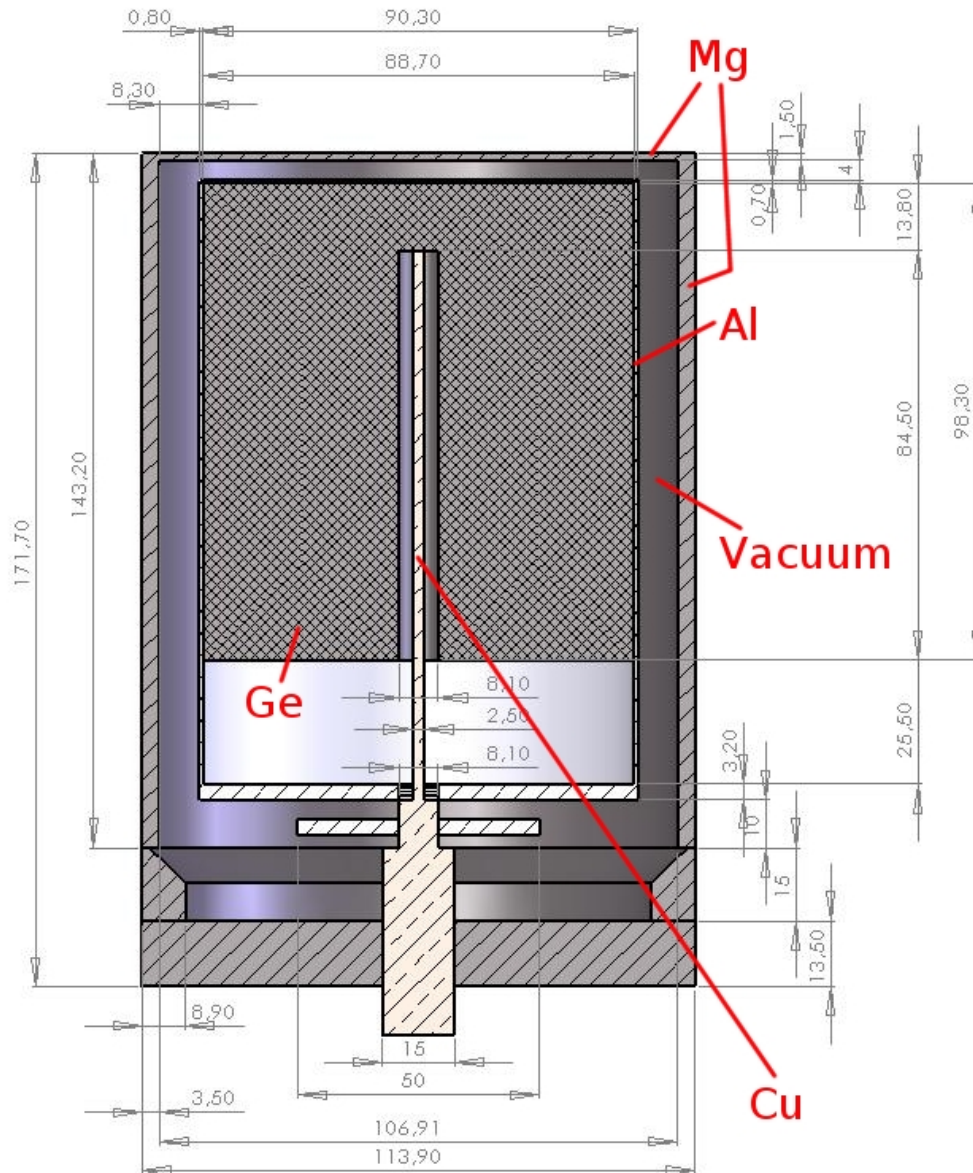


Figure 3.3: Cross section of the 150.5% germanium detector including the housing materials. The germanium crystal is represented by the hatched area in the middle of the figure. The rod in its center is made of copper and serves for cooling, as it has direct contact to the liquid nitrogen supply. Around the crystal a thin aluminium cylinder is mounted. Both parts reside within the evacuated magnesium housing. All dimensions in mm. After [Hen99].



Figure 3.4: *Photograph of the disjointed anti-Compton veto system consisting of sodium-iodide scintillation crystals in a copper shielding with aluminium entrance windows. From left to right: upper half shell, lower half shell and endcap. These parts surround the germanium detector in nearly  $4\pi$  geometry, except for a small solid angle at the backside of the germanium detector, which stays uncovered. The crystals of the half shells have a length of 300 mm and a diameter of 305 mm with an inner bore of 132 mm. The NaI detector system consists of six 2" PMTs (at the upper and lower half shell) and one 3" PMT mounted at the endcap.*

### 3.3 Anti-Compton veto

#### 3.3.1 General layout and working principle

As already mentioned in section 3.1, the germanium detector is enclosed by an anti-Compton veto system composed of thallium-doped sodium-iodide scintillation crystals. They are residing in a copper housing with 0.8 mm thick aluminium entrance windows (see fig. 3.4) made of ultrapure aluminium. The whole veto counter is divided into three parts, a lower and an upper half shell and an endcap (serial numbers given in tab. 3.1).

Gamma rays, which escape the germanium detector after a Compton scattering event, may deposit some energy in the sodium-iodide crystals (e.g. by photoeffect or a further Compton scattering), see figure 3.5. The signal produced by the scintillation light is afterwards converted into a logic pulse by the signal processing electronics (section 3.5), which then serves as veto

<i>detector part</i>	<i>type numbering / serial number</i>
upper half shell	305/2APC300/2(6)-E1 SS0223
lower half shell	
endcap	120AC100/3-E1-LB-X SS0224

Table 3.1: *Serial numbers of the detector parts of the anti-Compton veto manufactured by SCIONIX Holland.*

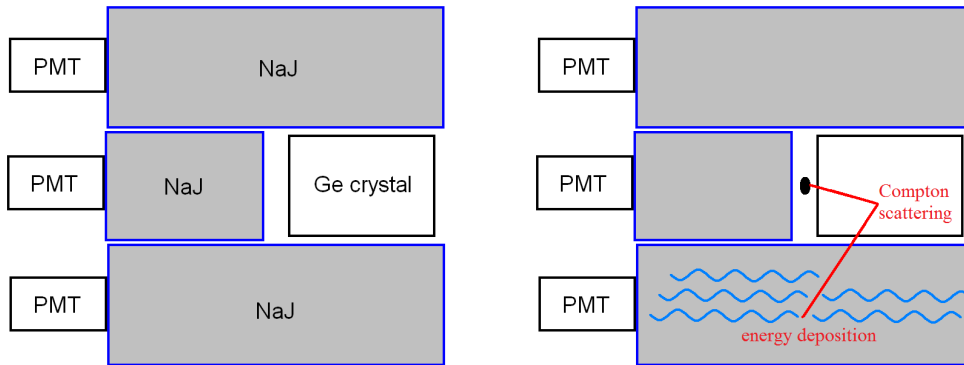


Figure 3.5: *Sketch of the working principle of the anti-Compton veto: after a Compton scattering, the gamma quantum deposits some energy within the sodium-iodide scintillation crystals, leading to a veto signal.*

signal. Due to this suppression of the Compton events especially gamma peaks at low energies become more prominent in the spectra recorded with the germanium detector and can thus be recognized more easily.

### 3.3.2 Calibration and balancing procedure

The first task in calibrating the anti-Compton veto was the detection of possible light leaks. This is of high importance as light leaks greatly increase the dark current of the PMT and therefore elevate the lower detection threshold leading to a worsening of the detector efficiency. The light leak detection was done using a  $^{241}\text{Am}$  calibration source, which emits gamma rays of the energies 26.3 keV, 33.2 keV and 59.5 keV. Recording the pulse height spectrum

of such a low-energetic gamma source provides information on the beginning of the noise band. According to the SCIONIX data sheet this should be at about 5 keV. Measured values for the start of the noise band are  $\sim 8$  keV for the endcap and  $\sim 15$  keV for the outer parts of the detector applying a high voltage of +750 V. These values are not perfect but adequate: gamma quanta of lower energy are unlikely to enter the scintillation counter through its entrance window.

During this procedure two major problems were recognized: Firstly, the fixture of the left PMT at the lower half shell was loose-fitting, leading to a bad contact between multiplier and scintillation crystal. This could be solved by replacing the fixture by a new one. Secondly, two PMTs (left and right one at the lower half shell) showed double peaks in their pulse height spectra. As an example figure 3.6 shows  $^{137}\text{Cs}$  spectra (single gamma line at 662 keV) of all seven PMTs. The appearance of double peaks is problematic as it tremendously worsens the energy resolution.

To inspect these two multipliers they were removed from the copper housing and checked for mechanical damage, but none was found. So they were mounted again at the anti-Compton veto, but this time without using optical compound in order to investigate whether a bad optical contact was causing the double peaks. Finally the problem was identified as a bad electrical contact in the gain (focus) potentiometers<sup>2</sup> of the PMT bases. It was solved by turning these potentiometers several times. Figure 3.7 on page 34 shows the influence of the potentiometer position on the peak shape in the pulse height spectrum.

Having solved these initial problems the next step in the installation of the anti-Compton veto system was to balance the gain of the photomultipliers by adjusting the gain (focus) potentiometers and the applied high voltages. This balancing serves for getting the best energy resolution possible. Furthermore, for geometrical reasons the read-out of the seven multipliers can happen by only one signal cable, therefore the gain of all PMTs should be fairly the same in terms of setting one common threshold. Thereby the highest possible detector efficiency is reached without creating too much dead-time. As the gain of the multipliers at the endcap and the lower half shell is bigger than that of the upper multipliers (cf. fig. 3.6), it was decided to use two different high voltages, one for the three upper 2-inch multipliers and one for the other four ones. The figures A.1, A.2 and A.3, which can be found in appendix A, show the respective  $^{137}\text{Cs}$ -spectra of the upper and lower half shells and the

---

<sup>2</sup>According to the SCIONIX data sheet these potentiometers are for gain adjustment. However, because of the defocussing effect of the potentiometers (see fig. 3.7), they are called "gain (focus)" in the following.

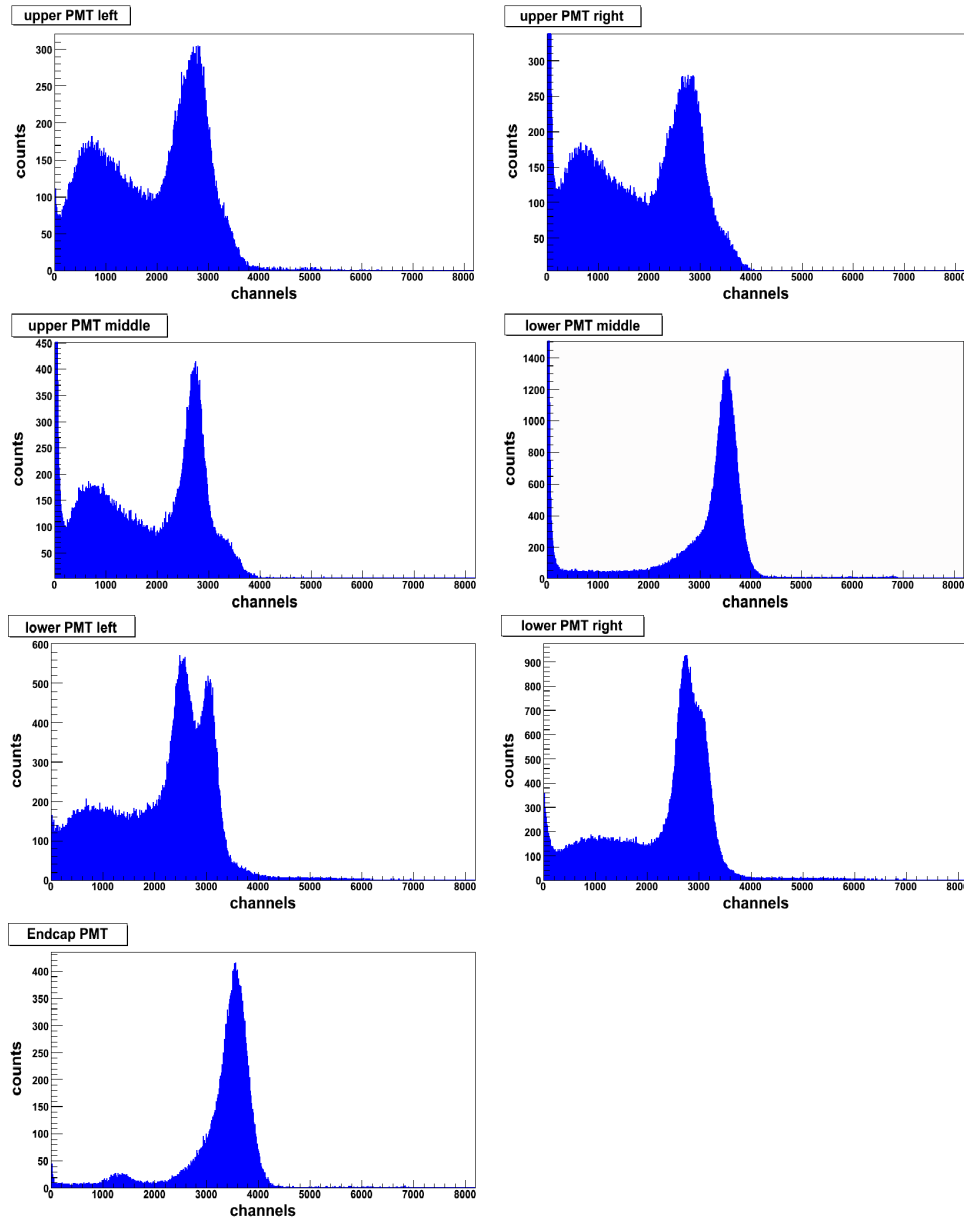


Figure 3.6:  $^{137}\text{Cs}$ -spectra of all seven multipliers of the anti-Compton veto. The double peaks in the spectra of the PMTs left and right at the lower half shell can clearly be seen. All spectra were recorded with an amplification of  $\sim 3k$ , a high voltage of  $+900\text{ V}$  and full gain (focus) at the PMT potentiometers. The measuring time was 300 seconds.

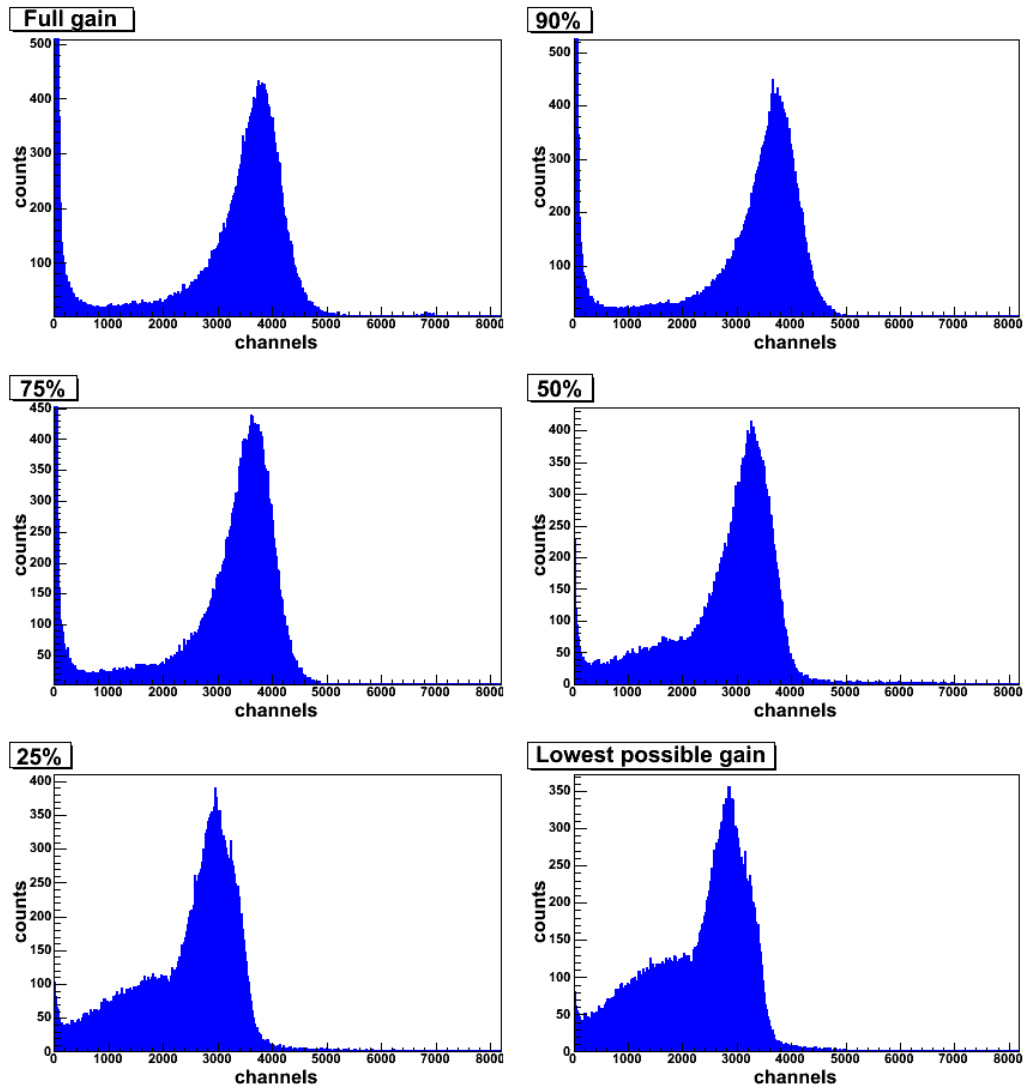


Figure 3.7:  $^{137}\text{Cs}$ -spectra of the lower-left PMT with different positions of the gain (focus) potentiometer: Full gain, potentiometer at 90%, 75%, 50%, 25% and lowest possible gain. High voltage: +1000 V. All spectra were recorded over 300 seconds.

<i>Energy resolution at 662 keV</i>			
<i>Applied voltage</i>	<i>upper half shell</i>	<i>lower half shell</i>	<i>endcap</i>
+850 V	23.0%	14.6%	8.7%
+900 V	21.3%	13.7%	8.1%
+950 V	19.4%	11.2%	8.5%

Table 3.2: *Energy resolution of the different anti-Compton veto parts using the  $^{137}\text{Cs}$ -spectra shown in fig. A.1 - A.3 in appendix A. The gain (focus) potentiometers of all photomultipliers are set to maximum.*

endcap for different voltages.

Table 3.2 lists the energy resolution at 662 keV of the different parts of the anti-Compton veto at three different high voltages.

The energy resolution of the endcap and the lower half shell match the values quoted in the SCIONIX data sheet, hence at these PMTs the gain (focus) potentiometers are kept at maximum position. For the upper half shell the balancing procedure is executed. This procedure, including all relevant spectra, can also be found in appendix A.

The energy resolution obtained for the upper half shell after the balancing procedure was 20.6% (with +950 V). As this value has not improved compared to that observed before balancing, a bad optical contact between multipliers and scintillation crystal was supposed to be the reason. Consequently the three PMTs were unscrewed from the copper housing and the optical compound was removed.

Now the energy resolution even changed for the worse (24.4%). Furthermore from tab. A.2 it can be seen, that the individual gain of the PMTs reduced, too. For these reasons the three multipliers were again removed and then remounted, this time recontacted with optical compound. Thereafter the balancing procedure was applied again using a high voltage of 950 V (fig. A.4 and tab. A.3).

Finally the energy resolution did not match the value from the data sheet (8.3%) and stayed at 20.2%. However, this bad resolution is not so bothersome as long as the sodium-iodide scintillator is only used as anti-Compton veto in anti-coincidence mode with a threshold just above the photomultiplier noise. But it would become a problem, if the energy threshold has to be

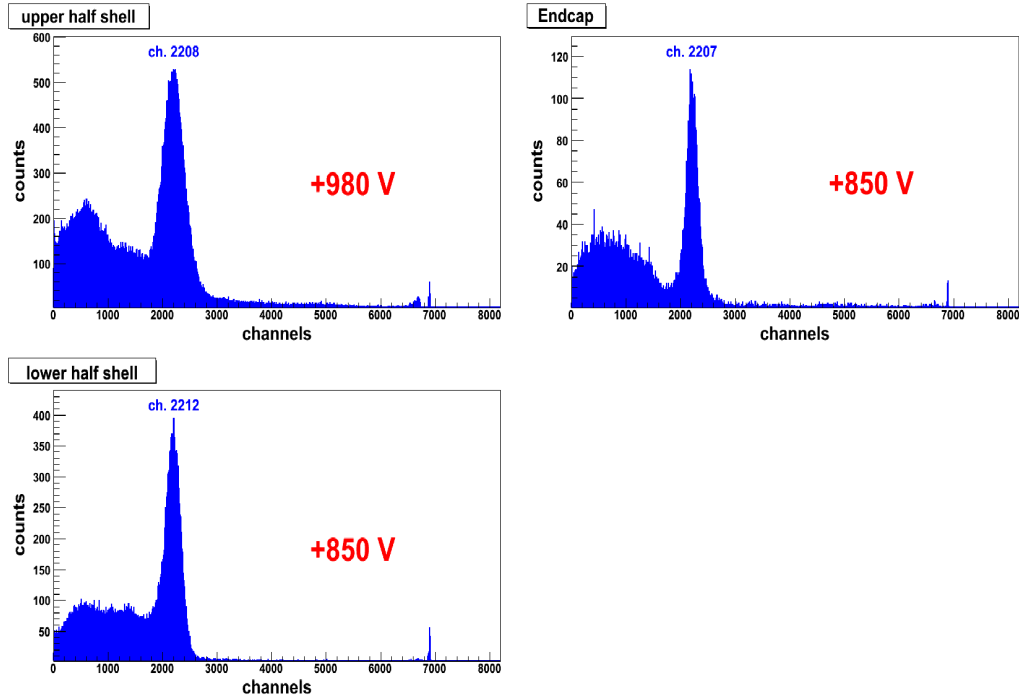


Figure 3.8: *Final  $^{137}\text{Cs}$ -spectra of the three anti-Compton veto parts with balanced gain (focus) and high voltage. The position of the photo peak (in channels) as well as the used voltage are displayed in each picture. Recorded over 100 seconds of measuring time.*

set to a certain value or if coincidence measurements have to be made. For example one could think of triggering on the 511 keV positron annihilation line appearing after a pair production process. This coincidence condition would allow to measure the single or double escape peaks of a high-energetic gamma line nearly background-free.

The last step of the calibration process was the adjustment of the high voltage, so that the three parts of the anti-Compton detector have approximately the same gain. For the endcap and the lower half shell 850 volts have been found to be optimal and the gain (focus) potentiometer of the 3" PMT at the endcap was slightly adjusted to match the correct gain. The potentiometers at the upper half shell stayed at the positions obtained in the balancing procedure; the optimal voltage used here is 980 V. The resulting  $^{137}\text{Cs}$ -spectra are displayed in fig. 3.8, including the peak position in channels.



Figure 3.9: *The fully equipped active muon-veto system consisting of 6 plastic scintillator panels with photomultiplier tubes. The panels are made of a scintillating material called BC408, which is based on polyvinyl toluene (see fig. 3.10).*

## 3.4 Muon-veto system

### 3.4.1 Overview of the setup

As already mentioned above, the detector system is equipped with an active muon-veto system to reject events from cosmic muons. This muon-veto is consisting of 6 plastic scintillator panels, surrounding the detector on top and on all sides except on the bottom (fig. 3.9).

These panels are made of a scintillating plastic material called polyvinyl toluene (see fig. 3.10) including additional fluors and are covered with a light-tight foil. Each panel is 5 cm thick and equipped with a 3" PMT. Table 3.3 lists their serial numbers as well as those of the PMT bases, while fig. 3.11 shows the shape and the size of the different panels.

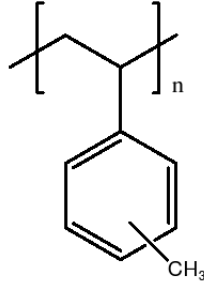


Figure 3.10: *The chemical structure of polyvinyl toluene [Ste07]. The brackets with the index  $n$  indicate, that this molecule is repeated very often to form the PVT chains. The sum formula is  $(C_2H_3-C_6H_4-CH_3)_n$ .*

<i>Panel number</i>	<i>position</i>	<i>serial number / PMT base number</i>
1	side left	43.307X29.528R2BC408/2 PG-564 02079863
2	side right	43.307X29.528R2BC408/2 PG-563 02079859
3	front	39.370X31.496R2BC408/2 PG-562 02079860
4	back left	31.496X17.717R2BC408/2 PG-567 02079861
5	back right	31.496X17.717R2BC408/2 PG-568 02079862
6	top	43.31X35.43H2BC408/2L PI-932 02079864

Table 3.3: *Position and serial numbers of the 6 muon-veto panels manufactured by BICRON. The position is given as seen from the middle of the underground lab.*

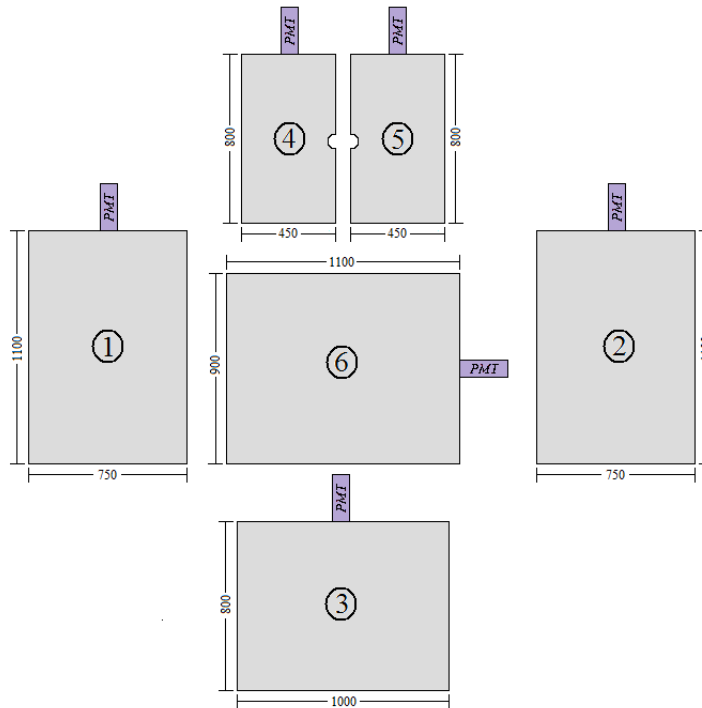


Figure 3.11: Schematic view of the 6 plastic scintillator panels. The sizes are given in units of millimeters.

### 3.4.2 Calibration

In order to identify cosmic muons correctly with a high efficiency and without generating too much dead time, the muon-veto system has to be calibrated. Spectra with a radioactive calibration source ( $^{60}\text{Co}$ ; gamma energies of 1.173 MeV and 1.332 MeV) were recorded with all 6 panels. The  $^{60}\text{Co}$ -source was held roughly in the middle of each panel. To record the spectra a main amplifier (type 2010 from CANBERRA; gain:  $\sim 3\text{k}$ ) and the CANBERRA Genie-2000 software were used<sup>3</sup>.

The high voltage for each panel was adjusted in such a way, that the Compton edge of  $^{60}\text{Co}$  appears at nearly the same position in all spectra, i.e. the same channel in the spectrum. The voltages found in this procedure are given in tab. 3.4 and are used as well for the muon-veto later on during the measurements. The "gain" potentiometer at the PMT bases was chosen maximal in all six cases.

The last step in calibrating the muon-veto system was the adjustment of the focus of the PMT bases. The "focus" potentiometer was set into the

<sup>3</sup>These spectra can be seen in figure B.2 in appendix B.

<i>panel number</i>	<i>Voltage</i>	<i>Current without radioactive source</i>
1	+1400 V	186 $\mu\text{A}$
2	+1400 V	187 $\mu\text{A}$
3	+1380 V	183 $\mu\text{A}$
4	+1187 V	157 $\mu\text{A}$
5	+1207 V	159 $\mu\text{A}$
6	+1182 V	157 $\mu\text{A}$

Table 3.4: *Voltages and currents of the PMTs mounted at the plastic scintillator panels.*

middle position and the spectrum of the  $^{60}\text{Co}$  source was recorded. Then the potentiometer was turned slightly into one direction and the spectrum was recorded again. Did the number of counts within the interval of  $\pm 200$  channels around the maximum of the Compton-edge peak increase, the focus improved. In this case the potentiometer was turned further in the same direction, until a maximum of the counts was reached. Did the number of counts in the given interval however decrease, the focus deteriorated and the next turns were therefore made in the opposite direction until again the best focus was reached<sup>4</sup>.

After that the  $^{60}\text{Co}$  calibration source was removed and for each panel a muon spectrum was recorded (amplifier gain now  $\sim 300$ ). These spectra are shown in fig. 3.12. Besides the PMT dark noise at low energies<sup>5</sup> (exponential behavior) the Landau distribution [Voj95] of the cosmic muons can clearly be seen. These spectra have been used later on in order to adjust the discriminator thresholds for the muon-veto (cf. chapter 3.5).

---

<sup>4</sup>Again, the results of this procedure can be seen in appendix B (fig. B.3).

<sup>5</sup>The electronic noise is negligible. This was proven by recording spectra without HV supply for the PMTs. In these spectra no noise was observable at all. Thus the dark noise of the PMTs is the main contribution to the pedestal as seen in the spectra in fig. 3.12.

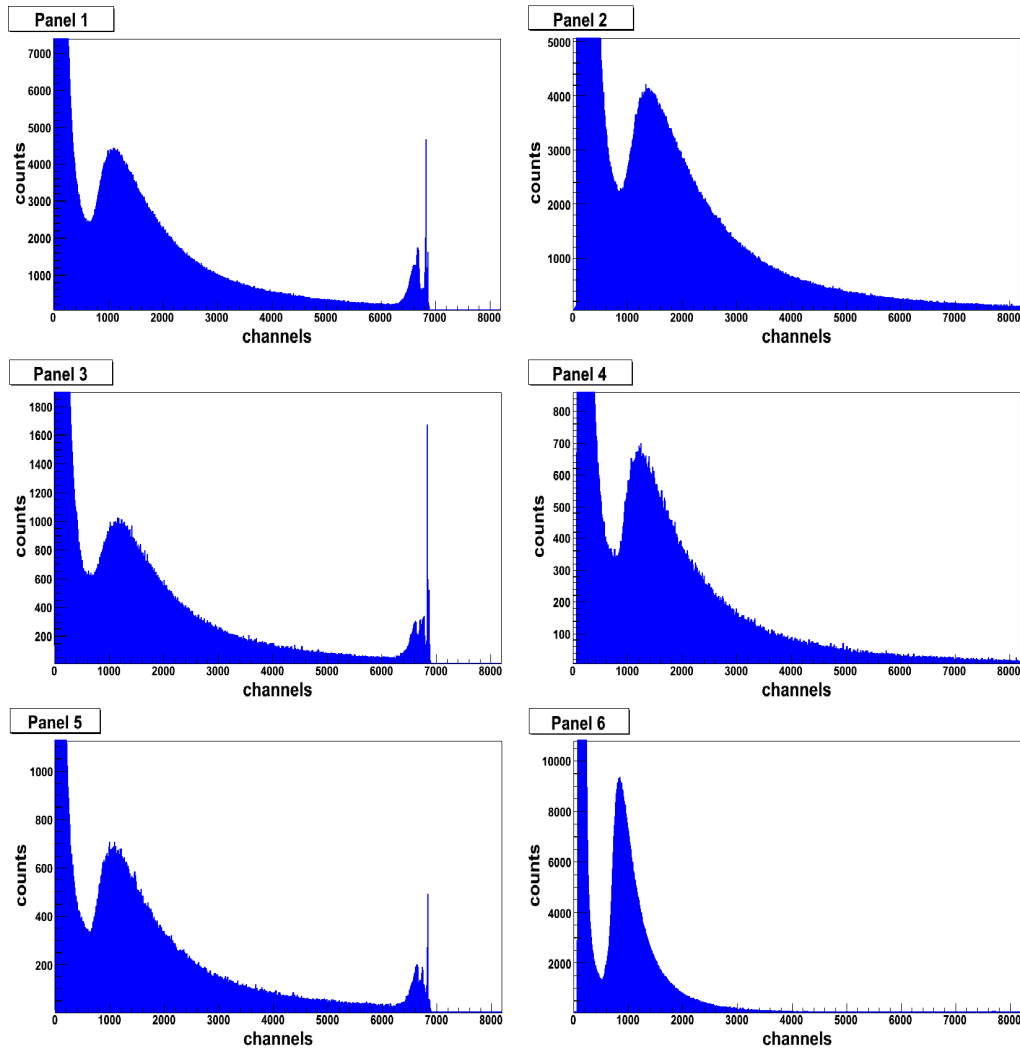


Figure 3.12: *Muon spectra of the six plastic scintillator panels, measured over a longer time (typically over night) in the Garching underground laboratory. The structures at the high-energetic end of the three spectra on the lefthand side are due to the upper threshold ("overflow") of the ADC used and have no physical meaning.*

### 3.5 Read-out electronics for signal processing

#### 3.5.1 Analogue part of the electronics

Figure 3.13 shows the wiring diagramme of the NIM read-out electronics, as it was developed and used for the measurements.

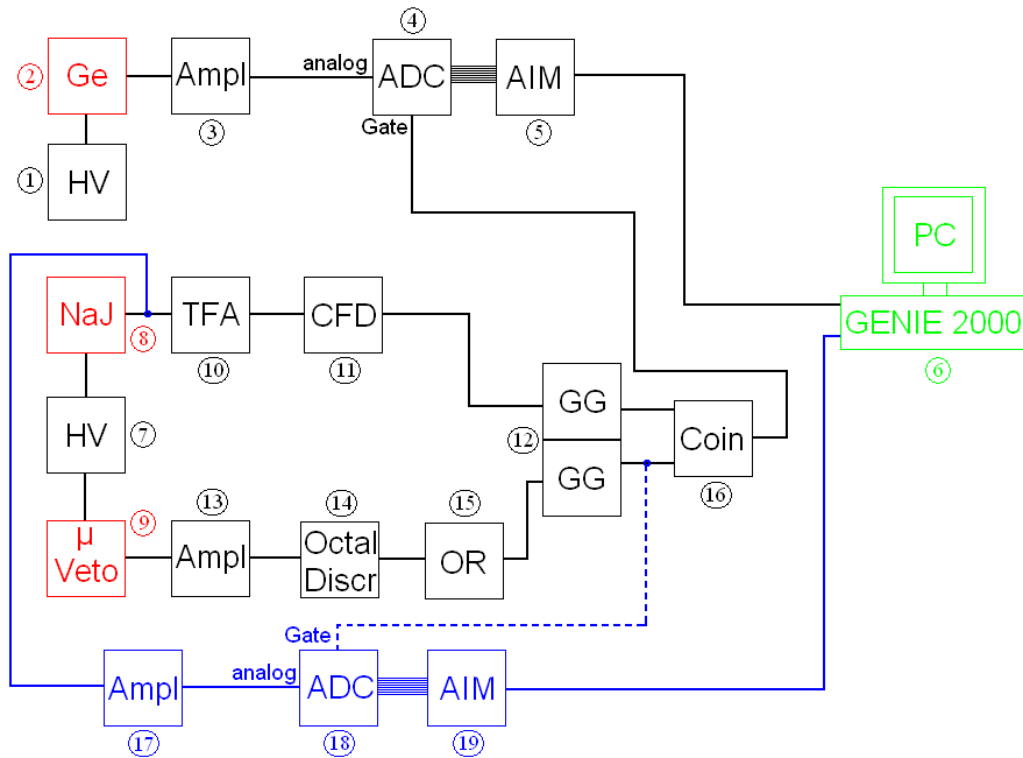


Figure 3.13: *Wiring diagramme of the read-out electronics. The individual modules are tagged with a number and explained in greater detail in the following itemisation.*

1. High voltage power supply for the germanium detector type "HVS 2" manufactured by HALDER. Operation bias is +2000 volts.
2. Germanium detector (see section 3.2)
3. Main amplifier "Model 2010" from CANBERRA for amplification and shaping of the germanium signal. The power supply for the preamplifier at the germanium detector is connected to this module, too. Used settings for the gamma spectroscopy are (unless otherwise noted):

- *coarse gain*: 30
  - *fine gain*: 3.00
  - *shaping time constant*:  $8 \mu\text{s}$
  - *pole zero (P/Z)*: optimized with oscilloscope
  - *base line restorer (BLR)*: SYM, HI
  - *output polarity*: positive
4. Analogue-to-digital converter (ADC) type CANBERRA "8713". Unless otherwise noted the used settings are:
    - *gain*: 8k
    - *peak detect*: auto
    - *mode*: PHA+
    - *coincidence mode*: anticoincidence
  5. Acquisition interface module (AIM) CANBERRA "556 A" with the ethernet address B87. This NIM module serves as multichannel analyser and is read out by the computer.
  6. Measuring computer. For the gamma spectroscopy measurements the software package "Genie-2000" from CANBERRA is used.
  7. High voltage supply "EHQ F020p" from ISEG for the photomultipliers of the anti-Compton veto and the muon-veto system. It has 16 computer-controlled channels and is mounted in a separate crate. The used voltages for the muon-veto can be found in tab. 3.4 on page 40 and for the anti-Compton veto in fig. 3.8 on page 36.
  8. Sodium iodide scintillation counter as anti-Compton veto (section 3.3). All seven PMTs are read out through one signal cable.
  9. Plastic scintillator panels (section 3.4). Here each multiplier has its own signal cable.
  10. Timing filter amplifier (TFA) CANBERRA "2110". This fast amplifier shapes the signal from the anti-Compton veto. For anticoincidence measurements the following settings were used:
    - *coarse gain*: 25
    - *fine gain*: full

- *integration time:* 20 ns
  - *differentiation time:* 100 ns
11. Constant fraction discriminator (CFD) HALDER type "2129" used for setting a lower threshold for the anti-Compton signal. Settings for triggering just above the PMT noise (lowest possible threshold,  $\approx 15$  keV):
- *window:* full
  - *lower level:* 0.20
  - *walk adjust:* optimized with oscilloscope

The veto signal is taken from the TTL output in CFT-mode.

12. Gate generator (GG) "GG 1300" manufactured by the electronics workshop of the Physik-Department of the TUM in Garching. This unit contains two modules, one is used for the muon-veto and one for the anti-Compton veto. The gate generator broadens the logic veto signal to 20  $\mu$ s. Furthermore, it delays the logic pulse so that it fully covers the analogue signal from the germanium detector.
13. 10-channel fast amplifier "Model N979" from CAEN for amplification of the muon-veto signal without time delay. Each channel has its own zero cancellation potentiometer, all adjusted separately with the oscilloscope.
14. 8-channel discriminator "Model 623 BLZ" from LeCROY. At this module an individual threshold is set for each muon panel, see tab. 3.5. These thresholds were adjusted using a ratemeter and the muon spectra shown in fig. 3.12 on page 41. The width of the output pulse was set to 100 ns for each channel.
15. OR-logic from BORER & CO, "Type L320" for collecting the six logic signals from the muon-veto. As the modules 13 through 15 operate with negative NIM logic (-0.8 V), a CFD is installed between the OR-logic and the gate generator for transforming the veto signal into a positive TTL pulse (+2.0 V when terminated with 50  $\Omega$ ).
16. Coincidence/Anticoincidence logic "K 1100", also manufactured by the electronics workshop of the Physik-Department of the TUM. This module serves for gathering the two veto signals from both veto systems.

<i>Muon panel</i>	<i>Discriminator threshold</i>
Panel 1	82.0 mV
Panel 2	97.5 mV
Panel 3	108.5 mV
Panel 4	60.5 mV
Panel 5	47.5 mV
Panel 6	31.5 mV

Table 3.5: *Discriminator thresholds for the individual muon-veto panels. These thresholds are adjusted in such a manner that the countrate above the threshold is identical to that determined from the muon spectrum (fig. 3.12 on page 41).*

Each channel can be switched either into coincidence mode or anticoincidence mode. Most measurements are performed in anticoincidence with both channels.

The total veto countrate is  $\sim 300$  Hz, when both the muon-veto and the anti-Compton veto are used in anticoincidence mode. Together with the veto window of  $20 \mu\text{s}$  this leads to a dead-time of the whole detector system of 0.6%.

The modules marked in blue in fig. 3.13 can be used optionally to check the analogue signal from the sodium-iodide crystals.

17. Main amplifier "Model 2021" from CANBERRA for signal amplification and shaping. Here some attention has to be payed to the shaping time constant: it should not be too large in order not to overload the input stage of the amplifier. Otherwise this would result in spectra where all events are stored into a Gaussian peak around the same channel independent of the energy of the events.

- *coarse gain:* 300
- *fine gain:* 0.3

- *shaping time constant*: 0.25  $\mu\text{s}$
- *pole zero (P/Z)*: optimized with oscilloscope
- *base line restorer (BLR)*: SYM, AUTO
- *output polarity*: positive

18. Like module 4.

19. Like module 5, but with the ethernet address B7C. The veto signal produced by the muon-veto system is used in anticoincidence mode at the gate input.

For cable connections RG58 cables (50  $\Omega$  impedance) with BNC connectors are used, except for the signal cable between germanium detector and main amplifier (RG62 BNC cable) and the interconnections between modules 13 through 15 (done with LEMO cables).

### 3.5.2 Digital signal processing with the DSP 9660A

In addition to the analogue read-out electronics described in section 3.5.1, a digital signal processing unit (DSP; module type 9660A from CANBERRA) was tested. The DSP is a combined digital amplifier and ADC. It replaced the analogue main amplifier and the ADC used for signal processing for the germanium detector (modules 3 and 4 in fig. 3.13), while the rest of the electronic setup stayed the same. Within the DSP the incoming analogue signal is at first amplified, after that directly digitised and then filtered with a trapezoidal filter function. The rise time and the flat-top time of this filter function are user-defined. Table 3.6 summarises the settings for the rise time and flat-top time, as well as the respective measured values for the energy resolution obtained for the 1.33 MeV line of a  $^{60}\text{Co}$  source.

The best energy resolution of 1.764 keV was obtained for a rise time of 16.8  $\mu\text{s}$  and a flat-top time of 1.2  $\mu\text{s}$ . Therefore these settings have been used for the measurements. This resolution is considerable better than that achieved with the analogue main amplifier/ADC (2.189 keV). Also in long-term measurements the energy resolution with the DSP is  $\sim 10\%$  better. However, it was observed, that the count rate in a given peak in the pulse height spectrum of the digital electronics is  $\sim 3\text{-}4\%$  less than that obtained with the analogue part. The reason for this behaviour is up to now unknown and will be investigated in future experiments.

<i>FWHM in keV</i>					
rise time [ $\mu\text{s}$ ]	12.0	13.6	15.2	16.8	18.4
flat top time [ $\mu\text{s}$ ]					
1.2	2.549	2.107	1.965	1.764	1.828
1.4	2.367		1.907	1.790	1.943
1.6			1.917	1.821	1.909
1.8			1.980	2.036	
2.0				2.103	
2.2				2.014	
2.4			1.842		
3.0				1.862	

Table 3.6: *Energy resolution obtained with the DSP 9660A for the 1.33 MeV gamma line of  $^{60}\text{Co}$ . Countrate is roughly 30 Hz, measuring time 1000 seconds. The different rows give the respective flat top times for digital signal processing, the columns the rise times (both in units of  $\mu\text{s}$ ). Attention has to be payed, that the sum of rise time and flat top time does not exceed 20  $\mu\text{s}$ . Otherwise the veto signal would be too short.*



# Chapter 4

## Monte-Carlo Simulation for the determination of the detector efficiency

### 4.1 The source code

In chapter 5 the analysis of the measured spectra will be completed and the characteristic gamma lines of the different isotopes will be found. The remaining task is the determination of the respective activities. For long-lived isotopes, or isotopes from a natural decay chain (see appendix E), which are in radioactive equilibrium, the activity is constant over the measuring time. In this case, the activity of a certain isotope in a sample is given by

$$A = \frac{N}{t \cdot \varepsilon_{Det} \cdot P} \quad , \quad (4.1)$$

where  $N$  denotes the number of counts in the corresponding peak,  $t$  the measuring time,  $P$  the relative intensity of the gamma ray in this decay and  $\varepsilon_{Det}$  the detector efficiency. From this activity  $A$ , the mass concentration  $c$  of the radioactive contamination can be calculated:

$$c = \frac{A \cdot \tau \cdot m}{M_{sample}} \quad . \quad (4.2)$$

Here  $\tau$  stands for the lifetime of the isotope,  $m$  its atomic mass and  $M_{sample}$  is the mass of the whole sample.

The detector efficiency  $\varepsilon_{Det}$  specifies the probability, that a gamma quantum deposits its whole energy within the germanium detector. Hence it depends on two major contributions: firstly, the geometry of the whole setup

including the solid angle covered by the germanium detector as well as the materials surrounding the sample; and secondly, it depends on the energy of the gamma ray, as this energy determines the cross sections for the photoeffect, Compton scattering and, if possible, pair production.

The determination of the detector efficiency for different geometries and gamma energies is a crucial point for gamma spectroscopy measurements. For this reason a Monte-Carlo simulation has been developed based on the software package GEANT4 written in C++ [Ago03, All06, CER07].

The structure of the source code is shown in the tree diagramme displayed in fig.4.1.

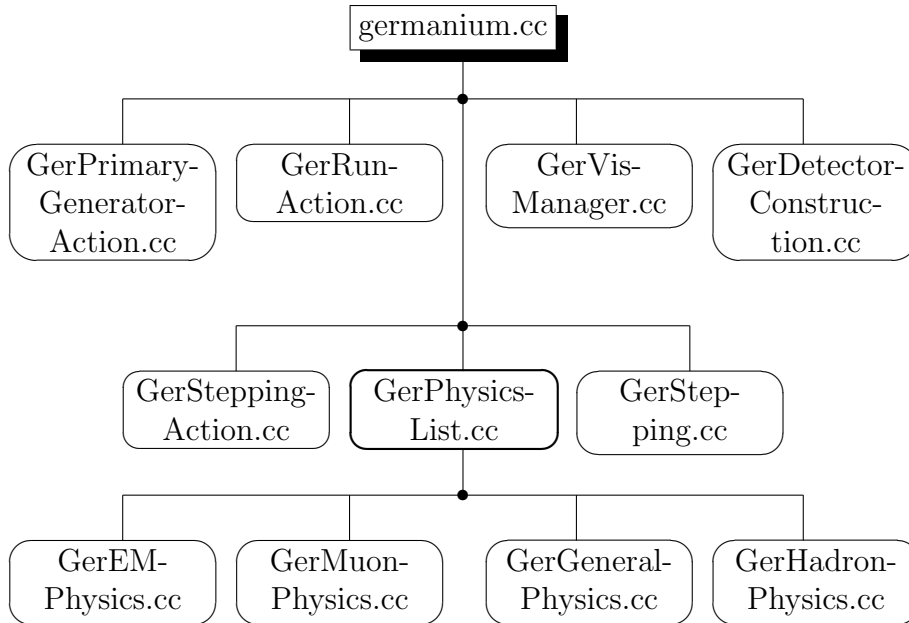


Figure 4.1: *Tree diagramme of the source code of the simulation. All files are linked into the main file called "germanium.cc". The file "GerPhysicsList.cc" is subdivided into several files, each including the physics for different kinds of particles.*

This simulation contains the full detector geometry including the germanium detector in its housing, the anti-Compton veto and the muon-veto system (needed when simulating cosmic muons), the lead shielding and the PVC box. A tracked gamma ray and its events can be seen in fig. 4.2.

The physics list "GerPhysicsList.cc" contains (nearly) all kinds of particles and interactions, even those not needed directly for simulating gamma

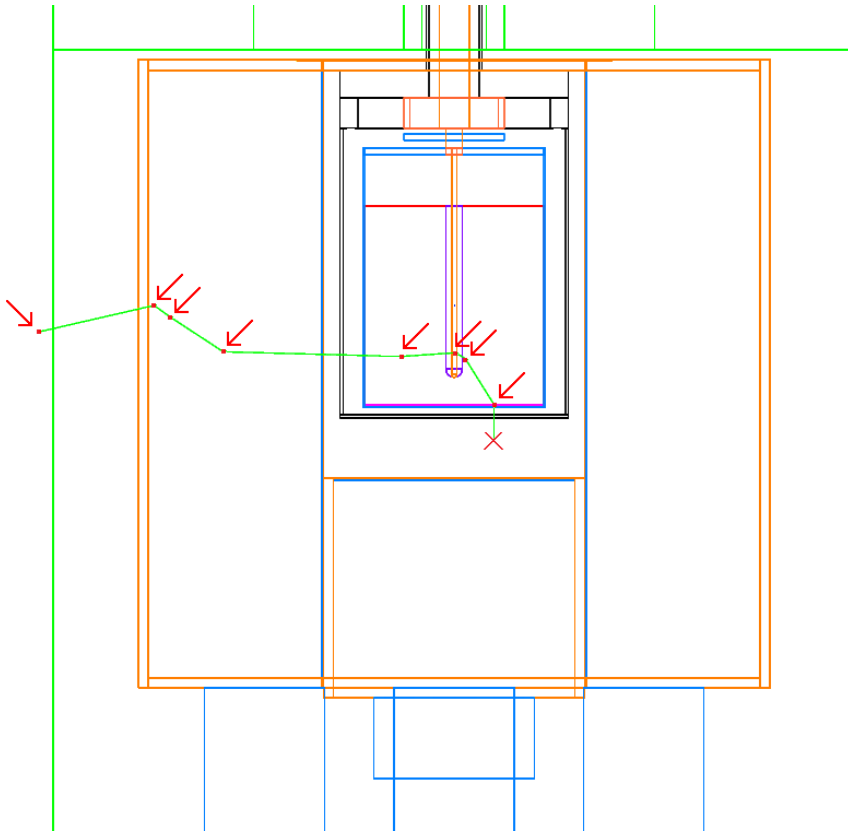


Figure 4.2: *Simulated gamma event in the software tool kit GEANT4. The gamma quantum, generated at the point marked with "x" between the germanium detector (top) and the endcap of the anti-Compton veto with an energy of 1.33 MeV, does four Compton scatterings (red arrows) within the germanium crystal, then escapes and scatters three times in the sodium-iodide counter before it is finally absorbed in the lead shielding (last red arrow).*

rays or cosmic muons. Table 4.1 gives an overview of the included particles and their interactions.

## 4.2 Simulated detector efficiencies versus measured values

The Monte-Carlo simulation has of course to be checked for its accuracy. Therefore values of  $\varepsilon_{\text{Det}}$  have been simulated (in the following denoted by  $\varepsilon_{\text{sim}}$ ) and compared to detector efficiencies  $\varepsilon_{\text{meas}}$  calculated from measurements with calibration sources with known activities. Tables 4.2 and 4.3 list

	EM				MUON					HADRON		
	<i>gamma</i>	$e^-$	$e^+$	$\nu_e, \bar{\nu}_e$	$\mu^-$	$\mu^+$	$\tau^-$	$\tau^+$	$\nu_\mu, \bar{\nu}_\mu, \nu_\tau, \bar{\nu}_\tau$	<i>mesons</i>	<i>baryons</i>	<i>shortlived</i>
<i>photoeffect</i>	✓											
<i>nuclear photoeffect</i>	✓											
<i>Compton effect</i>	✓											
<i>pair production</i>	✓				✓	✓						
<i>pair production to <math>\mu^\pm</math></i>	✓											
<i>bremsstrahlung</i>		✓	✓		✓	✓						
<i>ionization</i>		✓	✓		✓	✓	✓	✓		✓	✓	✓
<i>scattering</i>		✓	✓		✓	✓	✓	✓		✓	✓	✓
<i>annihilation</i>			✓								✓	
<i>annihilation to muons</i>			✓									
<i>annihilation to hadrons</i>			✓									
<i>spallation</i>					✓	✓						
<i>capture</i>					✓					✓	✓	
<i>decay</i>					✓	✓	✓	✓		✓	✓	✓
<i>Cherenkov radiation</i>		✓	✓		✓	✓						

Table 4.1: *Particles and interactions included in the Monte-Carlo simulation. The columns mesons and baryons summarize all longlived hadronic particles, while shortlived stands for baryonic resonances and quarks. For test runs the file "GerGeneralPhysics.cc" provides the non-physical particles "geantino", having no interactions at all, and "charged geantino", only interacting with electromagnetic fields. The row "scattering" includes both elastic and inelastic processes. The hadron physics is mainly needed for the simulation of neutrons, created by gammas or muons and interacting within the germanium detector.*

energy [keV]	isotope	Simulated efficiency $\varepsilon_{sim}$ [%] centered on the symmetry axis		
		10 mm	100 mm	200 mm
26	$^{241}\text{Am}$	18.43±0.04	2.64±0.02	0.80±0.01
33	$^{241}\text{Am}$	23.79±0.05	3.17±0.02	0.91±0.01
60	$^{241}\text{Am}$	28.85±0.05	3.53±0.02	1.05±0.01
81	$^{133}\text{Ba}$	28.86±0.05	3.50±0.02	1.04±0.01
122	$^{57}\text{Co}$	27.08±0.05	3.25±0.02	0.97±0.01
136.4	$^{57}\text{Co}$	26.26±0.05	3.19±0.02	0.96±0.01
302	$^{133}\text{Ba}$	16.97±0.04	2.12±0.02	0.67±0.01
356	$^{133}\text{Ba}$	15.15±0.04	1.92±0.01	0.62±0.01
511	$^{22}\text{Na}$	12.03±0.04	1.56±0.01	0.50±0.01
662	$^{137}\text{Cs}$	10.26±0.03	1.35±0.01	0.45±0.01
834	$^{54}\text{Mn}$	8.94±0.03	1.19±0.01	0.39±0.01
898	$^{88}\text{Y}$	8.54±0.03	1.12±0.01	0.38±0.01
1173	$^{60}\text{Co}$	7.28±0.03	0.99±0.01	0.33±0.01
1275	$^{22}\text{Na}$	6.87±0.03	0.93±0.01	0.32±0.01
1332	$^{60}\text{Co}$	6.67±0.03	0.93±0.01	0.31±0.01
1836	$^{88}\text{Y}$	5.40±0.02	0.75±0.01	0.26±0.01

Table 4.2: Simulated values for the detector efficiency  $\varepsilon_{sim}$  for different geometries. The gamma source is point-like and centered on the axis of the detector system in a distance to the entrance window given above the last three columns. The source emits the gamma rays into  $4\pi$  solid angle.

the simulated efficiencies for different geometries and gamma rays of different energies emitted by a point-like source into  $4\pi$  solid angle<sup>1</sup>, once for a symmetric setup (gamma source placed on the symmetry axis of the detector system) and once for an asymmetric configuration (source placed 2 cm off-axis).  $\varepsilon_{sim}$  and its statistical error are given by:

$$\varepsilon_{sim} = \frac{N}{N_{total}} \pm \frac{\sqrt{N}}{N_{total}} . \quad (4.3)$$

N is the number of events in the photopeak, while  $N_{total}$  denotes the total number of simulated gamma quanta.

In order to perform the measurements of the detector efficiency  $\varepsilon_{meas}$ ,

---

<sup>1</sup>In appendix C the mathematical formalism developed for the simulation of an isotropic source can be found.

energy [keV]	isotope	Simulated efficiency $\varepsilon_{sim}$ [%] 2 cm off-axis	
		100 mm	200 mm
26	<sup>241</sup> Am	2.53±0.02	0.76±0.01
33	<sup>241</sup> Am	3.02±0.02	0.91±0.01
60	<sup>241</sup> Am	3.43±0.02	1.03±0.01
81	<sup>133</sup> Ba	3.32±0.02	1.03±0.01
122	<sup>57</sup> Co	3.12±0.02	0.98±0.01
136.4	<sup>57</sup> Co	3.04±0.02	0.94±0.01
302	<sup>133</sup> Ba	2.06±0.01	0.66±0.01
356	<sup>133</sup> Ba	1.88±0.01	0.61±0.01
511	<sup>22</sup> Na	1.52±0.01	0.50±0.01
662	<sup>137</sup> Cs	1.30±0.01	0.44±0.01
834	<sup>54</sup> Mn	1.15±0.01	0.40±0.01
898	<sup>88</sup> Y	1.11±0.01	0.37±0.01
1173	<sup>60</sup> Co	0.98±0.01	0.34±0.01
1275	<sup>22</sup> Na	0.92±0.01	0.32±0.01
1332	<sup>60</sup> Co	0.91±0.01	0.31±0.01
1836	<sup>88</sup> Y	0.73±0.01	0.26±0.01

Table 4.3: Simulated values for the detector efficiency  $\varepsilon_{sim}$  for different geometries. To test the influence of the geometry an asymmetric setup was created by placing the point-like gamma source 2 cm off the axis of the detector system in a distance to the entrance window given above the last two columns. Again, the source emits the gamma rays into  $4\pi$  solid angle.

point-like calibration sources with very low and well-known activity are needed. These requirements on the sources turned out to be a major problem: typically, the activities of the calibration sources are only known to  $\pm 30\%$  [AEA01] and exceed some hundreds of Bequerels, leading to excessive pile-up in the germanium detector when placed close to the entrance window. For that reasons eventually only four calibration sources were used for the measurements:  $^{133}\text{Ba}$  with a remaining activity of 2.6 kBq,  $^{57}\text{Co}$  (4.3 kBq),  $^{60}\text{Co}$  (1.6 kBq) and  $^{88}\text{Y}$  (3.1 Bq), see fig. 4.3. The isotopes  $^{241}\text{Am}$  and  $^{137}\text{Cs}$  have long half-lives (432.2 yr and 30.23 yr, respectively), whereby all sources of this type had too much activity left to be used for the measurements. The only  $^{22}\text{Na}$  source with suitable activity was not point-like, but a liquid solution in a glass bottle making it impossible to create the correct geometry.



Figure 4.3: *Calibration sources used for measuring the detector efficiency. From left to right:  $^{57}\text{Co}$ -source,  $^{88}\text{Y}$ -source,  $^{133}\text{Ba}$ -source and  $^{60}\text{Co}$ -source. The radioactive material is a small metallic dot in the centre of each calibration source (only visible for  $^{57}\text{Co}$  and  $^{88}\text{Y}$ ). The size of the  $^{60}\text{Co}$ -source is nearly the same as a 1 Euro coin.*

The tables 4.4 and 4.5 give the measured detector efficiencies, again for a symmetric and an asymmetric setup.

<i>energy</i> [keV]	<i>isotope</i>	<i>Measured efficiency <math>\varepsilon_{meas}</math> [%]</i> <i>centered on the symmetry axis</i>		
		<i>10 mm</i>	<i>100 mm</i>	<i>200 mm</i>
26	<sup>241</sup> Am	-	-	-
33	<sup>241</sup> Am	-	-	-
60	<sup>241</sup> Am	-	-	-
81	<sup>133</sup> Ba	4.73±1.46	1.04±0.33	0.31±0.10
122	<sup>57</sup> Co	12.34±3.72	1.61±0.49	0.48±0.15
136.4	<sup>57</sup> Co	12.62±3.86	1.60±0.50	0.49±0.16
302	<sup>133</sup> Ba	12.43±3.80	1.64±0.52	0.52±0.17
356	<sup>133</sup> Ba	11.40±3.46	1.49±0.46	0.48±0.16
511	<sup>22</sup> Na	-	-	-
662	<sup>137</sup> Cs	-	-	-
834	<sup>54</sup> Mn	-	-	-
898	<sup>88</sup> Y	5.53±1.90	0.87±0.33	0.29±0.11
1173	<sup>60</sup> Co	7.19±2.19	1.23±0.38	0.42±0.14
1275	<sup>22</sup> Na	-	-	-
1332	<sup>60</sup> Co	6.68±2.03	1.16±0.36	0.39±0.13
1836	<sup>88</sup> Y	2.86±1.02	0.53±0.21	0.18±0.06

Table 4.4: *Measured values for the detector efficiency  $\varepsilon_{meas}$  for different geometries using the calibration sources mentioned above. The quoted errors are calculated from the  $1\sigma$  uncertainties of the Gaussian fit to the peaks in the measured spectra and the uncertainty of the activity of the calibration sources of  $\pm 30\%$  [AEA01]. The errors of the geometry or effects like pile-up are not taken into account.*

		<i>Measured efficiency <math>\varepsilon_{meas}</math> [%]</i> <i>2 cm off-axis</i>	
<i>energy</i> <i>[keV]</i>	<i>isotope</i>	<i>100 mm</i>	<i>200 mm</i>
26	<sup>241</sup> Am	-	-
33	<sup>241</sup> Am	-	-
60	<sup>241</sup> Am	-	-
81	<sup>133</sup> Ba	1.01±0.32	0.31±0.10
122	<sup>57</sup> Co	1.59±0.49	0.47±0.15
136.4	<sup>57</sup> Co	1.63±0.51	0.48±0.15
302	<sup>133</sup> Ba	1.59±0.50	0.51±0.16
356	<sup>133</sup> Ba	1.47±0.45	0.47±0.15
511	<sup>22</sup> Na	-	-
662	<sup>137</sup> Cs	-	-
834	<sup>54</sup> Mn	-	-
898	<sup>88</sup> Y	0.69±0.27	0.25±0.10
1173	<sup>60</sup> Co	1.19±0.37	0.41±0.13
1275	<sup>22</sup> Na	-	-
1332	<sup>60</sup> Co	1.13±0.35	0.39±0.13
1836	<sup>88</sup> Y	0.49±0.20	0.15±0.06

Table 4.5: *Measured values for the detector efficiency  $\varepsilon_{meas}$  for different geometries in an asymmetric setup. Again, the quoted errors include the uncertainty of the Gaussian fit and the uncertainty of the source activity.*

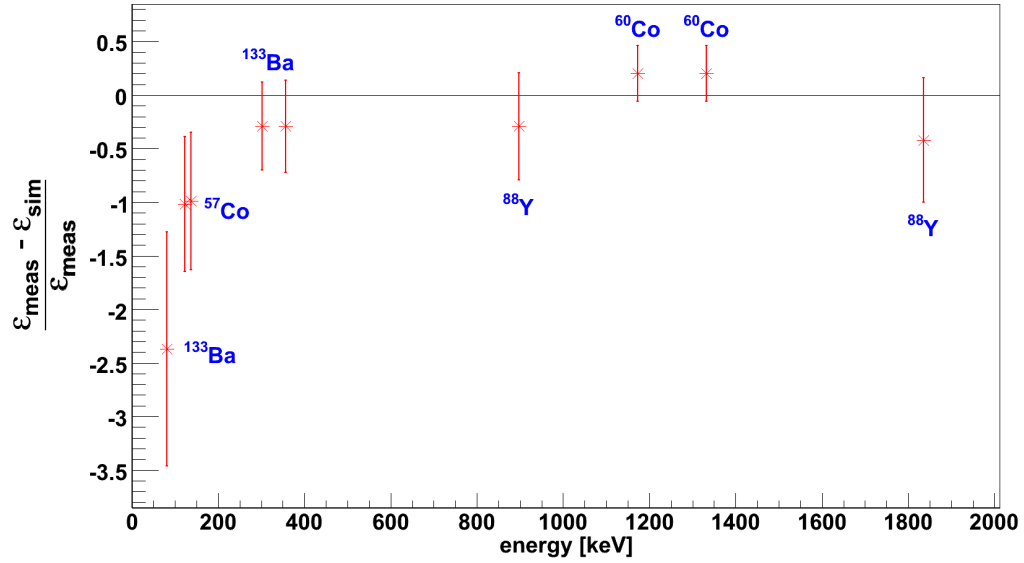


Figure 4.4: Comparison between the measured and the simulated detector efficiencies for the symmetrical setup. The ratio  $\frac{\epsilon_{\text{meas}} - \epsilon_{\text{sim}}}{\epsilon_{\text{meas}}}$  is plotted as a function of the gamma energy. The data set in red displays the values obtained for a source position 10 cm in front of the entrance window. The error bars are calculated by linear error propagation from the errors given in the tables 4.2 and 4.4. Obviously, the errors are dominated by systematic errors, in this case the uncertainty of the source activity. The uncertainty of the geometry is again not taken into account. For the symmetric setup with a source position at 20 cm, as well as the two asymmetric geometries, the plots look alike. The systematic deviation at low energies is most likely due to absorption, see text.

Obviously, the measured values for the detector efficiency show a systematic deviation from the simulated ones for energies below  $\sim 200$  keV. This is displayed in fig. 4.4, where  $\frac{\epsilon_{\text{meas}} - \epsilon_{\text{sim}}}{\epsilon_{\text{meas}}}$  is plotted as a function of the gamma energy for the symmetrical setup with the gamma source at a distance of 10 cm to the entrance window.

These deviations might have several reasons. As already mentioned above, the activities of the calibration sources are known only to a precision of about  $\pm 30\%$ . It is a noticeable fact in fig. 4.4, that the measured detector efficiencies are smaller than the simulated ones for the  $^{133}\text{Ba}$ , the  $^{57}\text{Co}$  and the  $^{88}\text{Y}$  source, while they are larger for the  $^{60}\text{Co}$  source. Furthermore, for gamma energies higher than  $\gtrsim 200$  keV the values are compatible with zero, when taking into account the uncertainty of the source activity of 30%. This in-

dicates, that the biggest uncertainty indeed comes from the activity of the calibration sources.

Another striking point is the energy-dependence of the detector efficiency: while the simulation predicts the maximum of  $\varepsilon_{\text{sim}}$  at an energy of about 60 to 81 keV (see tables 4.2 and 4.3), the measured maximum lies much higher, somewhere in between the 136.4 keV line of  $^{57}\text{Co}$  and the 302 keV line of  $^{133}\text{Ba}$  (tables 4.4 and 4.5). This could be caused by a layer of inactive germanium on the edge of the germanium crystal, which is not included in the simulation, as its thickness is unknown. Such a layer mainly has an impact on the efficiency at lower energies, while gamma rays with higher energies are more likely to reach the inner active part of the crystal. For example, the half-thickness for absorption in germanium is 1.9 mm for a photon energy of 100 keV, but more than 2 cm for an energy of 1 MeV [Fir96]. Thus, neglecting the inactive germanium layer in the simulation could explain the huge deviation of  $\varepsilon_{\text{sim}}$  from  $\varepsilon_{\text{meas}}$  for the 81 keV gamma line of  $^{133}\text{Ba}$ , as seen in tabs. 4.2 through 4.5 and fig. 4.4.

Furthermore, the detector geometry used in the simulation (fig. 3.3) might slightly deviate from the actual one, leading to a further discrepancy between simulation and measurement: for some germanium detectors it was observed, that the crystals are not mounted straight-lined in their housings, but slightly tilted [Kro07]. The correct detector geometry could be determined by x-raying the germanium detector.

The measured detector efficiencies for source positions close to the entrance window, particularly for 1 cm distance, suffer in addition from pile-up due to the too high activity of the sources used (except for the  $^{88}\text{Y}$ -source with only 3.1 Bq). Pile-up arises as sum-peaks in the recorded spectra, leading to a reduction of the measured efficiency. It can only be avoided by using gamma sources with activities below  $\sim 1$  kBq.

Minor contributions to the uncertainty of  $\varepsilon_{\text{meas}}$  come from the accuracy of the positioning of the calibration source within the detector system (estimated to be  $\pm 1$  mm), self-absorption of the gamma rays in the calibration source (mainly relevant for small gamma energies), the efficiency of the read-out electronics and the exactness of the Gaussian fit (done by the software package Genie-2000) in presence of a high continuous background.

Last but not least, the physics model used in the simulation might be inaccurate in some way: the simulation does not contain all interactions and particles, which might occur in reality. Furthermore, the used materials are taken from the GEANT4 database, which might contain some errors, for example in the natural abundances of the stable isotopes of a certain element. The total cross-sections of the different interactions for gamma

rays are implemented only in a simplified parameterised form<sup>2</sup>. All these effects could lead to (small) deviations of the simulated efficiencies  $\varepsilon_{\text{sim}}$  from the measured ones, even in case the detector geometry was implemented completely correct in the simulation.

Qualitatively correct in the simulated values is the behaviour of the detector efficiency for asymmetric setups: here the simulated as well as the measured efficiencies are a bit smaller for the off-axis configuration than for the symmetric setup.

In summary, the simulation seems to be applicable for gamma energies  $\gtrsim 200$  keV, but suffers from some problems for smaller energies. Most likely, the deviations of the simulated efficiencies from the measured ones are caused by absorption, like the inactive germanium layer at the detector surface. However, to obtain better quantitative information on the size of the errors, the measurements of the detector efficiency must be performed using calibration sources with very well-known and lower activity.

---

<sup>2</sup>Thus it is possible to calculate the cross-sections using only atomic numbers, mass numbers, densities and radiation lengths of the given materials [CER94].

# Chapter 5

## Results and discussion of the low-background gamma spectroscopy

### 5.1 Ambient background activity

As already mentioned in section 3.1, great efforts have to be made in order to keep the background, coming from various natural sources, at a low level<sup>1</sup>. Figure 5.1 shows two spectra, both recorded with the germanium detector over a measuring time of  $\sim 230,000$  seconds without any artificial source. The curve in green was recorded without using any of the two active veto systems (anti-Compton veto and muon-veto), but only the passive shieldings (lead shielding, PVC-box flushed with nitrogen and the overburden of the underground laboratory). Two major contributions to the natural background can be distinguished:

- ***Gamma lines:*** The sharp gamma lines, which can be seen in the spectrum, originate from several different sources:
  - Gamma lines from  $^{238}\text{U}$  and  $^{232}\text{Th}$  and their daughter isotopes. These two long-lived isotopes are omnipresent in the detector and shielding materials as well as in the surrounding laboratory. Among them are also lines originating from radon (and its daughters), which has not yet been flushed out of the plastic box. The high-energetic lines above  $\sim 1$  MeV (mainly from  $^{214}\text{Bi}$  and  $^{208}\text{Tl}$ ) originate also from sources in the laboratory and penetrate

---

<sup>1</sup>In addition, all parts of the detector have been carefully cleaned before the first measurements.

through the lead shielding into the germanium detector. This was recognised, when the lead shielding on top of the detector system was increased from 5 cm to 15 cm, thereby decreasing the intensity of the high-energetic lines by about 50%.

- The 1.4 MeV gamma line from the primordial isotope  $^{40}\text{K}$ . This potassium isotope has a natural abundance of 0.0117% and is - amongst others - probably contained in the sodium-iodide crystals of the anti-Compton veto.
- The 46.5 keV gamma line from  $^{210}\text{Pb}$ , contained in the lead shielding.
- Gamma lines originating from excited states of different germanium isotopes. These excited states are populated either by muons or by neutrons (see also appendix D).
- The 511 keV gamma line and less prominent the 1022 keV gamma line from positron annihilation. Positrons are created in pair-production processes of muons or high-energetic gamma quanta.
- X-ray fluorescence lines from lead, around 75 keV, excited by muons or gamma rays (see appendix D). These lines also appear after internal conversion, which occurs with high probability after the decays of radioactive lead isotopes [Fir96], for example  $^{212}\text{Pb}$  and  $^{214}\text{Pb}$ .

• ***Continuous background:***

- The Landau distribution ( $\propto \exp\{-\frac{1}{2}(x + e^{-x})\}$ ) mainly originating from the bremsstrahlung of the  $\delta$ -electrons released by cosmic muons [Hen99].
- Compton scattering events of gamma rays depositing not the full gamma energy within the germanium detector.
- Bremsstrahlung from electrons released in beta-decays of natural radioactive isotopes.

The spectrum marked in blue in fig. 5.1 was recorded using both active veto systems. Noticeable is the great reduction of the continuous background. Most of the Compton scattering events are eliminated by the anti-Compton veto, except for those which are scattered into the solid angle at the backside of the germanium detector, being uncovered by the anti-Compton veto, or those events depositing an amount of energy in the sodium-iodide scintillation crystals, which is below the detector threshold (start of the PMT dark noise

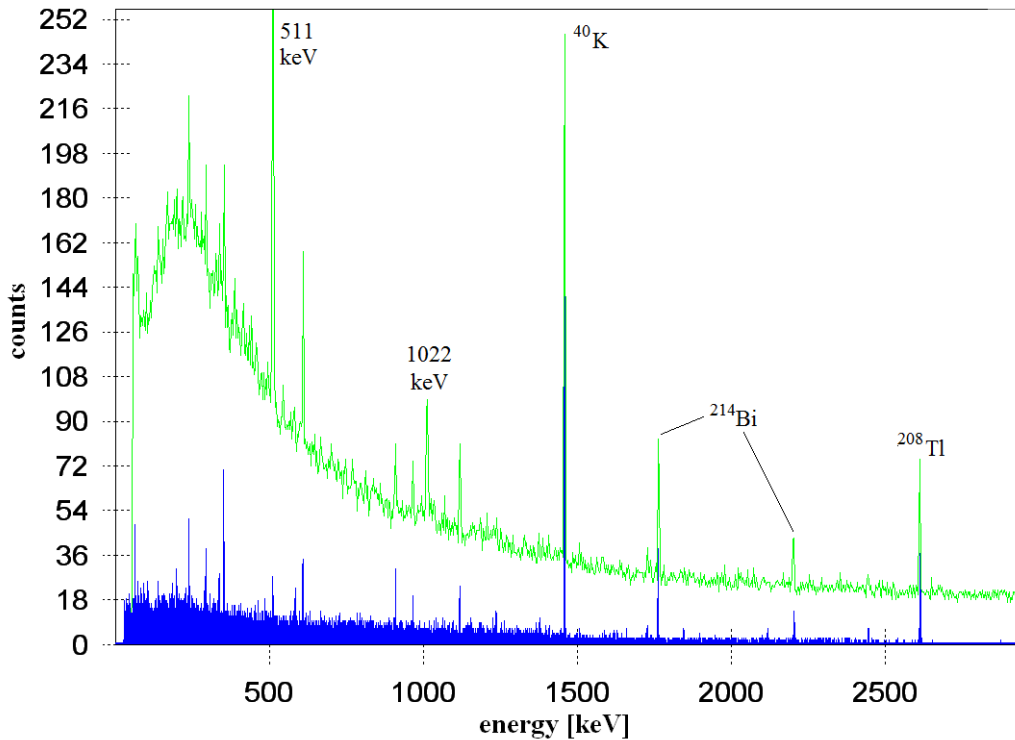


Figure 5.1: *Two spectra, both recorded with the germanium detector over  $\sim 230,000$  seconds without any artificial source. The spectrum in green was recorded without using the active veto systems, the spectrum in blue with full active veto. A detailed summary of the gamma lines, which can be seen, is given in appendix D.*

at about 15 keV, see section 3.3.2). The bremsstrahlung events from the  $\delta$ -electrons released by cosmic muons are erased by the muon-veto system. The main contribution to the still remaining continuous background comes from the bremsstrahlung of the beta decay electrons [Hen99]. But not only the continuous background is reduced, also some of the gamma lines vanish when using the active veto systems. Most eye-catching is the reduction of the 511 keV and the 1022 keV positron annihilation lines. From that reduction it is possible to estimate a muon detection efficiency of the plastic scintillator panels to  $> 97.7\%$ . The X-ray fluorescence lines from lead are also greatly reduced, when switching on the muon-veto. Last but not least all gamma lines of excited germanium states with half-lives shorter than  $\sim 20 \mu\text{s}$  vanish, as they are populated by muons or neutrons released in muon spallation processes. The figures 5.2 and 5.3 show again the background spectrum with complete identification of the most prominent remaining gamma lines.

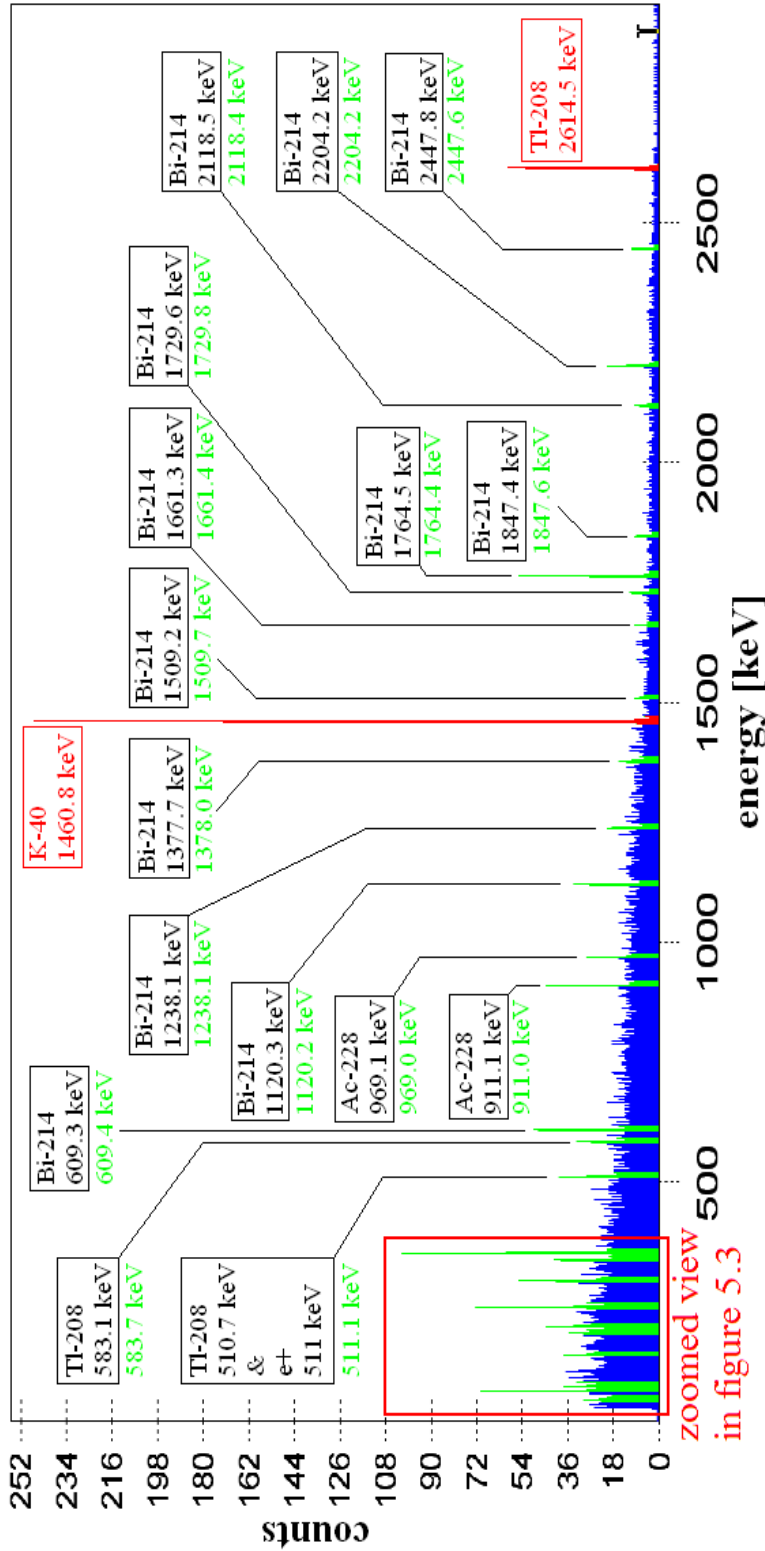


Figure 5.2: Background spectrum, recorded with the germanium detector over a measuring time of 340,000 seconds with full active veto systems. The most prominent remaining gamma lines are tagged with framed boxes giving the isotope and the literature value of the energy of the line. The numbers in green give the peak position of the Gaussian fit applied to each line in the spectrum, which was calibrated using a linear interpolation between the gamma line of  $^{40}\text{K}$  at 1460.8 keV and the 2614.5 keV line of  $^{208}\text{Tl}$  (both marked in red). A zoomed view of the low-energy part of the spectrum can be found in fig. 5.3.

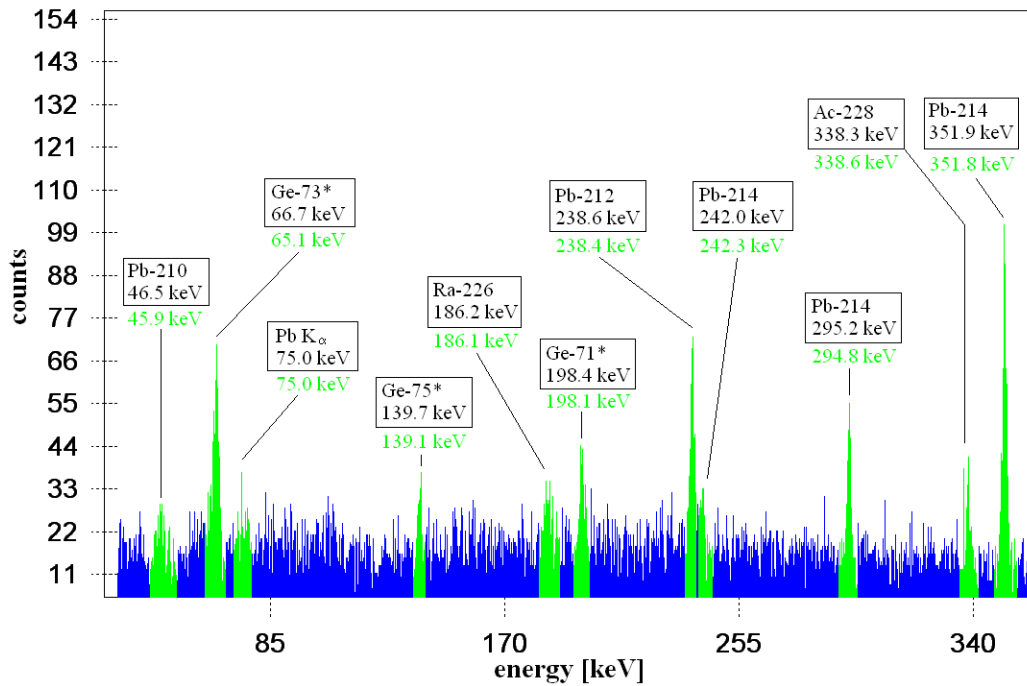


Figure 5.3: *Low-energy part of the background spectrum shown in fig. 5.2. The framed boxes again give the isotope with its literature value for the energy, while the numbers in green give the fitted peak positions. The energy calibration is the same as in fig. 5.2.*

Table 5.1 lists the number of counts in the background spectra, once without the active veto systems and once with full active veto.

<i>energy range</i> [keV]	<i>0-500</i>	<i>500-1000</i>	<i>1000-1500</i>	<i>&gt; 1500</i>
<i>without veto</i>	35.485 cpm	17.703 cpm	8.269 cpm	8.050 cpm
<i>with full veto</i>	1.910 cpm	0.692 cpm	0.581 cpm	0.226 cpm

Table 5.1: *Number of background counts in the spectra recorded with the germanium detector in units of counts per minute (cpm) for different energy ranges. The reduction in the number of counts when using the active veto systems is mainly due to the suppression of the continuous background originating from cosmic muons and Compton-scattering events.*

## 5.2 Performed measurements and results

### 5.2.1 Investigated samples

In the context of the low-background gamma spectroscopy for DOUBLE CHOOZ several samples of organic liquids, scintillators and mineral oils, and additional wave-length shifters were investigated. These samples are either liquids or powders, making it necessary to use plastic containers to hold the samples during the measurements. Therefore, first of all these containers were measured in blank runs without any sample in order to determine their contribution to the radioactive background. Two different types of plastic containers were used: high-density polyethylene (short: PEHD) bottles with a volume of 100 ml and containers made of polytetrafluoroethylene ("Teflon", PTFE) with a volume of 60 ml. The latter are much more expensive but are needed, as some liquid scintillators are able to dissolve polyethylene.

In the following the results of the measurements will be presented in detail for the liquid scintillator LAB (linear alcyll benzene), which is most likely used in the inner veto system of the DOUBLE CHOOZ detectors (see section 2.2), the mineral oil tetradecane, used for dilution of the liquid scintillators, the primary wave-length shifter PPO (2,5-diphenyloxazole), and the secondary wave-length shifter bisMSB (1,4-bis-(o-methylstyryl)-benzole). Tables 5.2 to 5.5 give more details on these four materials.

Each of these samples was measured over a measuring time of  $\sim 1,000,000$  seconds (about 12 days) plus a  $\sim 48$  hours time span before each measurement for flushing the PVC-box with nitrogen. Although the dead-time of the

detector system due to the active veto is very small ( $\lesssim 0.6\%$ ), the results are corrected by this factor.

The analysis of the recorded spectra in terms of finding the gamma peaks was done using the automatic peak-search routine implemented in the CANBERRA Genie-2000 software package [GEN02]. This routine uses the second derivative for peak identification. All peaks found, which exceed a user-defined threshold in significance, are considered to be true gamma peaks. By this, statistical fluctuations of the continuous background are rejected from the list of gamma lines.

After the peak-search a Gaussian fit was applied to each identified gamma line, using the method of non-linear least-squares fits [GEN02]. The continuous background under the gamma peak is approximated by a step function (with a step length, which depends on the steepness of the background) and subtracted from the area of the peak. The number of counts in a given gamma line is set equal to the area of the peak determined by this algorithm. Furthermore, Genie-2000 calculates the  $1\sigma$ -uncertainty of this peak-area, which adds to the statistical error of the number of counts.

Tables 5.6 through 5.8 on pages 72-74 give a detailed overview over the peaks identified in each spectrum recorded and specify the number of counts in each peak normalised to 100,000 seconds of measuring time. The quoted errors are the  $1\sigma$ -uncertainties as calculated by Genie-2000. A detailed summary of the gamma lines, which are listed in these tables, is given in appendix D.

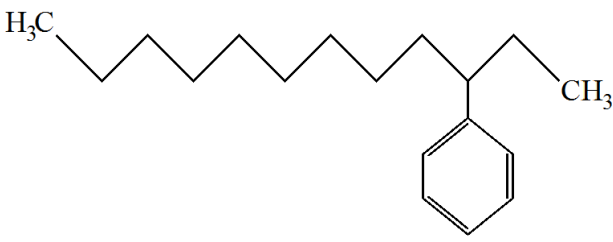
LAB	
	
<i>Linear alkyl benzene</i>	
<i>Sum formula</i>	$CH_3 - (CH_2)_n - CH(C_6H_5) - (CH_2)_m - CH_3$ $n+m = 7-10$
<i>sample mass</i>	88.67 g
<i>physical condition</i>	liquid
<i>type of product &amp; manufacturer</i>	P 550-Q CAS number: 68890-99-3 Petresa Canada Inc. (PCI) 5250 Bécancour Boulevard Bécancour (Québec) G9H 3X3, CANADA
<i>Intended use in DOUBLE CHOOZ</i>	Liquid scintillator candidate for the muon-veto system (inner veto)

Table 5.2: *Properties of the used LAB sample. Chemical structure, sum formula and physical condition are given, as well as the mass of the investigated sample. LAB is a candidate for the liquid scintillator in the inner veto of the DOUBLE CHOOZ detectors.*

TETRADECANE	
	
<i>Sum formula</i>	$C_{14}H_{30}$
<i>sample mass</i>	80.77 g
<i>physical condition</i>	liquid
<i>type of product &amp; manufacturer</i>	CAS number: 629-59-4 Petresa Campo de las Naciones Avda. del Partenón, 12 28042 Madrid, SPAIN
<i>Intended use in DOUBLE CHOOZ</i>	Mineral oil for liquid scintillator dilution

Table 5.3: *Properties of the used tetradecane sample. Chemical structure, sum formula and physical condition are given, as well as the mass of the investigated sample. Tetradecane is under investigation for dilution of the liquid scintillators in DOUBLE CHOOZ in order to increase the ratio of hydrogen atoms to carbon atoms. In this way, the number of free protons in the detectors can be increased.*

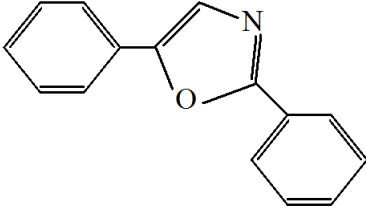
PPO	
	
<i>2,5-Diphenyloxazole</i>	
<i>Sum formula</i>	$C_{12}H_{11}NO$
<i>sample mass</i>	32.05 g
<i>physical condition</i>	dry chemical
<i>type of product &amp; manufacturer</i>	Aldrich D210404 CAS number: 92-71-7 Sigma-Aldrich Chemie GmbH Riedstr. 2 D-89555 Steinheim, GERMANY
<i>Intended use in DOUBLE CHOOZ</i>	Primary fluor (wave-length shifter)

Table 5.4: *Properties of the used PPO sample. Chemical structure, sum formula and physical condition are given, as well as the mass of the investigated sample. In order to decrease self-absorption and thus increase the light-yield, wave-length shifters (also called fluors) are added in small concentrations to the liquid scintillators. PPO is a primary fluor, this means its absorption band overlaps with the emission band of the liquid scintillator, while its emission band is red-shifted.*

bisMSB	
<i>1,4-bis-(o-Methylstyryl)-Benzole</i>	
<i>Sum formula</i>	$C_7H_7 - C_2H_2 - C_6H_4 - C_2H_2 - C_7H_7$
<i>sample mass</i>	25.83 g
<i>physical condition</i>	dry chemical
<i>type of product &amp; manufacturer</i>	Fluka 15090 CAS number: 13280-61-0 Sigma-Aldrich Chemie GmbH Riedstr. 2 D-89555 Steinheim, GERMANY
<i>Intended use in DOUBLE CHOOZ</i>	Secondary fluor (wave-length shifter)

Table 5.5: *Properties of the used bisMSB sample. Chemical structure, sum formula and physical condition are given, as well as the mass of the investigated sample. The absorption band of the secondary fluor bisMSB overlaps with the emission band of the primary fluor PPO. Hence, it further red-shifts the emitted light, making self-absorption in the liquid scintillator very unlikely.*

<i>line energy [keV]</i>	46.5	66.7	75.0	92.4	139.7	186.2
<i>without sample</i>	41±9	89±9	26±7	-	25±7	30±8
<i>PEHD</i>	26±3	121±6	15±4	-	34±4	23±4
<i>PTFE</i>	29±5	126±8	6±5	-	32±5	15±4
<i>LAB</i>	28±3	121±5	16±3	-	28±3	16±3
<i>Tetradecane</i>	25±3	107±6	31±4	8±3	37±4	18±4
<i>PPO</i>	32±3	94±5	20±3	-	32±3	19±3
<i>bisMSB</i>	36±3	118±5	7±3	6±3	31±3	19±3

<i>line energy [keV]</i>	198.4	238.6	295.2	300.1	338.3	351.9
<i>without sample</i>	35±8	51±8	51±7	-	21±7	106±8
<i>PEHD</i>	31±3	69±5	49±3	-	14±3	109±5
<i>PTFE</i>	35±5	50±6	48±5	-	19±4	101±7
<i>LAB</i>	25±3	49±4	49±3	2±2	15±2	113±4
<i>Tetradecane</i>	30±4	60±4	53±4	-	18±3	104±5
<i>PPO</i>	27±3	55±4	35±3	6±2	14±2	102±4
<i>bisMSB</i>	35±3	46±4	46±3	5±2	19±3	102±4

<i>line energy [keV]</i>	463.0	510.7	583.1	609.3	665.5	727.2
<i>without sample</i>	-	53±6	41±6	72±6	-	-
<i>PEHD</i>	-	16±3	13±2	36±3	4±1	9±2
<i>PTFE</i>	9±3	9±3	20±3	44±4	3±3	7±3
<i>LAB</i>	-	12±2	15±2	42±3	-	12±2
<i>Tetradecane</i>	4±2	18±3	25±3	72±3	3±2	9±2
<i>PPO</i>	-	19±2	15±2	37±3	5±1	13±2
<i>bisMSB</i>	-	14±2	18±2	50±3	6±1	14±2

Table 5.6: The gamma lines found in the analysis of the different investigated samples are listed here for the low-energetic part ( $\leq 727.2$  keV). For each sample and each line the number of counts, which is the area under the Gaussian fit curve applied to the respective gamma peak in the spectrum, and the  $1\sigma$ -uncertainty are given (rounded to integers). The token "-" indicates, that the gamma line is not visible in the spectrum, or, at least, below the significance threshold.

<i>line energy</i> [keV]	768.4	785.4	794.9	860.4	911.1	964.6
<i>without sample</i>	-	-	-	-	55±5	-
<i>PEHD</i>	4±2	4±1	-	3±1	53±3	1±2
<i>PTFE</i>	5±3	8±3	-	9±3	53±4	-
<i>LAB</i>	2±1	3±1	-	3±1	48±3	-
<i>Tetradecane</i>	6±2	1±2	5±2	7±2	55±3	4±2
<i>PPO</i>	5±2	-	-	5±1	48±3	-
<i>bisMSB</i>	5±1	4±1	3±1	1±1	48±3	-

<i>line energy</i> [keV]	969.1	1001.0	1120.3	1238.1	1377.7	1408.0
<i>without sample</i>	26±4	-	30±4	9±3	13±4	5±2
<i>PEHD</i>	21±3	4±1	14±2	9±2	13±2	6±1
<i>PTFE</i>	24±4	-	20±3	9±2	12±3	-
<i>LAB</i>	27±2	3±1	18±2	7±1	10±2	4±1
<i>Tetradecane</i>	21±3	3±1	35±3	-	11±2	6±1
<i>PPO</i>	29±2	-	19±2	11±2	12±2	6±1
<i>bisMSB</i>	21±2	4±1	24±2	10±2	11±2	3±1

<i>line energy</i> [keV]	1460.8	1495.9	1509.2	1587.9	1620.6	1630.6
<i>without sample</i>	364±9	-	-	6±2	-	-
<i>PEHD</i>	361±7	4±1	4±1	9±1	2±1	4±1
<i>PTFE</i>	369±11	-	3±1	11±2	-	-
<i>LAB</i>	334±6	2±1	3±1	4±1	4±1	3±1
<i>Tetradecane</i>	324±6	-	6±1	6±1	2±1	4±1
<i>PPO</i>	342±6	2±1	3±1	11±1	1±1	3±1
<i>bisMSB</i>	351±6	3±1	2±1	5±1	4±1	4±1

Table 5.7: The gamma lines found in the analysis of the different investigated samples are listed here for the medium-energetic part ( $768.4 \text{ keV} \leq E \leq 1630.6 \text{ keV}$ ). For each sample and each line the number of counts, which is the area under the Gaussian fit curve applied to the respective gamma peak in the spectrum, and the  $1\sigma$ -uncertainty are given (rounded to integers). The token "-" indicates, that the gamma line is not visible in the spectrum, or, at least, below the significance threshold.

<i>line energy [keV]</i>	1661.3	1729.6	1764.5	1847.4
<i>without sample</i>	-	9±2	64±4	6±2
<i>PEHD</i>	2±1	8±1	53±3	7±1
<i>PTFE</i>	-	10±2	54±4	6±1
<i>LAB</i>	1±1	8±1	50±2	5±1
<i>Tetradecane</i>	-	8±1	49±2	6±1
<i>PPO</i>	-	7±1	46±2	8±1
<i>bisMSB</i>	2±1	11±1	51±2	6±1

<i>line energy [keV]</i>	2118.5	2204.2	2447.8	2614.5
<i>without sample</i>	-	13±2	-	69±4
<i>PEHD</i>	4±1	16±2	6±1	52±3
<i>PTFE</i>	6±1	15±2	5±1	53±4
<i>LAB</i>	4±1	16±1	4±1	42±2
<i>Tetradecane</i>	5±1	12±1	3±1	62±3
<i>PPO</i>	5±1	16±1	4±1	50±2
<i>bisMSB</i>	5±1	18±1	4±1	51±2

Table 5.8: *The gamma lines found in the analysis of the different investigated samples are listed here for the high-energetic part ( $\geq 1661.3$  keV). For each sample and each line the number of counts, which is the area under the Gaussian fit curve applied to the respective gamma peak in the spectrum, and the  $1\sigma$ -uncertainty are given (rounded to integers). The token "-" indicates, that the gamma line is not visible in the spectrum, or, at least, below the significance threshold.*

### 5.2.2 Calculation of radioactivities

From the number of counts in a given peak, the activity of the corresponding gamma line can be calculated using eq. (4.1). In the case of the measured samples, the number of counts in a certain peak is very often compatible with or even below the number of counts in the corresponding peak in the blank run within the  $1\sigma$  error bars. To calculate an upper limit for the number of counts coming from the sample in the respective gamma line in this case, a special method is applied: a Gaussian error distribution curve  $P(x)$  is set up around the difference in the counts within a peak between the runs with sample and without sample. Thereby, its root mean square deviation is computed from the  $1\sigma$ -uncertainties of the peak-areas via quadratic error propagation (see fig. 5.4):

$$P(x) = \frac{1}{\sqrt{2\pi} \cdot \sigma} \exp \left\{ -\frac{(x - \mu)^2}{2\sigma^2} \right\} \quad (5.1)$$

with

$$\sigma = \sqrt{\sigma_{sample}^2 + \sigma_{blank}^2} \quad (5.2)$$

and

$\mu$ : counts in the peak with sample minus counts in the peak without sample

$x$ : difference in counts

$\sigma_{sample}$ : uncertainty of the peak-area with sample

$\sigma_{blank}$ : uncertainty of the peak-area in the blank run

Now, the upper limit  $N_s$  for the number of counts, originating from the sample itself, can be calculated for a confidence level of 90% by integrating eq. (5.1) [PDG90]:

$$\frac{\int_0^{N_s} P(x) \cdot dx}{\int_0^{\infty} P(x) \cdot dx} \stackrel{!}{=} 0.9 \quad (5.3)$$

This is again displayed in fig. 5.4. The limit  $N_s$  is chosen in such a manner, that the blue shaded area covers 90% of the total area under the

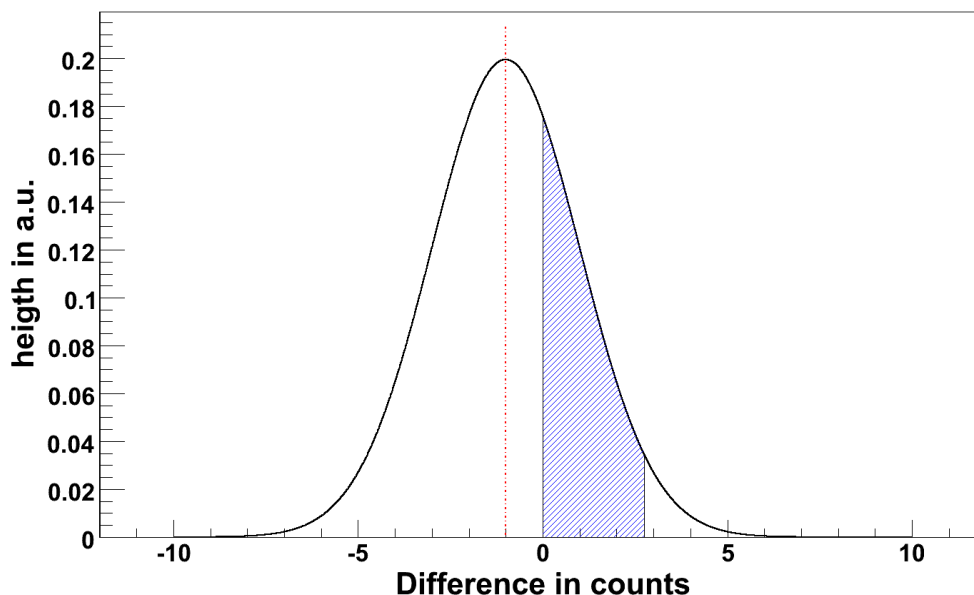


Figure 5.4: *Gaussian error distribution curve for determining the upper limit of the number of counts originating from the sample. The bell-shaped curve is centered around the difference in counts within a peak between the runs with sample and without sample (red line), in this case taken to be negative. The area shaded in blue covers 90% of the area under the error curve in the physically allowed region. Its upper limit gives the maximal number of counts from the sample for 90% C.L. [PDG90].*

Gaussian error distribution curve in the physically allowed region (between 0 and  $\infty$ ).

A great advantage of this method is, that it passes continuously into the method normally applied to Gaussian distributed values for the calculation of upper limits for a given confidence level, when the difference in counts  $\mu$  goes to zero.

In the case of gamma lines, which do not appear in the measured spectra because of lack of intensity (this is, for example, the case for the isotopes of the  $^{235}\text{U}$ -decay chain, which show up neither in the blank runs nor in the spectra recorded with a sample), the same method is applied. Here, as input the number of counts of the continuous background in an interval  $\pm 1$  FWHM (linearly interpolated from neighbouring peaks) around the position of the expected peak is taken. The square-root of this number of counts is taken as uncertainty.

For many radioactive isotopes the de-excitation after an alpha- or beta-decay takes place via gamma cascades, this means multiple gamma quanta are emitted (nearly) at once. If one of these gamma quanta deposits its energy in the germanium detector, while another one creates a signal in the anti-Compton veto system, this leads to a veto signal, erasing the event from the spectrum recorded with the germanium detector. Therefore, some attention has to be paid to the question, which lines can be used for the determination of the activity of a certain isotope. Suitable lines should come from a transition from an excited state  $E_1$  directly into the ground state  $E_0$  of the daughter isotope, not being followed by further gamma rays. Furthermore, the excited state  $E_1$ , the gamma line is originating from, should not be populated (or at least only very little) from states with higher energies, again to avoid a veto. In an ideal situation, the probability for  $E_1$  to be directly populated after the decay of the mother isotope is quite high. Thus the intensity of the corresponding gamma line is high, making it easier to detect. Appendix F shows the schemes of three different isotopes as examples:  $^{212}\text{Pb}$ , where any effects of gamma cascades can be neglected,  $^{214}\text{Bi}$ , where only some high-energetic gamma lines are suitable and  $^{208}\text{Tl}$ , having no adequate transition.

In detail, the following gamma lines from the three different decay chains (see appendix E) satisfy these requirements:

- ***Th-232 decay chain:*** 969.1 keV, 911.1 keV, 1587.9 keV (all three appearing in the decay of  $^{228}\text{Ac}$ ), 84.4 keV ( $^{228}\text{Th}$ ), 238.6 keV ( $^{212}\text{Pb}$ ), 727.2 keV and 1620.6 keV (both from  $^{212}\text{Bi}$ )
- ***U-235 decay chain:*** 205.3 keV ( $^{235}\text{U}$ ), 84.2 keV ( $^{231}\text{Th}$ ), 330.1 keV ( $^{231}\text{Pa}$ ), 286.1 keV and 334.4 keV (both from  $^{227}\text{Th}$ ), 269.6 keV ( $^{223}\text{Ra}$ ), 401.8 keV and 271.2 keV (both from  $^{219}\text{Rn}$ ), 831.8 keV ( $^{211}\text{Pb}$ )
- ***U-238 decay chain:*** 92.4 keV and 92.8 keV (both from  $^{234}\text{Th}$ ), 1001.0 keV ( $^{234}\text{Pa}$ ), 186.2 keV ( $^{226}\text{Ra}$ ), 351.9 keV and 295.2 keV (both from  $^{214}\text{Pb}$ ), 2447.8 keV, 2204.2 keV, 2118.5 keV, 1847.4 keV and 1764.5 keV (all five from  $^{214}\text{Bi}$ ), 46.5 keV ( $^{210}\text{Pb}$ )

All other gamma lines are either part of a gamma cascade or hidden behind a much more prominent line of another isotope. Furthermore, some isotopes cannot be used for an analysis, as they do not emit gamma rays at all after their decay, or the intensity of the gamma rays is very low due to a high probability for internal conversion (see appendix E).

From the suitable gamma lines the respective activities of the isotopes in the sample can be calculated using eq. (4.1). To obtain information on the

investigated materials independent from the mass of the used sample  $M_{\text{sample}}$ , the results are given as activity per mass unit:

$$\frac{A}{M_{\text{sample}}} = \frac{N_s}{t \cdot \varepsilon_{\text{Det}} \cdot P \cdot M_{\text{sample}}} \quad (5.4)$$

Again,  $N_s$  denotes the number of counts in the gamma peak coming from the sample,  $t$  the measuring time,  $P$  the relative intensity of the gamma line and  $\varepsilon_{\text{Det}}$  the detector efficiency.

In case, that the limit of the activity for one isotope can be calculated from different gamma lines, the quoted values are the weighted averages of the results obtained for the single lines [Bev69]:

$$\langle A \rangle = \left( \sum_{i=1}^n \frac{A_i}{\sigma_i^2} \right) \cdot \left( \sum_{i=1}^n \frac{1}{\sigma_i^2} \right)^{-1} \quad (5.5)$$

Herein  $A_i$  denote the activities of the single gamma lines,  $\sigma_i$  their errors and  $n$  the number of lines used for the analysis of this isotope. The error of  $\langle A \rangle$  is given by

$$\langle \sigma \rangle = \sqrt{\left( \sum_{i=1}^n \frac{1}{\sigma_i^2} \right)^{-1}} \quad (5.6)$$

The advantage of the weighted average is, that it gives more weight to smaller values (in case the relative errors for all values are always the same or quite the same) and thus the most stringent upper limit of all the single gamma lines has the biggest impact on the combined result.

Tables 5.9 through 5.14 on pages 80-85 display the results obtained for the investigated samples, as well as the results for the used plastic containers using eq. (5.4) for 90% C.L. The quoted limit on the activity for the whole decay chain is in each case again the weighted average of the activities of the different isotopes contained in these chains. This approach requires radioactive equilibrium within the decay chains, which is assumed to be existent. All results are given in the format activity per mass unit (in units of Bq/kg) and as a mass concentration (given in g/g) (see eq. 4.2).

The quoted uncertainties of the activity were calculated by linear error propagation from the uncertainties of the measuring time  $t$  (Genie-2000 determines the measuring time with an accuracy of 0.01 seconds), the detector efficiency  $\varepsilon_{\text{Det}}$ , the sample mass  $M_{\text{sample}}$  (measured with an accuracy of 0.01 grammes) and the relative gamma intensity  $P$  (errors taken from [Fir96], normally in the range of 1-10%):

$$\frac{\Delta A}{A} = \frac{\Delta t}{t} + \frac{\Delta \varepsilon_{Det}}{\varepsilon_{Det}} + \frac{\Delta M_{sample}}{M_{sample}} + \frac{\Delta P}{P} \quad (5.7)$$

The detector efficiency  $\varepsilon_{Det}$  and its uncertainty were determined as follows: first of all, the weighted average of  $\frac{\varepsilon_{meas} - \varepsilon_{sim}}{\varepsilon_{meas}}$  and its uncertainty were calculated analogously to equations (5.5) and (5.6), using the values given in tables 4.2 through 4.5 on pages 53-57. As already explained in chapter 4.2, the simulation is only applicable for energies above  $\gtrsim 200$  keV. That is why only the two lines from  $^{88}\text{Y}$  (898 keV and 1836 keV), the two lines from  $^{60}\text{Co}$  (1173 keV and 1332 keV) and the two high-energetic lines from  $^{133}\text{Ba}$  (302 keV and 356 keV) were used for this calculation. Furthermore, in order to avoid systematic effects from pile-up, the series of measurements performed for a position of the calibration sources 1 cm in front of the entrance window of the germanium detector was discarded. The result of this calculation is

$$\left\langle \frac{\varepsilon_{meas} - \varepsilon_{sim}}{\varepsilon_{meas}} \right\rangle = -0.0129 \pm 0.0755 . \quad (5.8)$$

Thereafter,  $\varepsilon_{sim}$  was determined for each sample and each gamma energy with the Monte-Carlo simulation, using the correct geometry (the gamma rays are started at a randomly chosen point within the sample volume with a randomly created direction of flight) and accurate properties of the sample materials. This value was afterwards inserted into the weighted average for  $\frac{\varepsilon_{meas} - \varepsilon_{sim}}{\varepsilon_{meas}}$  given in eq. (5.8). Solving this equation for  $\varepsilon_{meas}$  gave the detector efficiency  $\varepsilon_{Det}$  and its uncertainty ( $\sim 8\%$ ) used later on for the analysis of the gamma spectra of the investigated samples. Due to this procedure, the error of  $\varepsilon_{Det}$  was now asymmetric, leading eventually to asymmetric errors of the calculated activities.

Because of the systematic deviation of the simulated detector efficiencies from the measured ones (see fig. 4.4) for low energies, the analysis presented here was done only for gamma lines, whose energy exceeds 186.2 keV (line from  $^{226}\text{Ra}$ ). The other lines, being also suitable for an analysis, with an energy less than this value (see itemisation on page 77) should also be analysed after an improvement of the Monte-Carlo simulation for consistency checks.

RESULTS FOR THE PLASTIC CONTAINERS (90% C.L.)		
<i>isotope</i>	<i>PEHD</i>	<i>PTFE</i>
<b>K-40</b>	$< 3.19^{+0.30}_{-0.27}$ Bq/kg $< 12.3^{+1.2}_{-1.0} \cdot 10^{-9}$ g/g	$< 2.18^{+0.20}_{-0.18}$ Bq/kg $< 8.41^{+0.77}_{-0.69} \cdot 10^{-9}$ g/g
$^{228}\text{Ac}$	$< 0.537^{+0.038}_{-0.034}$ Bq/kg $< 6.49^{+0.46}_{-0.41} \cdot 10^{-21}$ g/g	$< 0.287^{+0.020}_{-0.018}$ Bq/kg $< 3.47^{+0.24}_{-0.22} \cdot 10^{-21}$ g/g
$^{212}\text{Pb}$	$< 0.452^{+0.040}_{-0.035}$ Bq/kg $< 8.79^{+0.78}_{-0.68} \cdot 10^{-21}$ g/g	$< 0.109^{+0.010}_{-0.008}$ Bq/kg $< 2.12^{+0.19}_{-0.16} \cdot 10^{-21}$ g/g
$^{212}\text{Bi}$	$< 1.73^{+0.13}_{-0.12}$ Bq/kg $< 3.19^{+0.24}_{-0.22} \cdot 10^{-21}$ g/g	$< 0.744^{+0.058}_{-0.050}$ Bq/kg $< 1.37^{+0.11}_{-0.09} \cdot 10^{-21}$ g/g
<b>Th-232 chain</b>	$< 0.547^{+0.027}_{-0.024}$ Bq/kg $< 1.35^{+0.07}_{-0.06} \cdot 10^{-7}$ g/g	$< 0.155^{+0.009}_{-0.007}$ Bq/kg $< 3.82^{+0.22}_{-0.17} \cdot 10^{-8}$ g/g
$^{234}\text{Pa}$	$< 7.87^{+0.74}_{-0.64}$ Bq/kg $< 31.0^{+2.9}_{-2.5} \cdot 10^{-23}$ g/g	$< 4.19^{+0.39}_{-0.34}$ Bq/kg $< 16.5^{+1.5}_{-1.3} \cdot 10^{-23}$ g/g
$^{226}\text{Ra}$	$< 1.75^{+0.17}_{-0.15}$ Bq/kg $< 47.8^{+4.6}_{-4.1} \cdot 10^{-15}$ g/g	$< 0.613^{+0.058}_{-0.051}$ Bq/kg $< 16.7^{+1.6}_{-1.4} \cdot 10^{-15}$ g/g
$^{214}\text{Pb}$	$< 0.443^{+0.031}_{-0.027}$ Bq/kg $< 365^{+26}_{-22} \cdot 10^{-24}$ g/g	$< 0.175^{+0.012}_{-0.011}$ Bq/kg $< 144^{+10}_{-9} \cdot 10^{-24}$ g/g
$^{214}\text{Bi}$	$< 0.630^{+0.047}_{-0.041}$ Bq/kg $< 3.86^{+0.29}_{-0.25} \cdot 10^{-22}$ g/g	$< 0.414^{+0.028}_{-0.025}$ Bq/kg $< 2.53^{+0.17}_{-0.15} \cdot 10^{-22}$ g/g
<b>U-238 chain</b>	$< 0.536^{+0.026}_{-0.022}$ Bq/kg $< 4.30^{+0.21}_{-0.18} \cdot 10^{-8}$ g/g	$< 0.231^{+0.011}_{-0.010}$ Bq/kg $< 1.86^{+0.09}_{-0.08} \cdot 10^{-8}$ g/g

Table 5.9: Limits on the activities (given in Bq/kg as well as in g/g) of the used plastic containers for the different isotopes from the  $^{232}\text{Th}$ - and the  $^{238}\text{U}$ -decay chain, as well as for  $^{40}\text{K}$ . All values are calculated with the method described in the main text. In the case, that several gamma lines were used for the calculation of the activity of one isotope, the quoted value is the weighted average of the single activities. The limits given for the whole decay chains are again the weighted averages of the activities of the single isotopes.

RESULTS FOR THE PLASTIC CONTAINERS (90% C.L.)		
<i>isotope</i>	<i>PEHD</i>	<i>PTFE</i>
$^{235}\text{U}$	$< 0.135_{-0.011}^{+0.012}$ Bq/kg $< 1.69_{-0.14}^{+0.15} \cdot 10^{-9}$ g/g	$< 79.6_{-6.3}^{+7.3} \cdot 10^{-3}$ Bq/kg $< 9.94_{-0.79}^{+0.91} \cdot 10^{-10}$ g/g
$^{231}\text{Pa}$	$< 0.554_{-0.080}^{+0.086}$ Bq/kg $< 3.17_{-0.46}^{+0.49} \cdot 10^{-13}$ g/g	$< 0.339_{-0.049}^{+0.052}$ Bq/kg $< 1.94_{-0.28}^{+0.30} \cdot 10^{-13}$ g/g
$^{227}\text{Th}$	$< 0.522_{-0.099}^{+0.104}$ Bq/kg $< 4.59_{-0.87}^{+0.91} \cdot 10^{-19}$ g/g	$< 0.289_{-0.055}^{+0.058}$ Bq/kg $< 2.54_{-0.48}^{+0.51} \cdot 10^{-19}$ g/g
$^{223}\text{Ra}$	$< 60.5_{-6.4}^{+7.0} \cdot 10^{-3}$ Bq/kg $< 31.9_{-3.4}^{+3.7} \cdot 10^{-21}$ g/g	$< 41.3_{-4.3}^{+4.8} \cdot 10^{-3}$ Bq/kg $< 21.8_{-2.3}^{+2.5} \cdot 10^{-21}$ g/g
$^{219}\text{Rn}$	$< 88.1_{-10.2}^{+11.0} \cdot 10^{-3}$ Bq/kg $< 1.83_{-0.21}^{+0.23} \cdot 10^{-25}$ g/g	$< 61.2_{-6.9}^{+7.4} \cdot 10^{-3}$ Bq/kg $< 1.27_{-0.14}^{+0.15} \cdot 10^{-25}$ g/g
$^{211}\text{Pb}$	$< 0.321_{-0.030}^{+0.033}$ Bq/kg $< 0.351_{-0.033}^{+0.036} \cdot 10^{-21}$ g/g	$< 0.153_{-0.014}^{+0.016}$ Bq/kg $< 0.167_{-0.015}^{+0.018} \cdot 10^{-21}$ g/g
<b>U-235 chain</b>	$< 90.2_{-4.8}^{+5.2} \cdot 10^{-3}$ Bq/kg $< 1.13_{-0.06}^{+0.06} \cdot 10^{-9}$ g/g	$< 61.4_{-3.1}^{+3.4} \cdot 10^{-3}$ Bq/kg $< 7.67_{-0.39}^{+0.42} \cdot 10^{-10}$ g/g

Table 5.10: Limits on the activities (given in Bq/kg as well as in g/g) of the used plastic containers for the different isotopes from the  $^{235}\text{U}$ -decay chain. All values are calculated with the method described in the main text. In the case, that several gamma lines were used for the calculation of the activity of one isotope, the quoted value is the weighted average of the single activities. The limits given for the whole decay chains are again the weighted averages of the activities of the single isotopes.

RESULTS FOR THE ORGANIC LIQUIDS (90% C.L.)		
<i>isotope</i>	<i>LAB</i>	<i>Tetradecane</i>
<b>K-40</b>	$< 0.158^{+0.015}_{-0.013}$ Bq/kg $< 6.10^{+0.58}_{-0.50} \cdot 10^{-10}$ g/g	$< 0.142^{+0.013}_{-0.012}$ Bq/kg $< 5.48^{+0.50}_{-0.46} \cdot 10^{-10}$ g/g
$^{228}\text{Ac}$	$< 44.5^{+3.2}_{-2.9} \cdot 10^{-3}$ Bq/kg $< 0.538^{+0.039}_{-0.035} \cdot 10^{-21}$ g/g	$< 87.8^{+5.5}_{-4.9} \cdot 10^{-3}$ Bq/kg $< 1.06^{+0.07}_{-0.06} \cdot 10^{-21}$ g/g
$^{212}\text{Pb}$	$< 8.84^{+0.79}_{-0.68} \cdot 10^{-3}$ Bq/kg $< 0.172^{+0.015}_{-0.013} \cdot 10^{-21}$ g/g	$< 16.5^{+1.5}_{-1.3} \cdot 10^{-3}$ Bq/kg $< 0.321^{+0.029}_{-0.025} \cdot 10^{-21}$ g/g
$^{212}\text{Bi}$	$< 0.233^{+0.018}_{-0.015}$ Bq/kg $< 0.430^{+0.033}_{-0.028} \cdot 10^{-21}$ g/g	$< 0.183^{+0.014}_{-0.012}$ Bq/kg $< 0.338^{+0.026}_{-0.022} \cdot 10^{-21}$ g/g
<b>Th-232 chain</b>	$< 11.2^{+0.8}_{-0.7} \cdot 10^{-3}$ Bq/kg $< 2.76^{+0.20}_{-0.17} \cdot 10^{-9}$ g/g	$< 23.0^{+1.4}_{-1.2} \cdot 10^{-3}$ Bq/kg $< 5.66^{+0.34}_{-0.30} \cdot 10^{-9}$ g/g
$^{234}\text{Pa}$	$< 0.567^{+0.053}_{-0.046}$ Bq/kg $< 2.23^{+0.21}_{-0.18} \cdot 10^{-23}$ g/g	$< 0.869^{+0.080}_{-0.071}$ Bq/kg $< 3.42^{+0.31}_{-0.28} \cdot 10^{-23}$ g/g
$^{226}\text{Ra}$	$< 0.101^{+0.010}_{-0.008}$ Bq/kg $< 2.76^{+0.27}_{-0.22} \cdot 10^{-15}$ g/g	$< 0.170^{+0.016}_{-0.014}$ Bq/kg $< 4.64^{+0.44}_{-0.38} \cdot 10^{-15}$ g/g
$^{214}\text{Pb}$	$< 49.8^{+3.4}_{-3.0} \cdot 10^{-3}$ Bq/kg $< 41.0^{+2.8}_{-2.5} \cdot 10^{-24}$ g/g	$< 37.3^{+2.8}_{-2.4} \cdot 10^{-3}$ Bq/kg $< 30.7^{+2.3}_{-2.0} \cdot 10^{-24}$ g/g
$^{214}\text{Bi}$	$< 0.139^{+0.007}_{-0.007}$ Bq/kg $< 85.1^{+4.3}_{-4.1} \cdot 10^{-24}$ g/g	$< 0.131^{+0.007}_{-0.006}$ Bq/kg $< 80.2^{+4.3}_{-3.7} \cdot 10^{-24}$ g/g
<b>U-238 chain</b>	$< 70.1^{+2.9}_{-2.6} \cdot 10^{-3}$ Bq/kg $< 5.63^{+0.23}_{-0.21} \cdot 10^{-9}$ g/g	$< 54.1^{+2.6}_{-2.2} \cdot 10^{-3}$ Bq/kg $< 4.34^{+0.21}_{-0.18} \cdot 10^{-9}$ g/g

Table 5.11: Limits on the activities (given in Bq/kg as well as in g/g) of the investigated organic liquids for the different isotopes from the  $^{232}\text{Th}$ - and the  $^{238}\text{U}$ -decay chain, as well as for  $^{40}\text{K}$ . All values are calculated with the method described in the main text. In the case, that several gamma lines were used for the calculation of the activity of one isotope, the quoted value is the weighted average of the single activities. The limits given for the whole decay chains are again the weighted averages of the activities of the single isotopes.

RESULTS FOR THE ORGANIC LIQUIDS (90% C.L.)		
<i>isotope</i>	<i>LAB</i>	<i>Tetradecane</i>
$^{235}\text{U}$	$< 89.3_{-7.1}^{+8.1} \cdot 10^{-3} \text{ Bq/kg}$ $< 1.12_{-0.09}^{+0.10} \cdot 10^{-9} \text{ g/g}$	$< 0.543_{-0.043}^{+0.049} \text{ Bq/kg}$ $< 6.78_{-0.54}^{+0.61} \cdot 10^{-9} \text{ g/g}$
$^{231}\text{Pa}$	$< 0.539_{-0.077}^{+0.083} \text{ Bq/kg}$ $< 3.08_{-0.44}^{+0.47} \cdot 10^{-13} \text{ g/g}$	$< 2.26_{-0.32}^{+0.35} \text{ Bq/kg}$ $< 12.9_{-1.8}^{+2.0} \cdot 10^{-13} \text{ g/g}$
$^{227}\text{Th}$	$< 0.404_{-0.075}^{+0.078} \text{ Bq/kg}$ $< 3.55_{-0.66}^{+0.69} \cdot 10^{-19} \text{ g/g}$	$< 2.37_{-0.44}^{+0.46} \text{ Bq/kg}$ $< 20.8_{-3.9}^{+4.0} \cdot 10^{-19} \text{ g/g}$
$^{223}\text{Ra}$	$< 22.8_{-2.4}^{+2.6} \cdot 10^{-3} \text{ Bq/kg}$ $< 12.0_{-1.3}^{+1.4} \cdot 10^{-21} \text{ g/g}$	$< 0.249_{-0.026}^{+0.029} \text{ Bq/kg}$ $< 131_{-14}^{+15} \cdot 10^{-21} \text{ g/g}$
$^{219}\text{Rn}$	$< 44.0_{-5.0}^{+5.3} \cdot 10^{-3} \text{ Bq/kg}$ $< 9.14_{-1.04}^{+1.10} \cdot 10^{-26} \text{ g/g}$	$< 0.339_{-0.038}^{+0.041} \text{ Bq/kg}$ $< 7.04_{-0.79}^{+0.85} \cdot 10^{-25} \text{ g/g}$
$^{211}\text{Pb}$	$< 0.164_{-0.015}^{+0.017} \text{ Bq/kg}$ $< 0.180_{-0.016}^{+0.019} \cdot 10^{-21} \text{ g/g}$	$< 0.457_{-0.047}^{+0.053} \text{ Bq/kg}$ $< 0.500_{-0.051}^{+0.058} \cdot 10^{-21} \text{ g/g}$
<b>U-235 chain</b>	$< 34.9_{-2.0}^{+2.2} \cdot 10^{-3} \text{ Bq/kg}$ $< 4.36_{-0.25}^{+0.27} \cdot 10^{-10} \text{ g/g}$	$< 0.357_{-0.018}^{+0.020} \text{ Bq/kg}$ $< 4.46_{-0.22}^{+0.25} \cdot 10^{-9} \text{ g/g}$

Table 5.12: Limits on the activities (given in Bq/kg as well as in g/g) of the investigated organic liquids (the scintillator LAB and the mineral oil tetradecane) for the different isotopes from the  $^{235}\text{U}$ -decay chain. All values are calculated with the method described in the main text. In the case, that several gamma lines were used for the calculation of the activity of one isotope, the quoted value is the weighted average of the single activities. The limits given for the whole decay chains are again the weighted averages of the activities of the single isotopes.

RESULTS FOR THE WAVELENGTH SHIFTERS (90% C.L.)		
<i>isotope</i>	<i>PPO</i>	<i>bisMSB</i>
<b>K-40</b>	$< 0.546^{+0.051}_{-0.045}$ Bq/kg $< 2.11^{+0.20}_{-0.17} \cdot 10^{-9}$ g/g	$< 0.912^{+0.085}_{-0.075}$ Bq/kg $< 3.52^{+0.33}_{-0.29} \cdot 10^{-9}$ g/g
$^{228}\text{Ac}$	$< 105^{+9}_{-8} \cdot 10^{-3}$ Bq/kg $< 1.27^{+0.11}_{-0.10} \cdot 10^{-21}$ g/g	$< 150^{+10}_{-9} \cdot 10^{-3}$ Bq/kg $< 1.81^{+0.12}_{-0.11} \cdot 10^{-21}$ g/g
$^{212}\text{Pb}$	$< 26.9^{+2.4}_{-2.1} \cdot 10^{-3}$ Bq/kg $< 0.523^{+0.047}_{-0.041} \cdot 10^{-21}$ g/g	$< 25.0^{+2.2}_{-1.9} \cdot 10^{-3}$ Bq/kg $< 0.486^{+0.043}_{-0.037} \cdot 10^{-21}$ g/g
$^{212}\text{Bi}$	$< 0.647^{+0.045}_{-0.039}$ Bq/kg $< 1.19^{+0.08}_{-0.07} \cdot 10^{-21}$ g/g	$< 1.03^{+0.08}_{-0.07}$ Bq/kg $< 1.90^{+0.15}_{-0.13} \cdot 10^{-21}$ g/g
<b>Th-232 chain</b>	$< 33.7^{+2.3}_{-2.0} \cdot 10^{-3}$ Bq/kg $< 8.30^{+0.57}_{-0.49} \cdot 10^{-9}$ g/g	$< 31.3^{+2.1}_{-1.9} \cdot 10^{-3}$ Bq/kg $< 7.71^{+0.52}_{-0.47} \cdot 10^{-9}$ g/g
$^{234}\text{Pa}$	$< 1.53^{+0.14}_{-0.12}$ Bq/kg $< 6.02^{+0.55}_{-0.47} \cdot 10^{-23}$ g/g	$< 2.91^{+0.27}_{-0.24}$ Bq/kg $< 11.4^{+1.1}_{-0.9} \cdot 10^{-23}$ g/g
$^{226}\text{Ra}$	$< 0.341^{+0.032}_{-0.029}$ Bq/kg $< 9.31^{+0.87}_{-0.79} \cdot 10^{-15}$ g/g	$< 0.450^{+0.043}_{-0.038}$ Bq/kg $< 12.3^{+1.2}_{-1.0} \cdot 10^{-15}$ g/g
$^{214}\text{Pb}$	$< 52.5^{+3.6}_{-3.2} \cdot 10^{-3}$ Bq/kg $< 43.3^{+3.0}_{-2.6} \cdot 10^{-24}$ g/g	$< 87.9^{+6.5}_{-5.7} \cdot 10^{-3}$ Bq/kg $< 72.4^{+5.4}_{-4.7} \cdot 10^{-24}$ g/g
$^{214}\text{Bi}$	$< 0.205^{+0.013}_{-0.012}$ Bq/kg $< 1.25^{+0.08}_{-0.07} \cdot 10^{-22}$ g/g	$< 0.458^{+0.026}_{-0.023}$ Bq/kg $< 2.80^{+0.16}_{-0.14} \cdot 10^{-22}$ g/g
<b>U-238 chain</b>	$< 67.1^{+3.4}_{-3.1} \cdot 10^{-3}$ Bq/kg $< 5.39^{+0.27}_{-0.25} \cdot 10^{-9}$ g/g	$< 0.118^{+0.006}_{-0.005}$ Bq/kg $< 9.48^{+0.48}_{-0.40} \cdot 10^{-9}$ g/g

Table 5.13: Limits on the activities (given in Bq/kg as well as in g/g) of the investigated wavelength shifters for the different isotopes from the  $^{232}\text{Th}$ - and the  $^{238}\text{U}$ -decay chain, as well as for  $^{40}\text{K}$ . All values are calculated with the method described in the main text. In the case, that several gamma lines were used for the calculation of the activity of one isotope, the quoted value is the weighted average of the single activities. The limits given for the whole decay chains are again the weighted averages of the activities of the single isotopes.

RESULTS FOR THE WAVELENGTH SHIFTERS (90% C.L.)		
<i>isotope</i>	<i>PPO</i>	<i>bisMSB</i>
$^{235}\text{U}$	$< 0.198_{-0.016}^{+0.018}$ Bq/kg $< 2.47_{-0.20}^{+0.22} \cdot 10^{-9}$ g/g	$< 0.690_{-0.055}^{+0.063}$ Bq/kg $< 8.62_{-0.69}^{+0.79} \cdot 10^{-9}$ g/g
$^{231}\text{Pa}$	$< 0.831_{-0.119}^{+0.128}$ Bq/kg $< 4.75_{-0.68}^{+0.73} \cdot 10^{-13}$ g/g	$< 1.77_{-0.25}^{+0.27}$ Bq/kg $< 10.1_{-1.4}^{+1.5} \cdot 10^{-13}$ g/g
$^{227}\text{Th}$	$< 0.676_{-0.126}^{+0.132}$ Bq/kg $< 5.94_{-1.11}^{+1.16} \cdot 10^{-19}$ g/g	$< 1.29_{-0.26}^{+0.27}$ Bq/kg $< 11.3_{-2.3}^{+2.4} \cdot 10^{-19}$ g/g
$^{223}\text{Ra}$	$< 81.2_{-8.5}^{+9.4} \cdot 10^{-3}$ Bq/kg $< 42.8_{-4.5}^{+5.0} \cdot 10^{-21}$ g/g	$< 0.132_{-0.014}^{+0.015}$ Bq/kg $< 69.6_{-7.4}^{+7.9} \cdot 10^{-21}$ g/g
$^{219}\text{Rn}$	$< 0.114_{-0.014}^{+0.015}$ Bq/kg $< 2.37_{-0.29}^{+0.31} \cdot 10^{-25}$ g/g	$< 0.186_{-0.021}^{+0.023}$ Bq/kg $< 3.86_{-0.44}^{+0.48} \cdot 10^{-25}$ g/g
$^{211}\text{Pb}$	$< 0.341_{-0.032}^{+0.035}$ Bq/kg $< 0.373_{-0.035}^{+0.038} \cdot 10^{-21}$ g/g	$< 0.363_{-0.034}^{+0.037}$ Bq/kg $< 0.397_{-0.037}^{+0.040} \cdot 10^{-21}$ g/g
<b>U-235 chain</b>	$< \mathbf{0.122}_{-0.006}^{+0.007}$ Bq/kg $< \mathbf{1.52}_{-0.07}^{+0.09} \cdot 10^{-9}$ g/g	$< \mathbf{0.195}_{-0.011}^{+0.012}$ Bq/kg $< \mathbf{2.44}_{-0.14}^{+0.15} \cdot 10^{-9}$ g/g

Table 5.14: Limits on the activities (given in Bq/kg as well as in g/g) of the investigated wavelength shifters (fluors) for the different isotopes from the  $^{235}\text{U}$ -decay chain. All values are calculated with the method described in the main text. In the case, that several gamma lines were used for the calculation of the activity of one isotope, the quoted value is the weighted average of the single activities. The limits given for the whole decay chains are again the weighted averages of the activities of the single isotopes.

The results obtained for the investigated samples for the decay chains of  $^{232}\text{Th}$ ,  $^{238}\text{U}$  and  $^{235}\text{U}$ , as well as  $^{40}\text{K}$ , are summarized in tab. 5.15.

UPPER LIMITS ON THE MASS CONCENTRATION IN $10^{-9}$ G/G				
	<i>LAB</i>	<i>Tetradecane</i>	<i>PPO</i>	<i>bisMSB</i>
$^{40}\text{K}$	0.610	0.548	2.11	3.52
$^{232}\text{Th}$	2.76	5.66	8.30	7.71
$^{238}\text{U}$	5.63	4.34	5.39	9.48
$^{235}\text{U}$	0.436	4.46	1.52	2.44

Table 5.15: *Summary of the final results of the low-background gamma spectroscopy for the investigated samples LAB, tetradecane, PPO and bisMSB. All values for the mass concentrations are given in units of  $10^{-9}$  gramme per gramme. Error bars are given in tables 5.11 through 5.14.*

As the different materials listed above are produced in chemical processes, and as all isotopes of a certain element have the same chemical properties, the isotopes should be present with their natural abundances in the samples investigated. Therefore, the limits on the mass concentrations of two isotopes  $^{238}\text{U}$  and  $^{235}\text{U}$  should, in principle, be combined to a single activity for the element uranium. This combined activity can be calculated by weighting the single activities with the natural abundances of the respective isotopes. However, the natural abundance of  $^{238}\text{U}$  is 99.27% [Fir96]. For this reason the combined activity for uranium is completely dominated by the limits obtained for  $^{238}\text{U}$ . Hence, the limit for the activity of uranium is (nearly) equal to the limit for the activity of  $^{238}\text{U}$ . Even minor deviations from the natural abundances, however, would not affect this result.

## 5.3 Discussion of the results

### 5.3.1 General discussion of the results

Some points of the final results presented in tables 5.9 through 5.14 should be emphasized:

First of all, for all investigated samples (LAB, tetradecane, PPO and bisMSB, as well as the plastic containers) only upper limits on the activities and mass concentrations of certain isotopes were obtained, which means that none of the quoted isotopes are contained in large amounts in the samples. Besides the gamma lines already observed in the blank runs, no further peaks were recognized in the recorded spectra, giving strong limits for the mass

concentrations of any radionuclide. These limits depend on the half-life of the particular radioisotope and are in general of the order of the limit obtained for  $^{235}\text{U}$  or even better, as from the isotopes from this decay chain no gamma peaks were recognized.

The fact, that only upper bounds for the activities were obtained, makes it impossible to decide, whether radioactive equilibrium is existent in the decay chains or not. In principle, this equilibrium could be broken at a particular isotope with a long half-life (e.g.  $^{234}\text{U}$  in the decay chain of  $^{238}\text{U}$ ). However, for the presented results radioactive equilibrium was assumed.

In general, the upper bounds on the activities per mass unit for different isotopes in the same sample vary in the range of one order of magnitude. This is due to the branching ratio  $P$  of the respective gamma line(s). For a particular line, high branchings lead to better upper limits, as can be seen from eq. (5.4). For lines, which cannot be seen in the spectra recorded with sample as well as in the blank run, the limit on the activity is inversely proportional to the branching  $P$ : in this case, the limit obtained for the number of counts  $N_s$  coming from the sample is nearly constant over the whole energy range, as the continuous background is very flat. For lines, which appear in both spectra, but are comparable in intensity, the limit on the activity is inversely proportional to  $\sqrt{P}$ . Here the upper limit for the number of counts  $N_s$  originating from the sample depends on the statistical errors of the number of counts  $N$  within the corresponding gamma peaks (see equations (5.1) through (5.3)), which are  $\sqrt{N}$ . As  $N$  is proportional to  $P$ , one gets for the activity  $A \propto \sqrt{P}/P = 1/\sqrt{P}$ .

The respective mass concentrations vary over a wide range. The reason for this is the wide range of different half-lives (see appendix E), which are specifying the mass concentrations (eq. (4.2)).

Comparing the results obtained for a particular isotope for the different samples shows mainly the influence of the sample mass: the bigger this mass, the better the upper limit on the activity. However, there are two deviations from this observation: in the spectrum recorded without any artificial source (i.e. blank run) as well as in the spectrum of the tetradecane sample the continuous background was increased (see below). The limits for the mass concentrations of radionuclides from the  $^{235}\text{U}$ -decay chain are computed from the continuous background, as no gamma lines are visible from this chain. Therefore, the upper bounds calculated for the plastic containers for these radionuclides are rather stringent, as in this case the low continuous background in the spectra recorded with the containers is compared to the high one in the blank run. For tetradecane, the situation is inverted: the high continuous background in the tetradecane spectrum is compared to the low one observed with the plastic containers, resulting in worse limits for the

same decay chain for tetradecane. However, for tetradecane also no gamma peaks originating from the  $^{235}\text{U}$ -decay chain were observed, so upper limits on the respective activities are given also in this case.

The increased continuous background might have several reasons. As was discussed in section 5.1, the three main contributions here are the bremsstrahlung emitted by fast electrons released by cosmic muons, the Compton-scattering events and the bremsstrahlung of electrons emitted in beta decays. Normally, the first two of these contributions are suppressed by the active veto systems; in case of a malfunction of the veto-electronics this could lead to an increased continuous background. However, the electronics and the veto systems were checked after the measurement and everything was found to be alright. For the measurement performed with tetradecane, the increased background could also be due to an elevated beta activity of the sample. Another possible reason could be an air-leak in the PVC-box or the dewar for the liquid nitrogen supply, leading to a relatively high amount of radon, and thus a high ambient activity in the detector system. Nevertheless, an elevated radon concentration should also increase the number of counts in the gamma peaks of the daughter nuclides of radon, as well as an increased beta activity should show up in some subsequent gamma lines. Both effects however were not observed (see tables 5.6-5.8). Clarifying this point is one of the remaining tasks for future measurements.

Another interesting observation is the correlation between the number of counts in the photopeak of  $^{40}\text{K}$  at 1460.8 keV and the density of the sample: the higher the density of the sample, the smaller the count rate (see tab. 5.7). This might be accidental, but could also be an indication for absorption or scattering of these gamma rays in the sample. This could happen, if the gamma rays originate from a source residing on the side of the sample, which is opposite to the germanium detector. Therefore, possible  $^{40}\text{K}$ -sources are the sodium-iodide crystal of the endcap and the PMTs of the anti-Compton veto. Again, this point should be further investigated in future experiments and/or by a Monte-Carlo simulation.

### 5.3.2 Consequences for the DOUBLE CHOOZ experiment

As already explained in section 1.2.3, the limiting factor for the achievable sensitivity for all reactor neutrino experiments (including DOUBLE CHOOZ) are the statistical and systematical uncertainties. A main contribution to the systematical uncertainties comes from the intrinsic background of the detector. Therefore it has to be kept as low as possible. In the case of

DOUBLE CHOOZ the accidental background rate has to be less than 1% of the neutrino signal [Ard06], which is translating into the following limits (see table 5.16) for the concentrations of radioactive elements in the different detector liquids [Ard04, Ard06]:

<i>Allowed upper limits for the mass concentrations</i>	$^{40}\text{K}$ [g/g]	$U$ [g/g]	$Th$ [g/g]
<i>neutrino target</i>	$\sim 5 \cdot 10^{-13}$	$\sim 10^{-13}$	$\sim 10^{-13}$
<i>gamma catcher</i>	$\sim 5 \cdot 10^{-13}$	$\sim 10^{-13}$	$\sim 10^{-13}$
<i>buffer</i>	-	$\sim 10^{-12}$	$\sim 10^{-12}$
<i>inner veto</i>	-	$\sim 10^{-10}$	$\sim 10^{-10}$

Table 5.16: *Allowed mass concentrations for the radioactive isotopes for the different detector liquids in DOUBLE CHOOZ [Ard04, Ard06]. The values are calculated in such a way, that the rate of beta and gamma decays in the neutrino target and gamma catcher is about 1 Hz. The column for uranium contains the combined activity of the  $^{238}\text{U}$ - and the  $^{235}\text{U}$ -decay chains, both weighted with the natural abundance. The limits for uranium and thorium are stricter than those for potassium, because in the subsequent decay chains several beta and gamma emissions with an energy above  $\sim 1\text{ MeV}$  (the positron annihilation threshold) take place [Fir96]. Alpha decays can be neglected, as the visible energy of alpha particles is quenched well below  $1\text{ MeV}$  [Ard04]. The allowed concentrations for the buffer liquid and the inner veto are less stringent<sup>2</sup>.*

The limits quoted in table 5.11 on page 82 for the liquid scintillator LAB ( $6.10 \cdot 10^{-10}\text{ g/g}$  for  $^{40}\text{K}$ ,  $2.76 \cdot 10^{-9}\text{ g/g}$  for  $^{232}\text{Th}$  and  $5.63 \cdot 10^{-9}\text{ g/g}$  for  $^{238}\text{U}$ ) and the mineral oil tetradecane ( $5.48 \cdot 10^{-10}\text{ g/g}$  for  $^{40}\text{K}$ ,  $5.66 \cdot 10^{-9}$  for  $^{232}\text{Th}$  and  $4.34 \cdot 10^{-9}\text{ g/g}$  for  $^{238}\text{U}$ ) are several orders of magnitude larger<sup>3</sup> than the concentrations allowed for the neutrino target, the gamma catcher and

<sup>2</sup>Just for comparison: The Borexino experiment reached a mass concentration of uranium in the scintillator below  $10^{-17}\text{ g/g}$ ! This was achieved by several purification stages (distillation, water extraction and silicagel-chromatography) [Obe07].

<sup>3</sup>In principle, one should consider the combined limit from  $^{238}\text{U}$  and  $^{235}\text{U}$ , as these two isotopes have the same chemical properties. This combined limit is calculated by weighting the single limits with the natural abundances of the isotopes. But as the natural

the buffer liquid in the DOUBLE CHOOZ detectors. Hence, for these parts of the detector no conclusion can be given, whether a purification is needed or not. In general, it is difficult to reach limits below  $\sim 10^{-11}$  g/g with gamma spectroscopy in underground laboratories [Ard06], therefore other counting methods will have to be used for the target scintillator (for example neutron activation analysis). However, the maximum mass concentrations allowed for the inner veto of DOUBLE CHOOZ can in principle be tested in a gamma spectroscopy measurement, as was shown with the limit obtained for the mass concentration of  $^{235}\text{U}$  for LAB ( $4.36 \cdot 10^{-10}$  g/g). LAB will not be used in pure form in the inner veto, but diluted with some mineral oil (e.g. tetradecane), leading to increased allowed concentrations for the radionuclides (for example increased by a factor of 2.5 for a mixture of 40% LAB and 60% mineral oil).

To make a final conclusion on the scintillator for the inner veto, the sensitivity of the measurements has to be further increased. Regarding eq. (5.4) for the calculation of the activity, or the upper limit on the activity, shows three possibilities for an improvement of the obtained results: Increasing the mass  $M_{\text{sample}}$  of the measured sample, increasing the measuring time  $t$ , and/or decreasing the number of background counts  $N$  all lead to a more stringent upper limit for the activity per mass unit, and thereby the mass concentration, of a certain isotope in the investigated sample. The relative gamma intensity  $P$  and the detector efficiency  $\varepsilon_{\text{Det}}$  cannot be changed, however.

Increasing the sample mass is probably the easiest possibility. As it can be seen from tables 5.9 through 5.14 on pages 80-85, the best upper limits are achieved for the organic liquids LAB and tetradecane, simply for the reason, that these two samples had the biggest mass. The sample volume of the detector system used would in principle allow bigger sample masses, but specially shaped containers would have to be manufactured. This could be part of an upgrade for future measurements.

Decreasing the number of counts in a certain peak can only be achieved by reducing the intrinsic background of the detector. The optimal solution would be, that there are no gamma peaks visible in the background spectrum (as it is the case for the gamma lines from the  $^{235}\text{U}$ -decay chain, leading to good constraints for the mass concentrations, see again tables 5.9 through 5.14), combined with a very tiny continuous background. Future studies are planned on this point, for example an improved cleaning of the whole detector system or an additional supply for nitrogen flushing through the PVC-box to expel the radon more efficiently.

---

abundance of  $^{238}\text{U}$  is 99.27%, the combined limit is nearly equal to the limit obtained for the  $^{238}\text{U}$ -decay chain.

Longer measuring times mainly improve the statistics, leading to decreasing uncertainties of the measured values, and thus to stronger upper bounds for the number of counts emitted by the sample itself. Nevertheless, the impact of the measuring time on the achieved sensitivity is again limited by the intrinsic background: in the presence of background, the errors decrease only proportional to the square-root of the measuring time. Hence, measuring times considerably longer than 1,000,000 seconds do not make very much sense.

The situation is quite different for the wavelength-shifters bisMSB and PPO, as these are only used in very small concentrations in the liquid scintillators (intended values in DOUBLE CHOOZ [Ard06]: 6 g/l for PPO and 20 mg/l for bisMSB). Due to this dilution the allowed concentrations for these two materials are much higher, see table 5.17.

Comparing these allowed concentrations with the measured limits given in tab. 5.13 shows, that both wave-length shifters can be used for the inner veto of the DOUBLE CHOOZ detectors without any purification. Furthermore, the mass concentration of  $^{40}\text{K}$  in bisMSB ( $< 3.52 \cdot 10^{-9}$  g/g) is also far below the allowed concentration in the neutrino target and the gamma catcher, while the measured limits for  $^{238}\text{U}$  ( $< 9.48 \cdot 10^{-9}$  g/g) and  $^{232}\text{Th}$  ( $< 7.71 \cdot 10^{-9}$  g/g) are roughly a factor of 2 above the allowed limits. Improving the results by a factor 2 or more can simply be reached in a repeated measurement of bisMSB just by using a bigger amount of material (e.g. 100 grammes instead of 25 grammes). The upper bounds obtained for potassium, uranium and thorium for PPO are, however, two orders of magnitude too large compared with the required ones for the neutrino target and the gamma catcher in DOUBLE CHOOZ. Thus, again no conclusion can be given yet, whether PPO is suitable without any purification for the inner detector volumes or not.

<i>Allowed upper limits for the mass concentrations</i>	$^{40}\text{K}$ [g/g]	$U$ [g/g]	$Th$ [g/g]
PPO			
<i>neutrino target</i>	$\sim 7 \cdot 10^{-11}$	$\sim 10^{-11}$	$\sim 10^{-11}$
<i>gamma catcher</i>	$\sim 7 \cdot 10^{-11}$	$\sim 10^{-11}$	$\sim 10^{-11}$
<i>inner veto</i>	-	$\sim 10^{-8}$	$\sim 10^{-8}$
bisMSB			
<i>neutrino target</i>	$\sim 2 \cdot 10^{-8}$	$\sim 4 \cdot 10^{-9}$	$\sim 4 \cdot 10^{-9}$
<i>gamma catcher</i>	$\sim 2 \cdot 10^{-8}$	$\sim 4 \cdot 10^{-9}$	$\sim 4 \cdot 10^{-9}$
<i>inner veto</i>	-	$\sim 4 \cdot 10^{-6}$	$\sim 4 \cdot 10^{-6}$

Table 5.17: *Allowed mass concentrations for the radioactive isotopes for the wave-length shifters PPO and bisMSB. The values are calculated from the values given in tab. 5.16 assuming a concentration of PPO of 6 g/l and of bisMSB of 20 mg/l in the liquid scintillator. The limits given here are valid in the case, that the liquid scintillators themselves do not contain any radioactive isotopes. Otherwise care has to be taken, that the combined activity of the scintillator and the wave-length shifters dissolved in it does not exceed the limits given in tab. 5.16. This does not apply for the buffer liquid, since it does not contain wave-length shifters at all.*

# Chapter 6

## Conclusion & Outlook

In the last decade neutrino physics has made tremendous progress. Neutrino oscillations are known to be the cause for a huge variety of experimentally observed phenomena, like the lack of electron neutrinos originating from the sun, the dependence of the atmospheric muon-neutrino flux on the zenith angle or the appearance of neutrinos of the "wrong" flavour in accelerator neutrino beams. In the case, that neutrinos are Dirac particles, the theory of neutrino oscillations has six free parameters [Akh00, Akh06, Bil78, Bil99, Sch97], the three mixing angles  $\vartheta_{12}$ ,  $\vartheta_{13}$  and  $\vartheta_{23}$ , which determine the amplitudes of the oscillations, the two mass-squared differences, determining the oscillation frequencies, and one CP-violating phase  $\delta$ . While the two mass-squared differences  $\Delta m_{21}^2 = (8.0 \pm 0.3) \cdot 10^{-5} \text{ eV}^2$  and  $\Delta m_{32}^2 = (1.9 \text{ to } 3.0) \cdot 10^{-3} \text{ eV}^2$ , as well as  $\sin^2(2\vartheta_{12}) = 0.86_{-0.04}^{+0.03}$  and  $\sin^2(2\vartheta_{23}) > 0.92$ , are known to a high precision from various experiments, the last mixing angle  $\vartheta_{13}$  and the phase  $\delta$  are still unknown. For Majorana neutrinos two additional phases appear within the PMNS-matrix, also being unknown at present [Akh00, Doi81, Sch97]. However, several further fundamental properties of the neutrino need to be investigated in forthcoming experiments: the absolute mass scale and the hierarchy of the mass eigenvalues of the neutrinos are unknown, as well as whether neutrinos are Dirac or Majorana particles (the latter would imply, that neutrinos are their own anti-particles). All of these issues are either currently investigated or will be addressed by experiments in the near future.

One of these experiments is the DOUBLE CHOOZ reactor neutrino project in France [And04, Ard04, Ard06, Ber04, Obe06]. DOUBLE CHOOZ uses two identical liquid-scintillator detectors, each with a neutrino target volume of  $10.3 \text{ m}^3$ . The near detector is meant for flux monitoring, while the far detector is sensitive on effects from neutrino oscillations due to  $\vartheta_{13}$  on a baseline of 1050 metres. The intended sensitivity of DOUBLE CHOOZ is  $\sin^2(2\vartheta_{13}) \leq 0.03$  after three years of data taking [Ard06]. In case, DOU-

BLE CHOOZ does not measure a certain value for  $\vartheta_{13}$ , but can give only an improved upper limit on its value, this would be trend-setting for the next generation of neutrino beam experiments, as these will only be able to measure the CP-violating phase  $\delta$ , if  $\sin^2(2\vartheta_{13}) \gtrsim 0.01$  [Ber04].

In order to perform such a high-precision liquid-scintillator experiment, the intrinsic background of the detectors has to be very low. In this respect, an important issue is the concentration of radioactive isotopes within the materials used. Low-background gamma spectroscopy provides the possibility to measure these concentrations directly. Therefore, a detector system has been set up in the underground laboratory of the Technische Universität München in Garching (overburden: 15 m.w.e.), consisting of a germanium detector surrounded by several passive and active shielding systems for background reduction. The germanium detector has a relative counting efficiency of 150.5% and reaches an energy resolution of 1.764 keV at 1.33 MeV. It is enclosed by an anti-Compton veto, consisting of sodium-iodide scintillation crystals, which are read out by photomultipliers. This veto system serves for suppressing the Compton-scattering events in the germanium detector, leading to an improved peak-to-background ratio, especially for low-energetic gamma peaks. Its seven multipliers have been balanced, using their gain potentiometers and separate high voltage supplies. Both detectors are surrounded by a 15 cm thick lead-shielding, partly built from ultra pure lead (activity of  $^{210}\text{Pb}$  less than 5 Bq/kg [Lan07]), and a plastic box, which is flushed during operation with nitrogen to expel the radioactive noble gas radon. Plastic scintillator panels around the plastic box serve as active muon-veto. These panels were also calibrated in terms of having a high detection probability for muons and simultaneously a low dead-time.

Before starting the actual measurements, blank runs have been performed in terms of determining the intrinsic background of the detector system, as well as the radioactivity of the used sample holders. All remaining gamma lines in the background were identified. For the DOUBLE CHOOZ detectors, four different samples were investigated: the liquid scintillator LAB, the mineral oil tetradecane and the wave-length shifters PPO and bisMSB. In the recorded spectra of all samples only gamma lines showed up, which were already observed in the corresponding background spectra. Furthermore, the intensities of the respective gamma lines were compatible within the error bars, leading to strong upper limits on the concentration of radioactive isotopes in the investigated materials, see table 6.1.

These limits on the mass concentrations of the radionuclides obtained for the different samples imply, that both wave-length shifters can be used without any additional purification in the inner veto of the DOUBLE CHOOZ detectors [Ard04, Ard06]. The other limits, which can be given so far, are above

UPPER LIMITS ON THE MASS CONCENTRATION IN $10^{-9}$ G/G				
	<i>LAB</i>	<i>Tetradecane</i>	<i>PPO</i>	<i>bisMSB</i>
$^{40}\text{K}$	0.610	0.548	2.11	3.52
$^{232}\text{Th}$	2.76	5.66	8.30	7.71
$^{238}\text{U}$	5.63	4.34	5.39	9.48
$^{235}\text{U}$	0.436	4.46	1.52	2.44

Table 6.1: *Summary of the final results of the low-background gamma spectroscopy for the investigated samples LAB, tetradecane, PPO and bisMSB. All values for the mass concentrations are given in units of  $10^{-9}$  gramme per gramme. Error bars are given in tables 5.11 through 5.14 in chapter 5.2.2.*

the allowed concentrations for DOUBLE CHOOZ. Before further conclusions can be drawn, improvements concerning the sensitivity of the measurements are necessary. This can be achieved by further reducing the intrinsic background of the detector system and the usage of larger sample masses.

In addition, another mode of measurement is intended in the future: using the anti-Compton veto in coincidence mode provides the opportunity of triggering on a certain gamma line in a gamma cascade appearing after a radioactive decay or triggering on a gamma event within the germanium detector (for example the 511 keV escape line from positron annihilation after a pair production process), thus being able to determine the activity of a given single isotope nearly background-free.

Furthermore, the activity of certain isotopes can enormously be increased by neutron activation analysis, making it possible to reach sensitivities down to  $10^{-17}$  g/g, as was shown by R. v. Hentig in his Ph.D. thesis [Hen99]. The activation with neutrons could be performed at the Forschungsreaktor München FRM II, residing on the campus of the Technische Universität München.

The possibility of using a second germanium detector instead of the end-cap of the anti-Compton veto (see fig. 6.1) is under investigation, too. This would lead not only to a mere doubling of the solid angle covered by the germanium detector(s), and thus a doubling of the detector efficiency, but would also allow to perform coincidence measurements with two germanium detectors and thus would lead to an unrivalled sensitivity of the detector system. Certain gamma lines, being part of the characteristic gamma cascade of selected isotopes, could be measured nearly completely free of any intrinsic background of the detector system.

For the determination of the efficiency of the germanium detector, a

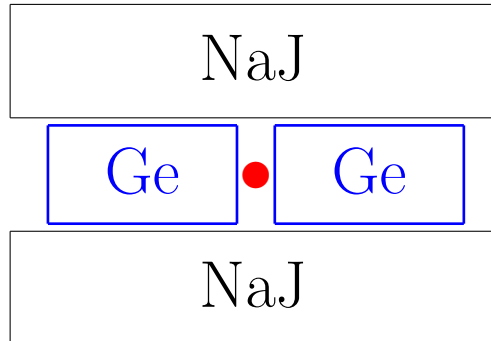


Figure 6.1: *Future detector system consisting of two identical germanium detectors put face-to-face, enclosed by a cylindrically shaped anti-Compton veto. The position of the sample is marked with a red circle.*

Monte-Carlo simulation based on the software kit GEANT4 was written. A comparison of simulated detector efficiencies with those obtained with radioactive calibration sources showed, that the simulation is quite good for gamma energies above  $\sim 200$  keV, but has a systematic deviation for lower gamma energies. For that reason, gamma lines below this threshold were discarded in the calculation of the radioactivities of the investigated samples. These lines will also be analysed after an improvement of the Monte-Carlo simulation. Furthermore, the analysis will be extended to gamma lines from gamma cascades, after the detector efficiency of the combined detector system, consisting of germanium detector and anti-Compton veto, has been determined for this situation, again using the Monte-Carlo simulation technique. Calibration sources emitting coincident gamma rays will be used for a comparison between measurement and simulation.

Besides the improvement of the detector sensitivity and the amelioration of the Monte-Carlo simulation, the most important task for the near future is the measurement of further samples for the DOUBLE CHOOZ detectors. Not only components of the detector liquids (like different mineral oils or wave-length shifters) have to be investigated with respect to their contribution of radioactive isotopes, but also samples from the intended tanks and reinforcing structures, the level monitoring and the filling system and, last but not least, the photomultipliers themselves have to be measured. Keeping the accidental background in all detector parts as low as possible is one of the main challenges of DOUBLE CHOOZ, an experiment meant to determine the last unknown mixing angle  $\vartheta_{13}$  with an up to now unrivalled sensitivity.

Hence, DOUBLE CHOOZ will be trend-setting for the next generation of neutrino experiments.



# Appendix A

## Balancing of the anti-Compton veto

The figures A.1 - A.3 show the  $^{137}\text{Cs}$ -spectra of the different parts (upper and lower half shell, as well as the endcap) of the anti-Compton veto system for different applied high voltages (850 V, 900 V and 950 V). From these spectra the energy resolutions given in table 3.2 in section 3.3.2 were determined.

The balancing procedure for the upper half shell was done with a high voltage of 950 V. This voltage was applied to all three multipliers and the respective  $^{137}\text{Cs}$ -spectra were recorded (with full gain (focus) at the PMT potentiometer). Afterwards the gain of the two multipliers with the highest amplification was reduced stepwise until it matched the gain of the multiplier with the lowest amplification. Table A.1 lists the channels for the 662 keV peak from  $^{137}\text{Cs}$  in the pulse height spectra before and after adjustment of the gain for the three upper photomultipliers.

This procedure was repeated twice: Once without optical compound (tab. A.2) and the second time after recontacting with optical compound (tab. A.3 and fig. A.4).

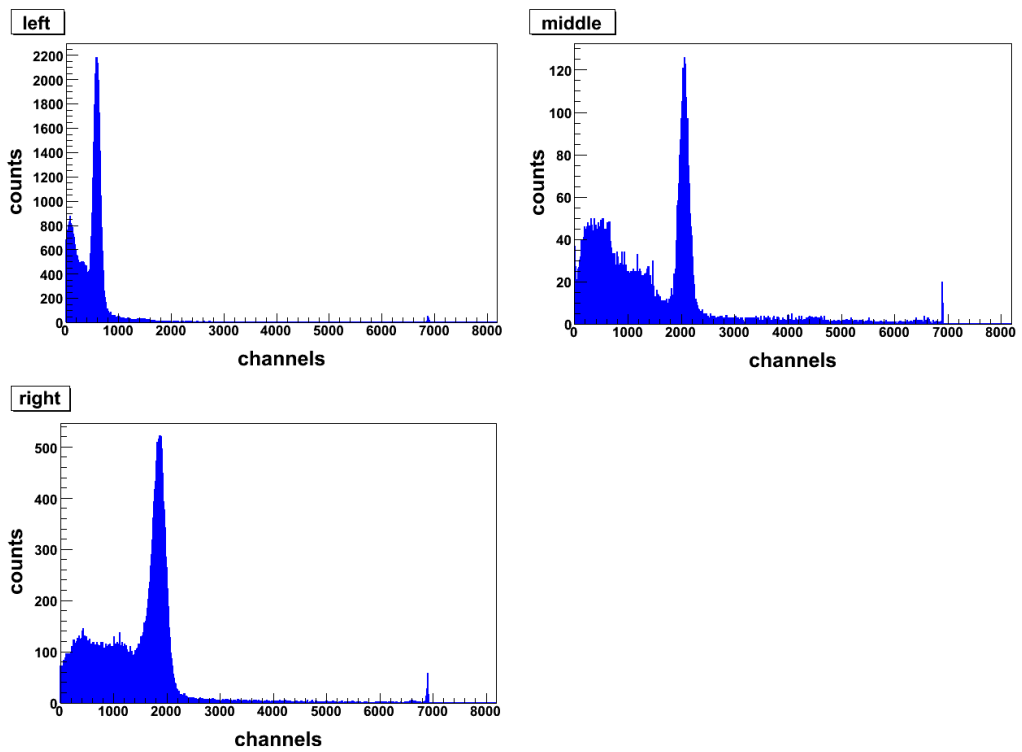


Figure A.1:  $^{137}\text{Cs}$ -spectra of the different parts of the anti-Compton veto with an applied high voltage of 850 V. Measuring time for each spectrum: 100 seconds.

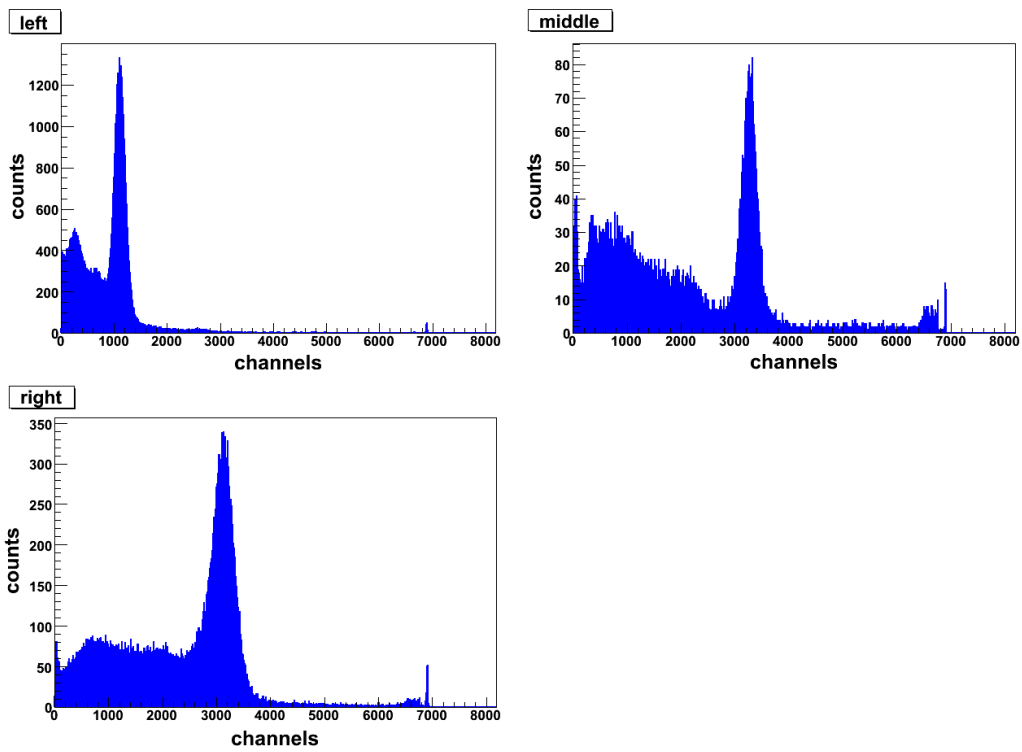


Figure A.2:  $^{137}\text{Cs}$ -spectra of the different parts of the anti-Compton veto with an applied high voltage of 900 V. Measuring time for each spectrum: 100 seconds.

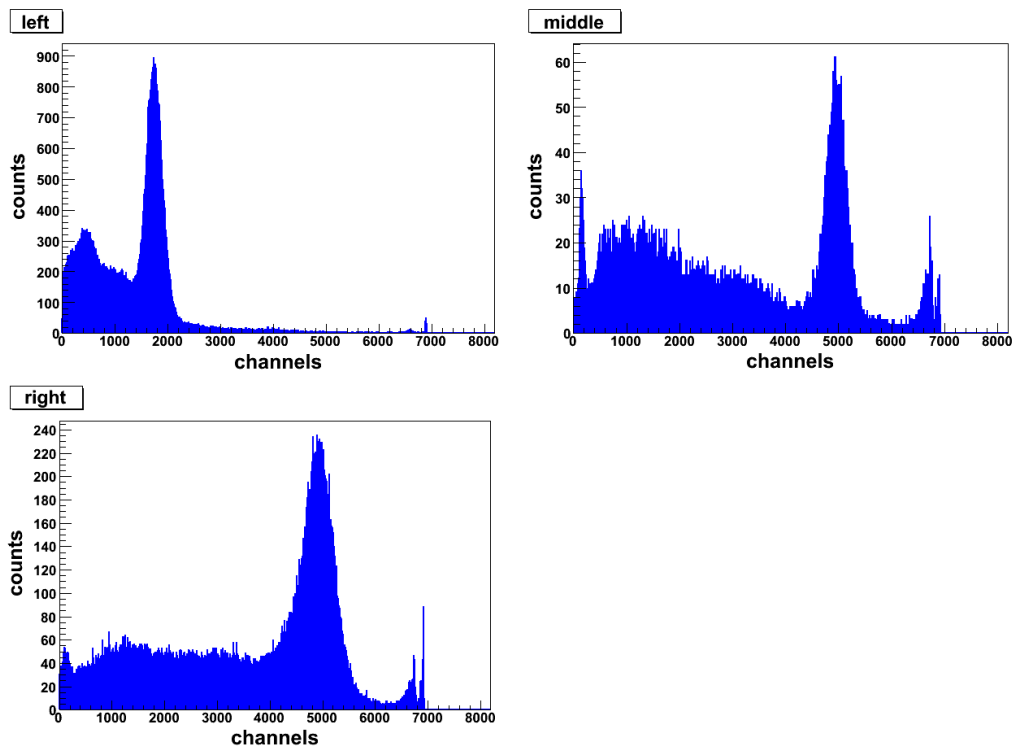


Figure A.3:  $^{137}\text{Cs}$ -spectra of the different parts of the anti-Compton veto with an applied high voltage of 950 V. Measuring time for each spectrum: 100 seconds.

---

<i>Peak position in channels at 662 keV</i>		
<i>PMT</i>	<i>before balancing</i>	<i>after balancing</i>
left	375	293
middle	496	313
right	308	308

Table A.1: Position of the  $^{137}\text{Cs}$  peak for the three multipliers in the upper half shell before and after adjustment of the gain (focus) potentiometer. Voltage feed 950 V.

<i>Peak position in channels at 662 keV</i>		
<i>PMT</i>	<i>before balancing</i>	<i>after balancing</i>
left	243	178
middle	269	157
right	204	204

Table A.2: Position of the  $^{137}\text{Cs}$  peak for the three multipliers in the upper half shell before and after adjustment of the gain (focus) potentiometer without optical compound. Voltage feed 950 V.

<i>Peak position in channels at 662 keV</i>		
<i>PMT</i>	<i>before balancing</i>	<i>after balancing</i>
left	380	338
middle	497	322
right	328	328

Table A.3: Position of the  $^{137}\text{Cs}$  peak for the three multipliers in the upper half shell before and after adjustment of the gain (focus) potentiometer; recontacted with optical compound. Voltage feed 950 V.

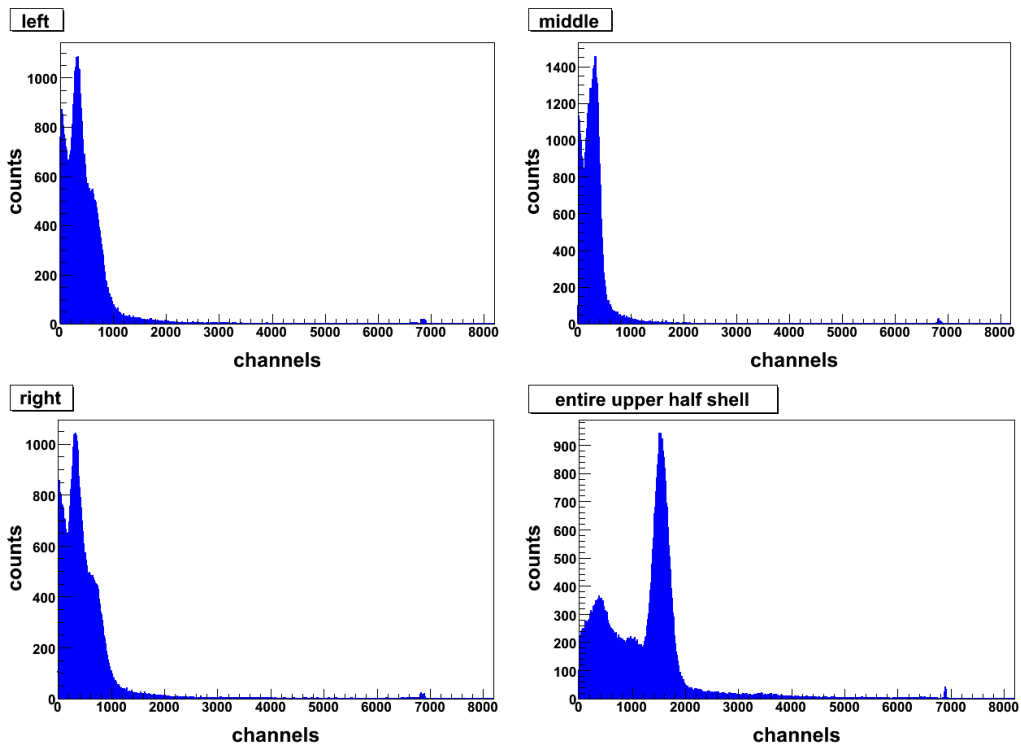


Figure A.4:  $^{137}\text{Cs}$ -spectra of the three upper PMTs after gain (focus) adjustment recontacted with optical compound, as well as the new sum spectrum. Recorded over 100 seconds with a high voltage of 950 V.

# Appendix B

## Calibration of the muon-veto system

To find the most suitable high voltage, first of all different positive high voltages were applied to panel 1 and spectra using the  $^{60}\text{Co}$ -source were recorded (fig. B.1).

1400 volts seemed to be most suitable (compromise between amplification and dark noise). Hence 1400 V were applied to all 6 panels and again  $^{60}\text{Co}$ -spectra were recorded (fig. B.2).

After that, the high voltages were adjusted in such a way, that the amplification of all 6 panels is roughly the same and the focus was optimised (as described in section 3.4.2). The results are shown in fig. B.3.

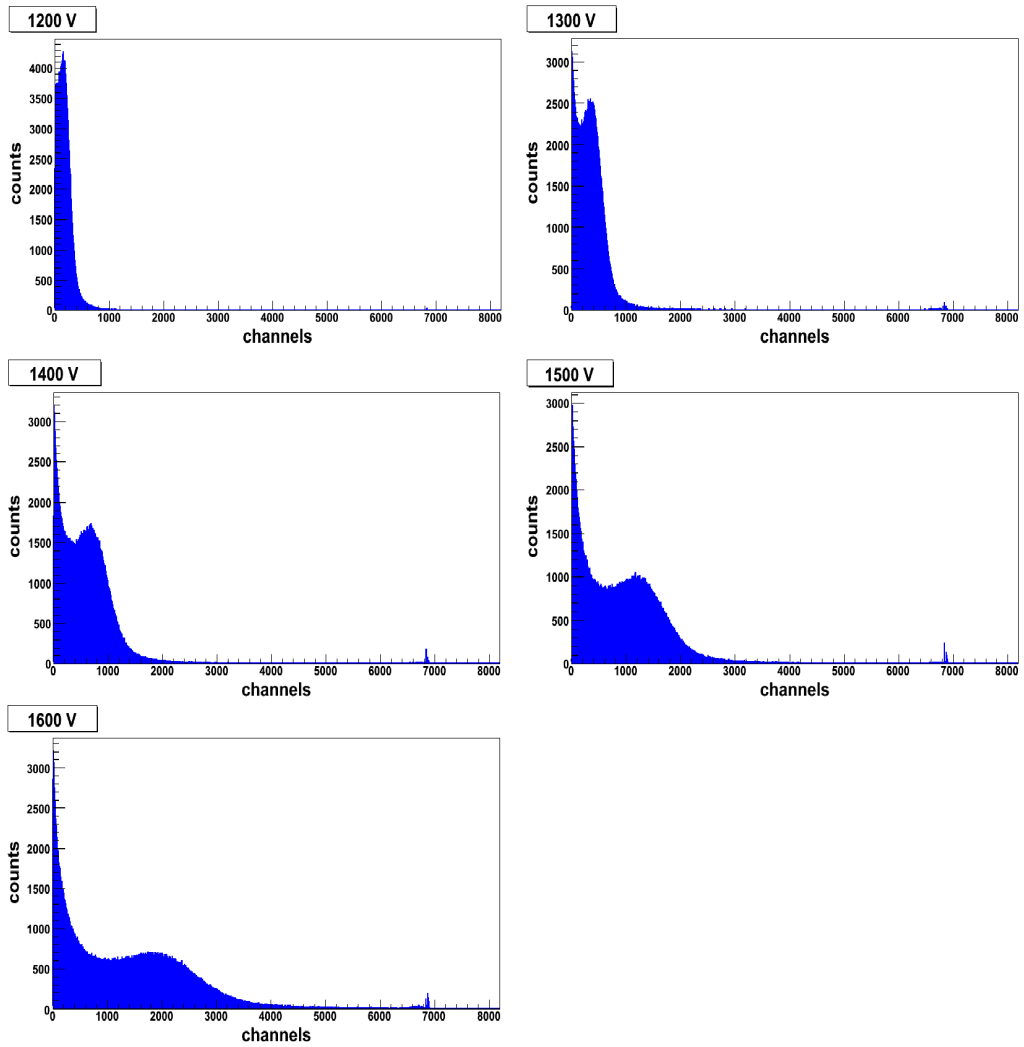


Figure B.1:  $^{60}\text{Co}$  spectra of panel 1 for different high voltages recorded over 100 seconds measuring time.

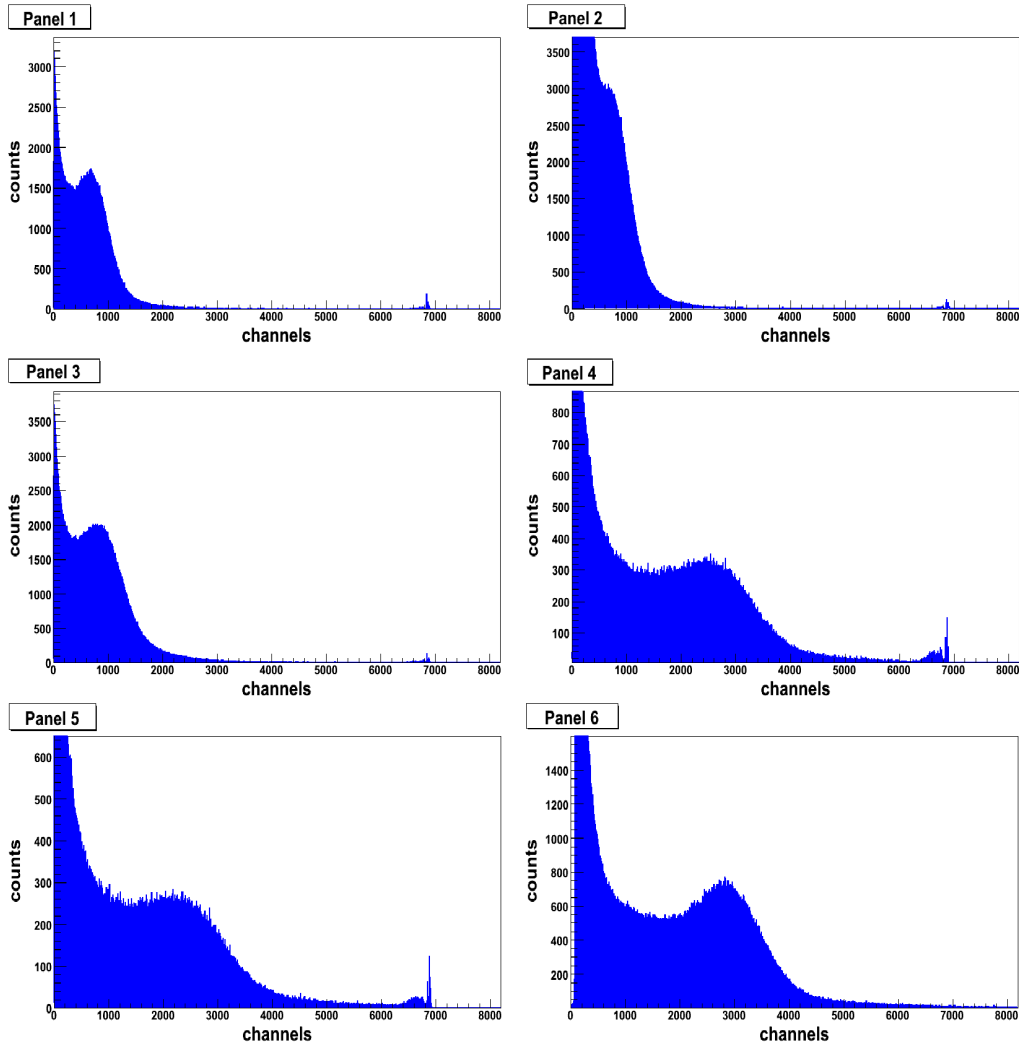


Figure B.2: The  $^{60}\text{Co}$  spectra of the 6 different panels all recorded for a HV of 1400 V over 100 seconds. The peak, that can be seen is the Compton edge of the two gamma lines of  $^{60}\text{Co}$  at roughly 1 MeV. Due to the relatively bad energy resolution of the plastic scintillator the two Compton edges can not be resolved.

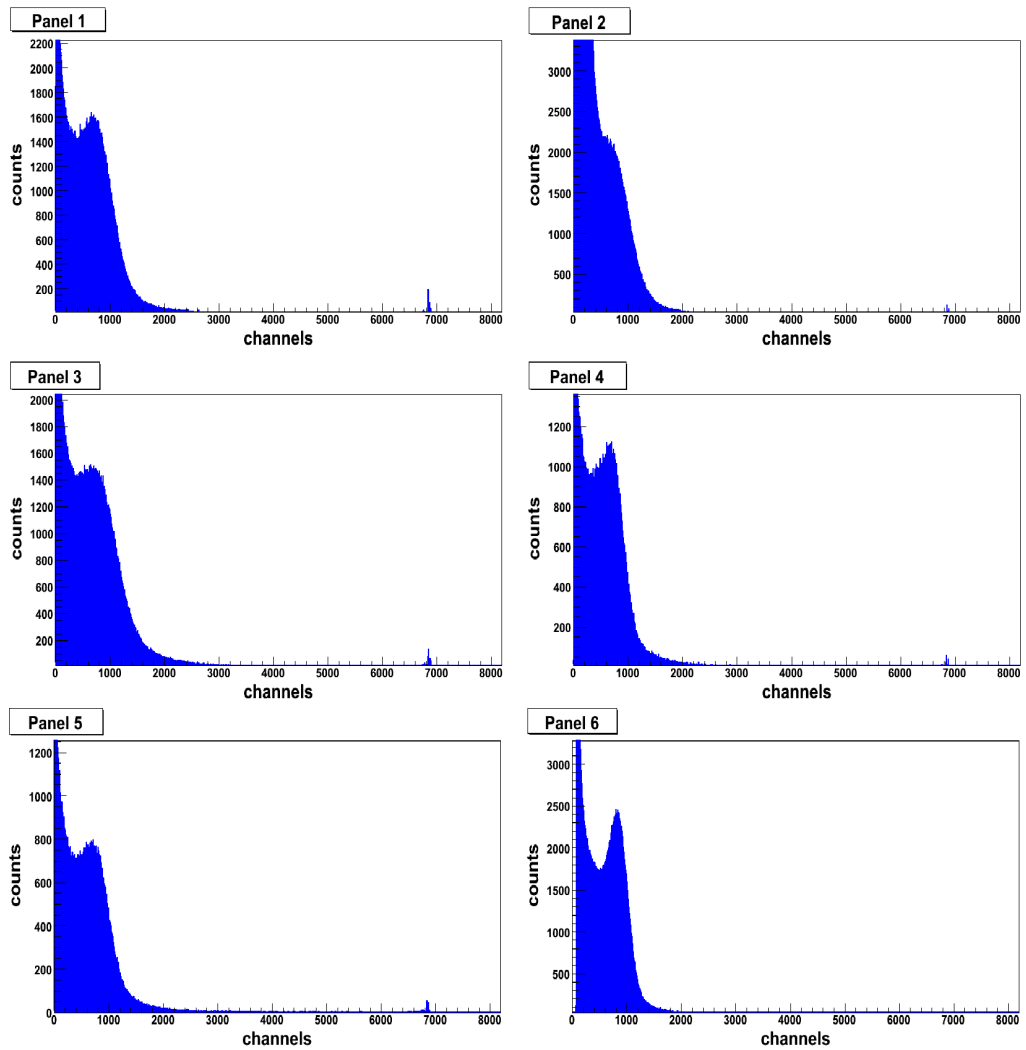


Figure B.3: The  $^{60}\text{Co}$  spectra of the six plastic scintillator panels after adjustment of the high voltage and optimising the focus potentiometer of the PMT bases. These spectra were recorded over 100 seconds measuring time.

# Appendix C

## Simulation of an isotropic source

The simulation of a source emitting gamma rays (or other particles) isotropically into  $4\pi$  solid angle was performed as follows: Two random numbers  $\vartheta$  and  $\varphi$  were chosen from the intervals  $[-1, 1]$  and  $[0, 2\pi]$ , respectively. Subsequently the x, y and z-components of the directional vector of the particle were computed by

$$\begin{aligned}x &= \sin(\arccos(\vartheta)) \cdot \cos(\varphi) \\y &= \sin(\arccos(\vartheta)) \cdot \sin(\varphi) \\z &= \cos(\arccos(\vartheta)) = \vartheta\end{aligned}\tag{C.1}$$

Figure C.1 shows the results of this computation. The ansatz

$$\begin{aligned}x &= \sin(\vartheta) \cdot \cos(\varphi) \\y &= \sin(\vartheta) \cdot \sin(\varphi) \\z &= \cos(\vartheta)\end{aligned}\tag{C.2}$$

with randomly chosen  $\vartheta \in [0, \pi]$  and  $\varphi \in [0, 2\pi]$  does **not** give isotropically distributed particle vectors, as the poles of the unit sphere are favoured, see fig. C.2.

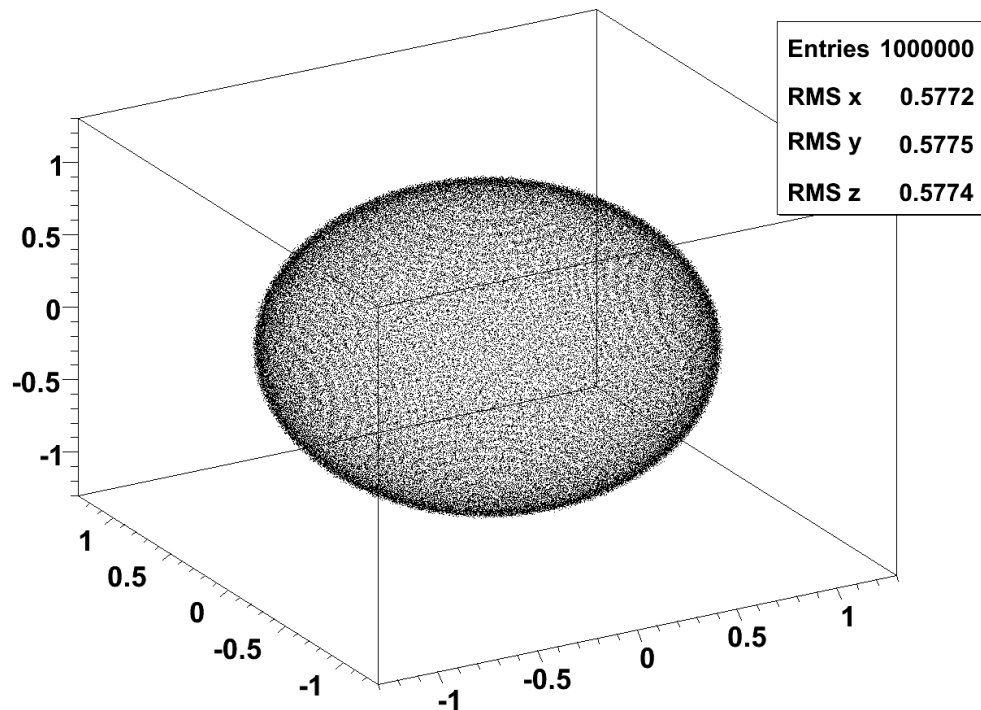


Figure C.1: *Three-dimensional plot of the directional vectors of the particles of one million randomly created events according to the correct method given by eq. (C.1). The root mean square values (RMS) given in the upper right corner of the picture show, that the  $x$ ,  $y$  and  $z$ -components are equally distributed, i.e. the particle emission happens isotropically. For particle vectors, which are normalized to one, the expectation value for RMS is  $\frac{1}{\sqrt{3}} \approx 0.57735$ .*

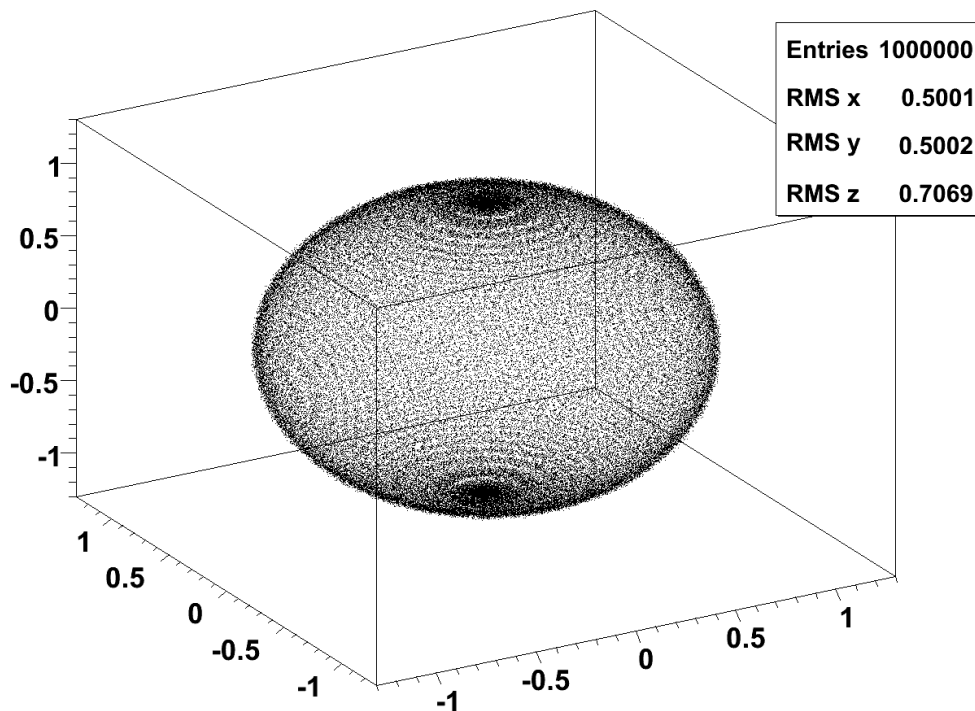


Figure C.2: *Three-dimensional plot of the directional vectors of the particles of one million randomly created events according to eq. (C.2), which, however, is a wrong ansatz. The  $x$ ,  $y$  and  $z$ -components are not equally distributed, in particular, the  $z$ -component is too large. Therefore the poles of the unit sphere are over-represented, what can clearly be seen in the picture as well as from the RMS values given in the box in the upper right corner.*



# Appendix D

## Gamma lines

This appendix lists the most important gamma lines of the natural background as seen in the germanium detector. This includes primordial isotopes as well as cosmogenic and anthropogenic elements. For the excited states (marked with an asterisk) of the different germanium isotopes also the half-life is given. Those states with lifetimes shorter than  $\approx 20 \mu\text{s}$  cannot be seen in the spectra with active muon-veto as their energy deposition in the germanium crystal lies within the veto window. These excited states are produced either by muons directly (indicated by a " $\mu$ " in the column "production") or by neutrons originating from spallation processes of cosmic muons in the lead in the shielding. In the column "production", also the decay chain is given for radioactive isotopes from such a chain (cf. also appendix E for all gamma energies appearing in these decay chains). All data taken from [Fir96, Led78], [GEN02a] and [Hen99].

<i>energy</i> [keV]	<i>from</i>	<i>production</i>	<i>half-life</i>
46.5	$^{210}\text{Pb} \xrightarrow{\beta^-} ^{210}\text{Bi}$	primordial, $^{238}\text{U}$ -chain	
66.7	$^{73}\text{Ge}^*$	$^{72}\text{Ge}(n, \gamma)^{73}\text{Ge}^*$ , $^{73}\text{Ge}(n, n')^{73}\text{Ge}^*$ , $^{74}\text{Ge}(n, 2n)^{73}\text{Ge}^*$ , $\mu$	0.49 s
68.8	$^{73}\text{Ge}^*$	$^{73}\text{Ge}(n, n')^{73}\text{Ge}^*$ , $^{74}\text{Ge}(n, 2n)^{73}\text{Ge}^*$ , $\mu$	1.74 ns
72.8	Pb $\text{K}_{\alpha 2}$	radiation, $\mu$	

<i>energy</i> [keV]	<i>from</i>	<i>production</i>	<i>half-life</i>
75.0	Pb K <sub>α1</sub>	radiation, $\mu$	
84.5	Pb K <sub>β3</sub>	radiation, $\mu$	
84.9	Pb K <sub>β1</sub>	radiation, $\mu$	
87.3	Pb K <sub>β2</sub>	radiation, $\mu$	
139.7	<sup>75</sup> Ge*	<sup>74</sup> Ge( <i>n</i> , $\gamma$ ) <sup>75</sup> Ge*, <sup>76</sup> Ge( <i>n</i> , 2 <i>n</i> ) <sup>75</sup> Ge*	47.7 s
159.7	<sup>77</sup> Ge*	<sup>76</sup> Ge( <i>n</i> , $\gamma$ ) <sup>77</sup> Ge*	52.9 s
186.2	<sup>226</sup> Ra $\xrightarrow{\alpha}$ <sup>222</sup> Rn	primordial, <sup>238</sup> U-chain	
198.4	<sup>71</sup> Ge*	<sup>70</sup> Ge( <i>n</i> , $\gamma$ ) <sup>71</sup> Ge*, <sup>72</sup> Ge( <i>n</i> , 2 <i>n</i> ) <sup>71</sup> Ge*	20.4 ms
238.6	<sup>212</sup> Pb $\xrightarrow{\beta^-}$ <sup>212</sup> Bi	primordial, Th-chain	
295.2	<sup>214</sup> Pb $\xrightarrow{\beta^-}$ <sup>214</sup> Bi	primordial, <sup>238</sup> U-chain	
338.3	<sup>228</sup> Ac $\xrightarrow{\beta^-}$ <sup>228</sup> Th	primordial, Th-chain	
351.9	<sup>214</sup> Pb $\xrightarrow{\beta^-}$ <sup>214</sup> Bi	primordial, <sup>238</sup> U-chain	
510.7	<sup>208</sup> Tl $\xrightarrow{\beta^-}$ <sup>208</sup> Pb	primordial, Th-chain	
511.0	<i>e</i> <sup>+</sup>	pair production, $\beta^+$ , $\mu$	
562.9	<sup>76</sup> Ge*	<sup>76</sup> Ge( <i>n</i> , <i>n'</i> ) <sup>76</sup> Ge*, $\mu$	18.2 ps
583.1	<sup>208</sup> Tl $\xrightarrow{\beta^-}$ <sup>208</sup> Pb	primordial, Th-chain	
595.9	<sup>74</sup> Ge*	<sup>73</sup> Ge( <i>n</i> , $\gamma$ ) <sup>74</sup> Ge*, <sup>74</sup> Ge( <i>n</i> , <i>n'</i> ) <sup>74</sup> Ge*, $\mu$	12.35 ps

<i>energy</i> [keV]	<i>from</i>	<i>production</i>	<i>half-life</i>
609.3	$^{214}\text{Bi} \xrightarrow{\beta^-} ^{214}\text{Po}$	primordial, $^{238}\text{U}$ -chain	
661.7	$^{137}\text{Cs} \xrightarrow{\beta^-} ^{137m}\text{Ba}$	anthropogenic	
691.6	$^{72}\text{Ge}^*$	$^{72}\text{Ge}(n, n')^{72}\text{Ge}^*$ , $^{73}\text{Ge}(n, 2n)^{72}\text{Ge}^*$ , $\mu$	444.2 ns
727.2	$^{212}\text{Bi} \xrightarrow{\beta^-} ^{212}\text{Po}$	primordial, Th-chain	
834.1	$^{72}\text{Ge}^*$	$^{72}\text{Ge}(n, n')^{72}\text{Ge}^*$ , $^{73}\text{Ge}(n, 2n)^{72}\text{Ge}^*$ , $\mu$	3.35 ps
860.4	$^{208}\text{Tl} \xrightarrow{\beta^-} ^{208}\text{Pb}$	primordial, Th-chain	
911.1	$^{228}\text{Ac} \xrightarrow{\beta^-} ^{228}\text{Th}$	primordial, Th-chain	
969.1	$^{228}\text{Ac} \xrightarrow{\beta^-} ^{228}\text{Th}$	primordial, Th-chain	
1039.3	$^{70}\text{Ge}^*$	$^{70}\text{Ge}(n, n')^{70}\text{Ge}^*$ , $\mu$	1.3 ps
1120.3	$^{214}\text{Bi} \xrightarrow{\beta^-} ^{214}\text{Po}$	primordial, $^{238}\text{U}$ -chain	
1173.2	$^{60}\text{Co} \xrightarrow{\beta^-} ^{60}\text{Ni}$	anthropogenic	
1204.2	$^{74}\text{Ge}^*$	$^{73}\text{Ge}(n, \gamma)^{74}\text{Ge}^*$ , $^{74}\text{Ge}(n, n')^{74}\text{Ge}^*$ , $\mu$	4.9 ps
1215.4	$^{70}\text{Ge}^*$	$^{70}\text{Ge}(n, n')^{70}\text{Ge}^*$ , $\mu$	3.7 ns
1238.1	$^{214}\text{Bi} \xrightarrow{\beta^-} ^{214}\text{Po}$	primordial, $^{238}\text{U}$ -chain	
1332.5	$^{60}\text{Co} \xrightarrow{\beta^-} ^{60}\text{Ni}$	anthropogenic	
1377.7	$^{214}\text{Bi} \xrightarrow{\beta^-} ^{214}\text{Po}$	primordial, $^{238}\text{U}$ -chain	
1401.5	$^{214}\text{Bi} \xrightarrow{\beta^-} ^{214}\text{Po}$	primordial, $^{238}\text{U}$ -chain	

<i>energy</i> [keV]	<i>from</i>	<i>production</i>	<i>half-life</i>
1408.0	$^{214}\text{Bi} \xrightarrow{\beta^-} ^{214}\text{Po}$	primordial, $^{238}\text{U}$ -chain	
1460.8	$^{40}\text{K} \xrightarrow{\beta^+, \text{EC}} ^{40}\text{Ar}$	primordial	
1463.8	$^{74}\text{Ge}^*$	$^{73}\text{Ge}(n, \gamma)^{74}\text{Ge}^*$ , $^{74}\text{Ge}(n, n')^{74}\text{Ge}^*$ , $\mu$	1.7 ps
1464.1	$^{72}\text{Ge}^*$	$^{72}\text{Ge}(n, n')^{72}\text{Ge}^*$ , $^{73}\text{Ge}(n, 2n)^{72}\text{Ge}^*$ , $\mu$	4.5 ps
1509.2	$^{214}\text{Bi} \xrightarrow{\beta^-} ^{214}\text{Po}$	primordial, $^{238}\text{U}$ -chain	
1587.9	$^{228}\text{Ac} \xrightarrow{\beta^-} ^{228}\text{Th}$	primordial, Th-chain	
1661.3	$^{214}\text{Bi} \xrightarrow{\beta^-} ^{214}\text{Po}$	primordial, $^{238}\text{U}$ -chain	
1728.4	$^{72}\text{Ge}^*$	$^{72}\text{Ge}(n, n')^{72}\text{Ge}^*$ , $^{73}\text{Ge}(n, 2n)^{72}\text{Ge}^*$ , $\mu$	1.5 ps
1729.6	$^{214}\text{Bi} \xrightarrow{\beta^-} ^{214}\text{Po}$	primordial, $^{238}\text{U}$ -chain	
1764.5	$^{214}\text{Bi} \xrightarrow{\beta^-} ^{214}\text{Po}$	primordial, $^{238}\text{U}$ -chain	
1847.4	$^{214}\text{Bi} \xrightarrow{\beta^-} ^{214}\text{Po}$	primordial, $^{238}\text{U}$ -chain	
2118.5	$^{214}\text{Bi} \xrightarrow{\beta^-} ^{214}\text{Po}$	primordial, $^{238}\text{U}$ -chain	
2204.2	$^{214}\text{Bi} \xrightarrow{\beta^-} ^{214}\text{Po}$	primordial, $^{238}\text{U}$ -chain	
2447.8	$^{214}\text{Bi} \xrightarrow{\beta^-} ^{214}\text{Po}$	primordial, $^{238}\text{U}$ -chain	
2614.5	$^{208}\text{Tl} \xrightarrow{\beta^-} ^{208}\text{Pb}$	primordial, Th-chain	

Table D.1: *Energy and origin of the gamma lines*

# Appendix E

## Decay chains

On the following pages the three natural decay chains including their branchings are shown. Numbers in red give the energies of the gamma rays released after each decay (in keV) and the relative intensity of the respective line. The colouring of the isotopes is the same as used in the Karlsruhe Nuclide Chart: yellow stands for  $\alpha$ -decay, blue for  $\beta^-$ -decay, green for spontaneous fission and black for stable isotopes. For each isotope also the half-life is given (small number in the box). All data taken from [Fir96, Led78].

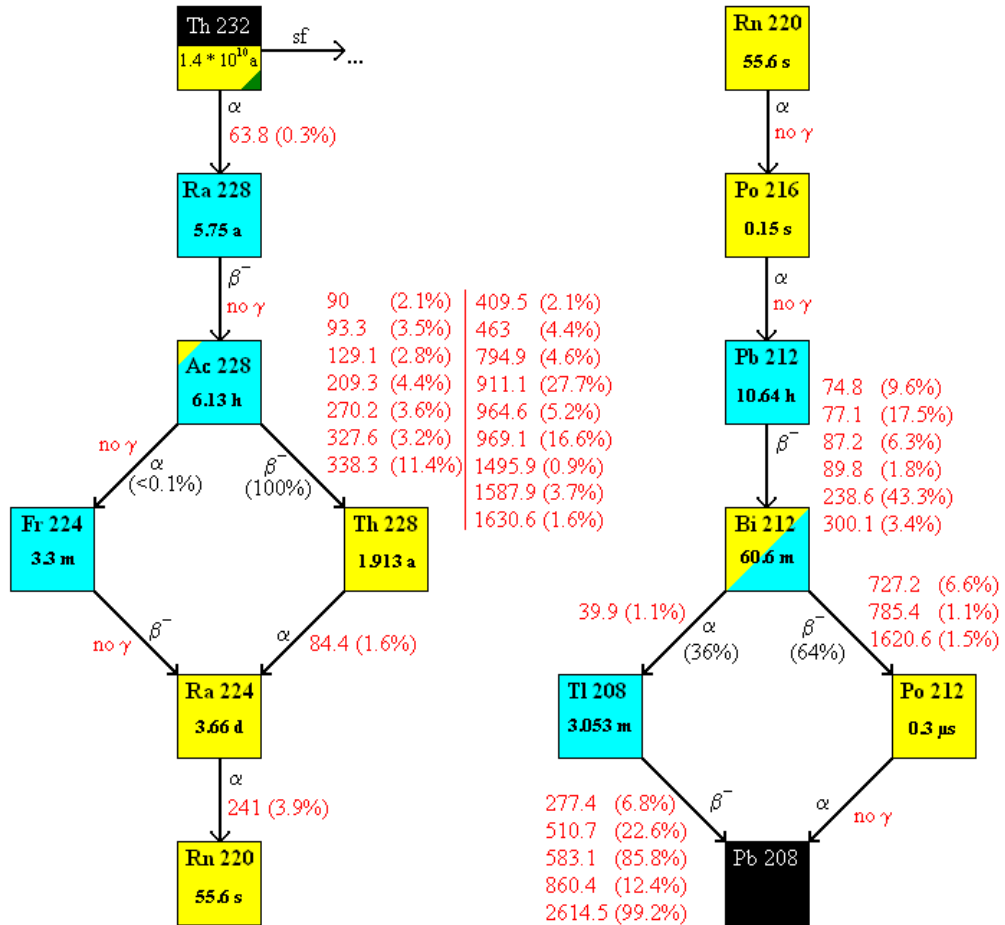


Figure E.1: The decay chain of Th-232 including all gamma lines (energy in keV) and their relative intensities. The tag "no  $\gamma$ " means that either there is no gamma emission at all or the relative intensity is so low, that the gamma line can be neglected in comparison to the other lines of the whole chain.

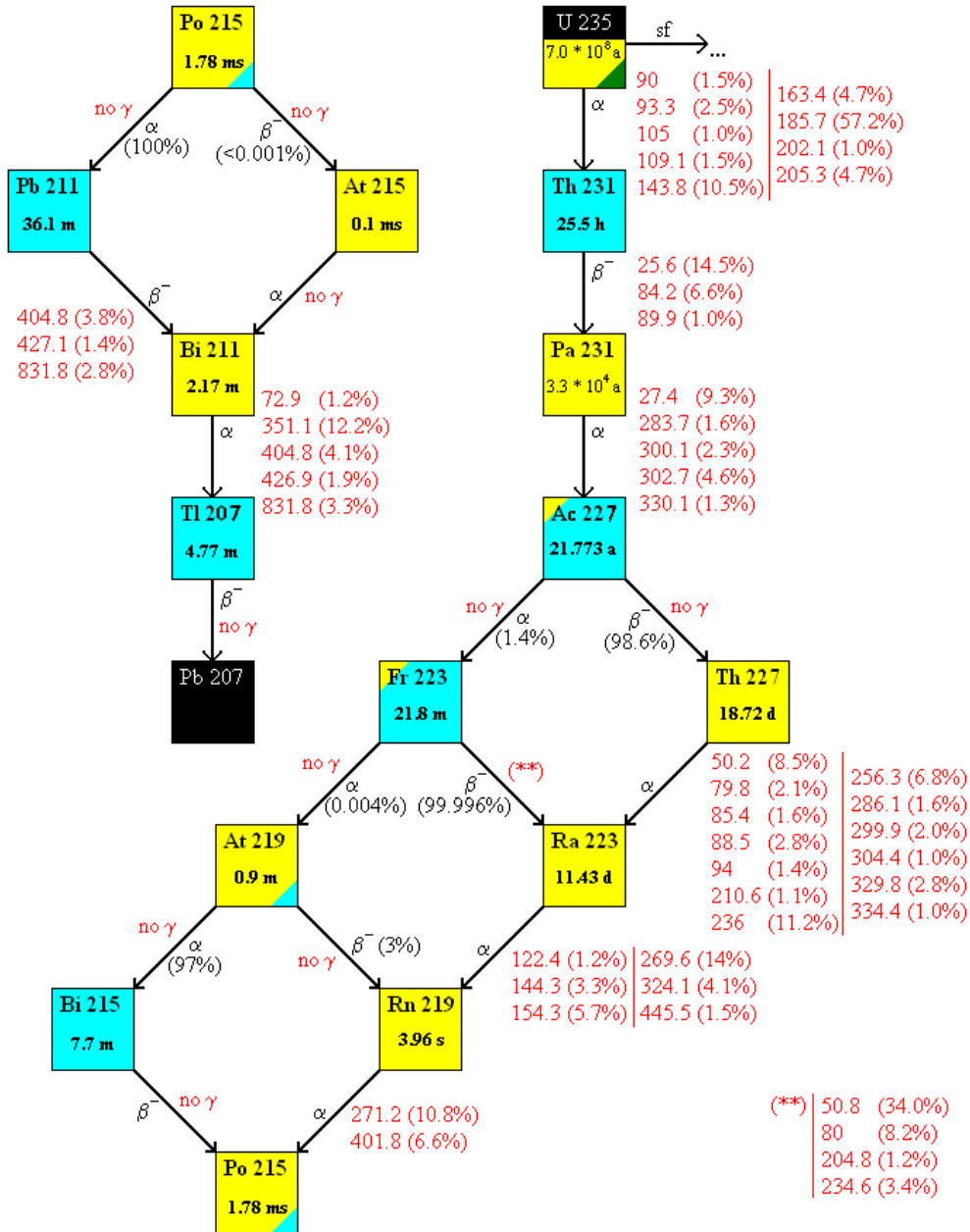


Figure E.2: The decay chain of  $U\text{-}235$  including all gamma lines (energy in keV) and their relative intensities. The tag "no  $\gamma$ " means that either there is no gamma emission at all or the relative intensity is so low, that the gamma line can be neglected in comparison to the other lines of the whole chain.

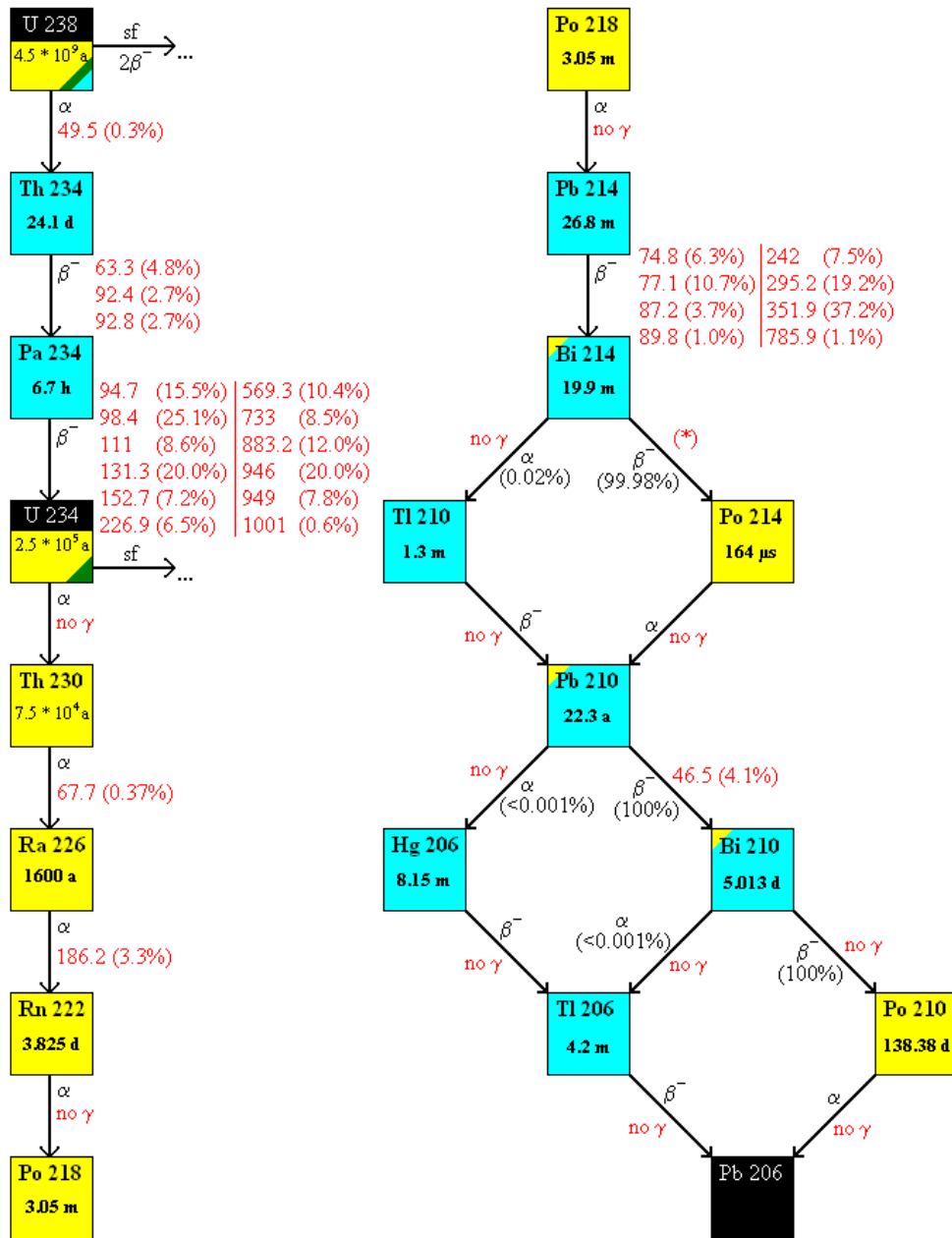


Figure E.3: The decay chain of  $U$ -238 including all gamma lines (energy in keV) and their relative intensities. The tag "no  $\gamma$ " means that either there is no gamma emission at all or the relative intensity is so low, that the gamma line can be neglected in comparison to the other lines of the whole chain. The various gamma rays appearing in the decay of  $^{214}\text{Bi}$  to  $^{214}\text{Po}$  (marked in the picture with "(\*)") are listed in table E.1.

---

Gamma energy [keV]	Relative intensity
609.3	46.3%
665.5	1.3%
768.4	5.0%
806.2	1.2%
934.1	3.2%
1120.3	15.1%
1155.2	1.7%
1238.1	5.9%
1281.0	1.5%
1377.7	4.1%
1385.3	0.8%
1401.5	1.4%
1408.0	2.5%
1509.2	2.2%
1661.3	1.1%
1729.6	3.0%
1764.5	15.8%
1847.4	2.1%
2118.5	1.2%
2204.2	5.0%
2447.8	1.6%

Table E.1: *Gamma lines appearing in the decay of  $^{214}\text{Bi}$  to  $^{214}\text{Po}$  and their relative intensities.*



# Appendix F

## Decay schemes of selected isotopes

This appendix shows the decay schemes or parts of the decay schemes of three selected isotopes,  $^{212}\text{Pb}$ ,  $^{214}\text{Bi}$  and  $^{208}\text{Tl}$ . The gamma transitions marked in red are used for the calculation of the activities of the respective radionuclides, see itemisation on page 77 in chapter 5.2.2. The transitions marked in blue indicate the gamma cascades, i.e., the population of low-energetic excited states by gamma transitions from high-energetic excited states. For each transition the energy of the gamma line is given, as well as the relative intensity. The arrows on the lefthand side of the decay schemes point to the energy levels of the daughter nuclide, which are directly populated after the decay of the mother isotope, including the branching ratio. The energy of each excited state is given on the righthand side of the decay schemes. All data taken from [Fir96].

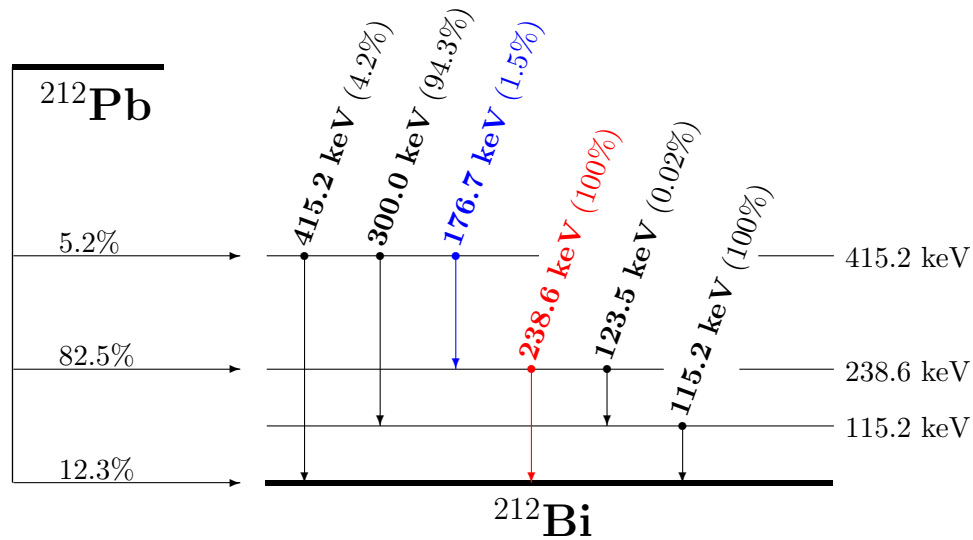


Figure F.1: Decay scheme of the  $\beta^-$ -decay of  $^{212}\text{Pb}$  into  $^{212}\text{Bi}$ . For the 238.6 keV line of this isotope all effects from gamma cascades can be neglected, as the relative intensity of the 176.7 keV line is very low. The gamma transition with an energy of 238.6 keV comes from an excited state of  $^{212}\text{Bi}$ , which is highly populated in the decay of  $^{212}\text{Pb}$ , and goes directly to the ground state of  $^{212}\text{Bi}$ , not being followed by further gamma quanta. The 415.2 keV gamma line is not used for an analysis, as its total intensity is far below 1% (5.2% from the branching ratio of the population times 4.2% from the relative intensity).

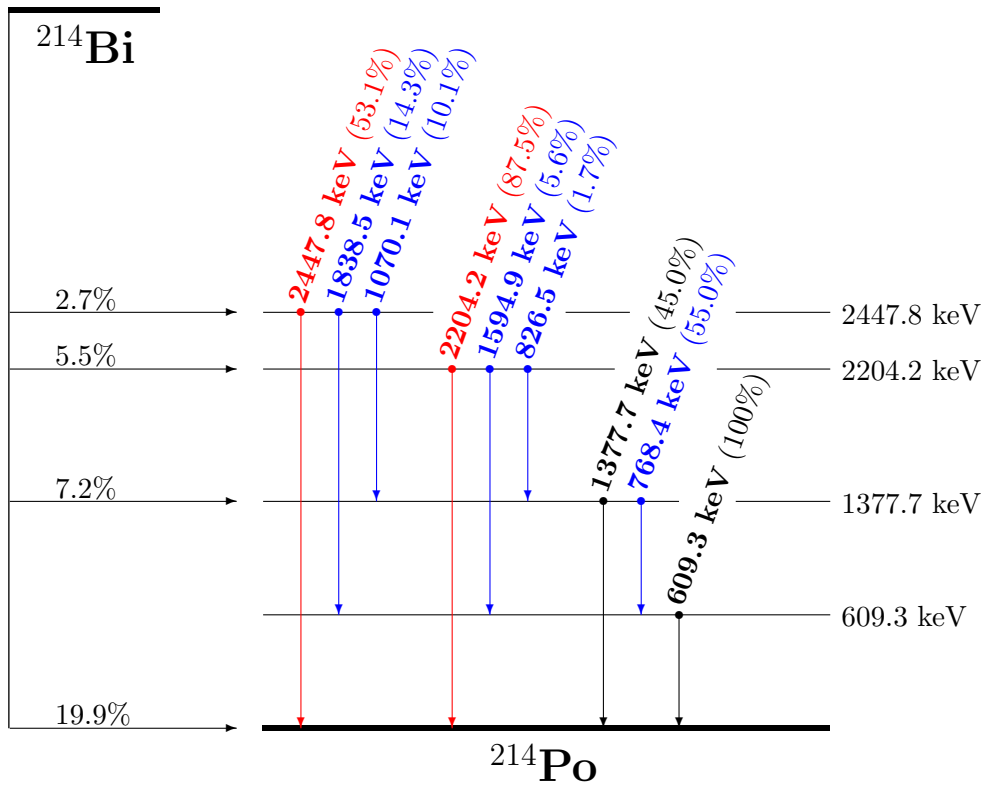


Figure F.2: Simplified decay scheme of the  $\beta^-$ -decay of  $^{214}\text{Bi}$  into  $^{214}\text{Po}$ . Not all excited states of this very complex scheme are shown; therefore the sum of the single branching ratios deviates in some cases from 100%. The two high-energetic transitions with gamma energies of 2447.8 keV and 2204.2 keV fulfill the requirements stated in chapter 5.2.2, i.e., they go directly to the ground state of  $^{214}\text{Po}$  and are not populated from states with higher energy. The population of the state at 1377.7 keV from high-energetic excited (also from many states not shown here) is not negligible. Therefore, this gamma line was excluded from the analysis. The state at 609.3 keV is not populated directly in the decay of  $^{214}\text{Bi}$  and only part of gamma cascades, excluding this line too.

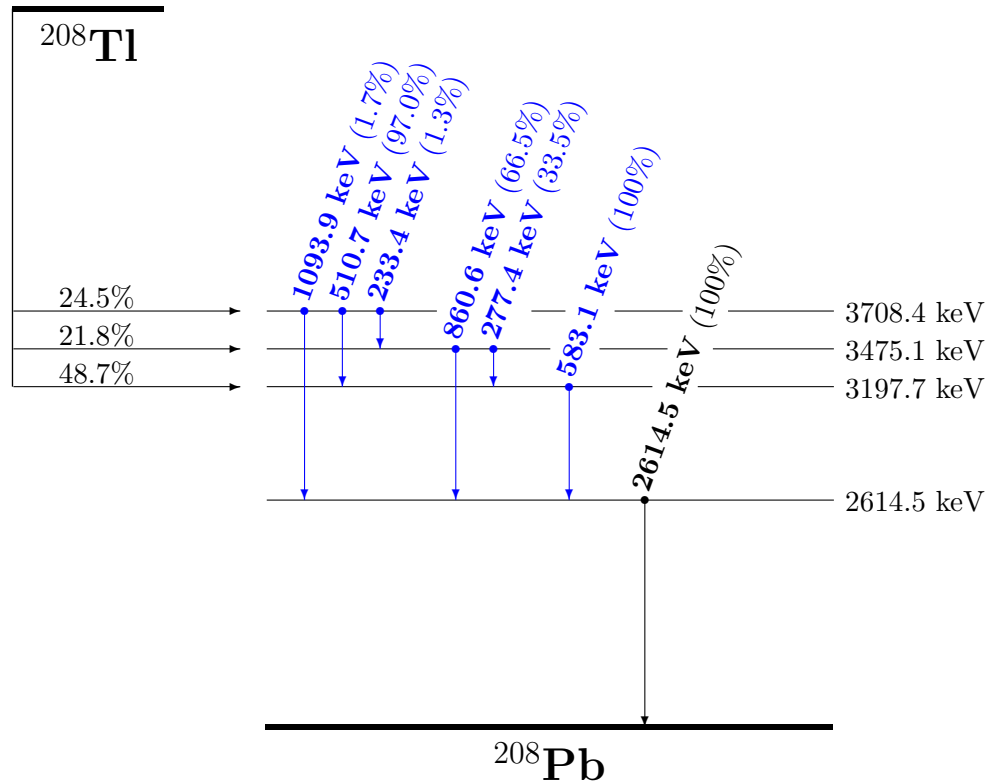


Figure F.3: *Simplified decay scheme of the  $\beta^-$ -decay of  $^{208}\text{Tl}$  into  $^{208}\text{Pb}$ . Again, not all excited states of the daughter isotope are shown. All excited states, populated directly in the decay of  $^{208}\text{Tl}$ , have no direct transition into the ground state of  $^{208}\text{Pb}$ , but first of all the state at 2614.5 keV is populated. Thus, all gamma lines are followed by 2614.5 keV gamma quanta, which results in the fact, that the requirements given in chapter 5.2.2 (i.e. particularly direct transitions to the ground state of the daughter isotope) are not met.  $^{208}\text{Tl}$  has no suitable gamma line for an analysis as described in the main text.*

# Appendix G

## Glossar

<b>ADC</b>	Analogue-to-digital converter
<b>AIM</b>	Acquisition interface module
<b>bisMSB</b>	1,4-bis-(o-Methylstyryl)-Benzole
<b>BLR</b>	Base line restorer
<b>BNC</b>	Bayonet Neill Concelman (Bayonet Navy Connector)
<b>CAS</b>	Chemical Abstracts Service
<b>CFD</b>	Constant fraction discriminator
<b>CFT</b>	Constant fraction trigger
<b>C.L.</b>	Confidence level
<b>CP</b>	Charge and parity conjugation
<b>cpm</b>	counts per minute
<b>DSP</b>	Digital signal processor
<b>FWHM</b>	Full width at half maximum
<b>GG</b>	Gate generator
<b>GRT</b>	General relativity
<b>GSW</b>	Glashow-Salam-Weinberg mechanism
<b>HPGe</b>	High purity germanium
<b>HV</b>	High voltage
<b>LAB</b>	Linear alcyyl benzene
<b>LMA</b>	Large mixing angle
<b>LN<sub>2</sub></b>	Liquid nitrogen
<b>MSW</b>	Mikheyev-Smirnov-Wolfenstein effect
<b>m.w.e.</b>	Metres of water equivalent; 1 m.w.e. $\hat{=}$ 100 g/cm <sup>2</sup>
<b>NIM</b>	Nuclear instrumentation module
<b>P/Z</b>	Pole zero
<b>PC</b>	Personal computer
<b>PEHD</b>	Polyethylene high-density
<b>PHA+</b>	Pulse height aquisition

<b><i>PMNS</i></b>	Pontecorvo-Maki-Nakagawa-Sakata matrix
<b><i>PMT</i></b>	Photomultiplier tube
<b><i>PPO</i></b>	2,5-Diphenyloxazole
<b><i>PTFE</i></b>	Polytetrafluoroethylene (Teflon)
<b><i>PVC</i></b>	Polyvinyl chloride
<b><i>PVT</i></b>	Polyvinyl toluene
<b><i>QCD</i></b>	Quantum chromodynamics
<b><i>QED</i></b>	Quantum electrodynamics
<b><i>RMS</i></b>	Root mean square
<b><i>TFA</i></b>	Timing filter amplifier
<b><i>TTL</i></b>	Transistor-transistor logic

# List of Figures

1.1	<i>Picture of the sun in "neutrino light"</i> . . . . .	10
1.2	<i>Exclusion plot of the CHOOZ experiment</i> . . . . .	12
2.1	<i>The Chooz reactor site</i> . . . . .	18
2.2	<i>Survival probability of electron antineutrinos as function of L/E</i>	19
2.3	<i>Intended sensitivity of the DOUBLE CHOOZ project</i> . . . . .	20
2.4	<i>Cross section of the DOUBLE CHOOZ detectors</i> . . . . .	22
3.1	<i>The opened detection system</i> . . . . .	26
3.2	<i>The Garching underground laboratory</i> . . . . .	28
3.3	<i>Cross section of the germanium detector</i> . . . . .	29
3.4	<i>The open anti-Compton veto system</i> . . . . .	30
3.5	<i>Working principle of the anti-Compton veto</i> . . . . .	31
3.6	<i><math>^{137}\text{Cs}</math>-spectra of all seven multipliers of the anti-Compton veto showing the double-peaks</i> . . . . .	33
3.7	<i><math>^{137}\text{Cs}</math>-spectra of the lower-left PMT with different positions of the gain (focus) potentiometer</i> . . . . .	34
3.8	<i>Final <math>^{137}\text{Cs}</math>-spectra of the three anti-Compton veto parts</i> . . . . .	36
3.9	<i>Active muon-veto system</i> . . . . .	37
3.10	<i>Chemical structure of polyvinyl toluene</i> . . . . .	38
3.11	<i>Schematic view of the plastic scintillator panels</i> . . . . .	39
3.12	<i>Muon spectra of the panels</i> . . . . .	41
3.13	<i>Wiring diagramme of the read-out electronics</i> . . . . .	42
4.1	<i>Tree diagramme of the source code of the simulation</i> . . . . .	50
4.2	<i>Tracked gamma ray in GEANT4</i> . . . . .	51
4.3	<i>Calibration sources used for measuring the detector efficiency</i> .	55
4.4	<i>Measured versus simulated detector efficiencies</i> . . . . .	58
5.1	<i>Comparison of spectra with and without active veto systems</i> . .	63
5.2	<i>Background spectrum, recorded with the germanium detector</i> .	64
5.3	<i>Low-energy part of the background spectrum</i> . . . . .	65

---

5.4	<i>Gaussian error distribution curve</i> . . . . .	76
6.1	<i>Future detector system consisting of two identical germanium detectors enclosed by an anti-Compton veto</i> . . . . .	96
A.1	$^{137}\text{Cs}$ -spectra of the different scintillator parts with 850 V . . .	100
A.2	$^{137}\text{Cs}$ -spectra of the different scintillator parts with 900 V . . .	101
A.3	$^{137}\text{Cs}$ -spectra of the different scintillator parts with 950 V . . .	102
A.4	$^{137}\text{Cs}$ -spectra of the three upper PMTs recontacted with optical compound . . . . .	104
B.1	$^{60}\text{Co}$ spectra of panel 1 for different HV . . . . .	106
B.2	$^{60}\text{Co}$ spectra of the panels at 1400 V . . . . .	107
B.3	$^{60}\text{Co}$ spectra of the panels after focus adjustment . . . . .	108
C.1	<i>Three-dimensional illustration of the isotropy of the source</i> . .	110
C.2	<i>Three-dimensional illustration of the particle directional vectors for wrong calculation</i> . . . . .	111
E.1	<i>Thorium decay chain</i> . . . . .	118
E.2	<i>Uranium-235 decay chain</i> . . . . .	119
E.3	<i>Uranium-238 decay chain</i> . . . . .	120
F.1	<i>Decay scheme of <math>^{212}\text{Pb}</math></i> . . . . .	124
F.2	<i>Simplified decay scheme of <math>^{214}\text{Bi}</math></i> . . . . .	125
F.3	<i>Simplified decay scheme of <math>^{208}\text{Tl}</math></i> . . . . .	126

# List of Tables

1.1	<i>The fundamental fermions in the standard model</i>	1
1.2	<i>Fermion properties</i>	3
1.3	<i>The fundamental interactions</i>	4
1.4	<i>Gauge boson properties</i>	5
1.5	<i>Neutrino oscillation parameters</i>	8
3.1	<i>Serial numbers of the anti-Compton veto</i>	31
3.2	<i>Energy resolution of the anti-Compton veto parts</i>	35
3.3	<i>Serial numbers of the muon-veto panels</i>	38
3.4	<i>HV bias of the muon-veto</i>	40
3.5	<i>Discriminator thresholds for the muon-veto panels</i>	45
3.6	<i>Energy resolution obtained with the DSP 9660A</i>	47
4.1	<i>Particles and interactions included in the Monte-Carlo simulation</i>	52
4.2	<i>Simulated efficiencies for different geometries</i>	53
4.3	<i>Simulated efficiencies for different asymmetric geometries</i>	54
4.4	<i>Measured detector efficiencies for different geometries</i>	56
4.5	<i>Measured detector efficiencies for different asymmetric geometries</i>	57
5.1	<i>Number of background counts recorded with the germanium detector</i>	66
5.2	<i>Chemical structure and main properties of LAB</i>	68
5.3	<i>Chemical structure and main properties of tetradecane</i>	69
5.4	<i>Chemical structure and main properties of PPO</i>	70
5.5	<i>Chemical structure and main properties of bisMSB</i>	71
5.6	<i>Gamma lines and respective number of counts found in the analysis of the samples for the low-energetic part</i>	72
5.7	<i>Gamma lines and respective number of counts found in the analysis of the samples for the medium-energetic part</i>	73

5.8	<i>Gamma lines and respective number of counts found in the analysis of the samples for the high-energetic part . . . . .</i>	74
5.9	<i>Final results for the plastic containers for <math>^{40}\text{K}</math>, Th and <math>^{238}\text{U}</math> .</i>	80
5.10	<i>Final results for the plastic containers for <math>^{235}\text{U}</math> . . . . .</i>	81
5.11	<i>Final results for the organic liquids for <math>^{40}\text{K}</math>, Th and <math>^{238}\text{U}</math> . . .</i>	82
5.12	<i>Final results for the organic liquids for <math>^{235}\text{U}</math> . . . . .</i>	83
5.13	<i>Final results for the wavelength shifters for <math>^{40}\text{K}</math>, Th and <math>^{238}\text{U}</math> .</i>	84
5.14	<i>Final results for the wavelength shifters for <math>^{235}\text{U}</math> . . . . .</i>	85
5.15	<i>Summary of the final results of the low-background gamma spectroscopy . . . . .</i>	86
5.16	<i>Allowed mass concentrations for the radioactive isotopes in DOUBLE CHOOZ . . . . .</i>	89
5.17	<i>Allowed mass concentrations for the radioactive isotopes for the wave-length shifters . . . . .</i>	92
6.1	<i>Summary of the final results of the low-background gamma spectroscopy . . . . .</i>	95
A.1	<i>Position of the <math>^{137}\text{Cs}</math> peak for the three multipliers in the upper half shell of the anti-Compton veto before and after gain (focus) adjustment . . . . .</i>	103
A.2	<i>Position of the <math>^{137}\text{Cs}</math> peak for the three multipliers in the upper half shell of the anti-Compton veto before and after gain (focus) adjustment without optical compound . . . . .</i>	103
A.3	<i>Position of the <math>^{137}\text{Cs}</math> peak for the three multipliers in the upper half shell of the anti-Compton veto before and after gain (focus) adjustment recontacted with optical compound . . . . .</i>	104
D.1	<i>Gamma lines . . . . .</i>	116
E.1	<i>Gamma lines from <math>^{214}\text{Bi}</math> . . . . .</i>	121

# Bibliography

- [Aba91] A.I. ABAZOV ET AL.: "*Search for neutrinos from the sun using the reaction  $^{71}\text{Ga}(\nu_e, e^-)^{71}\text{Ge}$* ", Phys. Rev. Lett. **67**, 3332 (1991)
- [Abd02] J.N. ABDURASHITOV ET AL.: "*Solar neutrino flux measurements by the Soviet-American Gallium Experiment (SAGE) for half the 22-year solar cycle*", Jour. Exp. Theo. Phys. **95** No.2, 181 (2002)
- [AEA01] AEA TECHNOLOGY QSA, ISOTRAK, Gieselweg 1, D-38110 Braunschweig: *Catalogue*, 2<sup>nd</sup> edition (2001)
- [Ago03] S. AGOSTINELLI ET AL.: "*Geant4 - A simulation toolkit*", Nucl. Instr. Meth. A **506**, 250 (2003)
- [Ahm02] Q.R. AHMAD ET AL., SNO collaboration: "*Direct evidence for neutrino flavour transformation from neutral-current interactions in the Sudbury Neutrino Observatory*", Phys. Rev. Lett. **87**, 071301 (2001) [arXiv:nucl-ex/0204008 and arXiv:nucl-ex/0204009]
- [Ahn06] M.H. AHN ET AL., K2K collaboration: "*Measurement of neutrino oscillation by the K2K experiment*", Phys. Rev. D **74**, 072003 (2006) [arXiv:hep-ex/0606032v3]
- [Ait89] I.J.R. AITCHISON AND A.J.G. HEY: "*Gauge theories in particle physics*", 2<sup>nd</sup> edition, Adam Hilger, Bristol and Philadelphia (1989)
- [Akh00] E.K. AKHMEDOV: "*Neutrino physics*", arXiv:hep-ph/0001264v2
- [Akh06] E.K. AKHMEDOV: "*Neutrino oscillations: theory and phenomenology*", arXiv:hep-ph/0610064v2
- [Ali00] G. ALIMONTI ET AL., BOREXINO collaboration: "*Science and technology of BOREXINO: A real time detector for low energy*

- solar neutrinos*", *Astropart.Phys.* **16**, 205 (2002) [arXiv:hep-ex/0012030]
- [All06] J. ALLISON ET AL.: "*Geant4 developments and applications*", *IEEE Trans. Nucl. Sci.* **53** No.1, 270 (2006)
- [Alt00] M. ALTMANN ET AL.: "*GNO solar neutrino observations: results for GNO I*", *Phys. Lett. B* **490**, 16 (2000) [arXiv:hep-ex/0006034]
- [Alt05] M. ALTMANN ET AL.: "*Complete results for five years of GNO solar neutrino observations*", *Phys. Lett. B* **616**, 174 (2005) [arXiv:hep-ex/0504037]
- [Alt05a] G. ALTARELLI: "*The Standard Model of Particle Physics*", arXiv:hep-ph/0510281
- [And04] K. ANDERSON ET AL.: "*White paper report on using nuclear reactors to search for a value of  $\vartheta_{13}$* ", arXiv:hep-ex/0402041
- [Anj05] J.C. ANJOS ET AL.: "*Angra neutrino project: status and plans*", arXiv:hep-ex/0511059
- [Ans92] P. ANSELMANN ET AL.: "*Solar neutrinos observed by GALLEX at Gran Sasso*", *Phys. Lett. B* **285**, 376 (1992)
- [Apo99] M. APOLLONIO ET AL., CHOOZ collaboration: "*Limits on neutrino oscillations from the CHOOZ experiment*", *Phys. Lett. B* **466**, 415 (1999) [see also Erratum, *Phys. Lett. B* **472**, 434 (1999)], [arXiv:hep-ex/9907037]
- [Apo03] M. APOLLONIO ET AL., CHOOZ collaboration: "*Search for neutrino oscillations on a long base-line at the CHOOZ nuclear power station*", *Eur. Phys. J. C* **27**, 331 (2003) [arXiv:hep-ex/0301017]
- [Ard04] F. ARDELLIER ET AL., DOUBLE CHOOZ collaboration: "*Letter of Intent for DOUBLE CHOOZ: a search for the mixing angle  $\theta_{13}$* ", arXiv:hep-ex/0405032
- [Ard06] F. ARDELLIER ET AL., DOUBLE CHOOZ collaboration: "*DOUBLE CHOOZ, A search for the neutrino mixing angle  $\theta_{13}$* ", arXiv:hep-ex/0606025v4
- [Ber04] S. BERRIDGE ET AL.: "*Proposal for U.S. participation in DOUBLE CHOOZ: A new  $\vartheta_{13}$  experiment at the Chooz reactor*", arXiv:hep-ex/0410081

- [Bev69] P.R. BEVINGTON: *"Data reduction and error analysis for the physical sciences"*, McGraw-Hill Companies, New York (1969)
- [Bil78] S.M. BILENKY AND B. PONTECORVO: *"Lepton mixing and neutrino oscillations"*, Phys. Rept. **41**, 225 (1978)
- [Bil99] S.M. BILENKY, C. GIUNTI, AND W. GRIMUS: *"Phenomenology of neutrino oscillations"*, Prog. Part. Nucl. Phys. **43**, 1 (1999) [arXiv:hep-ph/9906251]
- [Bil01] S.M. BILENKY, D. NICOLO, AND S.T. PETCOV: *"Constraints on  $|U_{e3}|^2$  from a three-Neutrino oscillation analysis of the CHOOZ data"*, Phys. Lett. B **538**, 77 (2002) [arXiv:hep-ph/0112216]
- [Bor07] BOREXINO COLLABORATION: *"First real time detection of  $^7\text{Be}$  solar neutrinos by BOREXINO"*, arXiv:0708.2251v2 [astro-ph]
- [CER94] CERN PROGRAM LIBRARY OFFICE: *"GEANT detector description and simulation tool"*,  
<http://wwwasdoc.web.cern.ch/wwwasdoc/pdfdir/geant.pdf>
- [CER07] CERN GEANT4 HOMEPAGE,  
<http://geant4.web.cern.ch/geant4/>
- [Cle98] B.T. CLEVELAND ET AL.: *"Measurement of the solar electron neutrino flux with the Homestake Chlorine detector"*, Astrophys. Jour. **496**, 505 (1998)
- [Dav68] R. DAVIS, JR. ET AL.: *"Search for neutrinos from the sun"*, Phys. Rev. Lett. **20**, 1205 (1968)
- [Day07] DAYA BAY COLLABORATION: *"Proposal: A precision measurement of the neutrino mixing angle  $\vartheta_{13}$  using reactor antineutrinos at Daya Bay"*, arXiv:hep-ex/0701029
- [Doi81] M. DOI ET AL.: *"CP violation in Majorana neutrinos"*, Phys. Lett. B **102**, 323 (1981)
- [Egu03] K. EGUCHI ET AL., KamLAND collaboration: *"First results from KamLAND: Evidence for reactor antineutrino disappearance"*, Phys. Rev. Lett. **90**, 021802 (2003) [arXiv:hep-ex/0212021]
- [Fir96] R.B. FIRESTONE AND V.S. SHIRLEY (ED.): *"Table of isotopes"*, 8<sup>th</sup> edition, John Wiley & sons (1996)

- [Fuk94] Y. FUKUDA ET AL.: "*Atmospheric  $\nu_\mu/\nu_e$  ratio in the multi-GeV energy range*", Phys. Lett. B **335**, 237 (1994)
- [GEN02] CANBERRA EURISYS GMBH, Walter-Flex-Str. 66, D-65428 Rüsselsheim: "*Genie-2000 Benutzerhandbuch für die Gammaspektrometrie*", Version 2.1 (2002)
- [GEN02a] CANBERRA EURISYS GMBH, Walter-Flex-Str. 66, D-65428 Rüsselsheim: Library of gamma lines included in Genie-2000, Version 2.1 (2002)
- [Giu04] C. GIUNTI: "*Theory of neutrino oscillations*", arXiv:hep-ph/0409230
- [Hal84] F. HALZEN AND A.D. MARTIN: "*Quarks & leptons*", John Wiley & sons (1984)
- [Ham99] W. HAMPEL ET AL.: "*GALLEX solar neutrino observations: results for GALLEX IV*", Phys. Lett. B **447**, 127 (1999)
- [Hen99] R. VON HENTIG: "*Spurenanalyse primordialler Radionuklide für das solare Neutrinoexperiment BOREXINO*", Dissertation, Technische Universität München (1999)
- [Hub02] P. HUBER ET AL.: "*Reactor neutrino experiments compared to superbeams*", Nucl. Phys. B **665**, 487 (2003) [arXiv:hep-ph/0303232v2]
- [Ish04] M. ISHITSUKA for the Super-Kamiokande collaboration: "*Super-Kamiokande results: atmospheric and solar neutrinos*", arXiv:hep-ex/0406076
- [Kno00] G.F. KNOLL: "*Radiation detection and measurement*", 3<sup>rd</sup> edition, John Wiley & sons (2000)
- [Kop05] S. KOPP: "*The NuMI neutrino beam at Fermilab*", in the Proc. of 2005 IEEE Part. Accel. Conv. (Knoxville, TN), May, 2005 [arXiv:physics/0508001]
- [Kro07] K. KRÖNIGER, MPPMU, *private communication*
- [Lan07] J.-C. LANFRANCHI, *private communication*
- [Las06] T. LASSERRE AND H.W. SOBEL: "*Reactor neutrinos*", Comp. Rend. Phys. **6** (2005) [arXiv:nucl-ex/0601013]

- [Led78] C.M. LEDERER AND V.S. SHIRLEY (ED.): "*Table of isotopes*", 7<sup>th</sup> edition, John Wiley & sons (1978)
- [Min07] MINOS COLLABORATION: "*Preliminary results from MINOS on  $\nu_\mu$  disappearance based on an exposure of  $2.5 \cdot 10^{20}$  120 GeV protons on the NuMI target*", arXiv:0708.1495v2 [hep-ex]
- [Nov05] NOVA COLLABORATION: "*NuMI Off-axis  $\nu_e$  Appearance Experiment*", arXiv:hep-ex/0503053
- [Obe92] L. OBERAUER AND F. VON FEILITZSCH: "*Neutrino oscillations*", Rep. Prog. Phys. **55**, 1093 (1992)
- [Obe06] L. OBERAUER: "*Search for  $\vartheta_{13}$  with reactor experiments*", Prog. Part. Nucl. Phys. **57**, 127 (2006)
- [Obe07] L. OBERAUER, *private communication*
- [Oya05] Y. OYAMA: "*Results from K2K and status of T2K*", arXiv:hep-ex/0512041v2
- [PDG90] PARTICLE DATA GROUP: "*Review of particle physics*", Phys. Lett. B **239**, 1 (1990)
- [PDG07] W.-M. YAO ET AL.: "*Review of particle physics*", J. Phys. G **33**, 1 (2006) [<http://pdg.lbl.gov>]
- [Sch95] P. SCHMÜSER: "*Feynman-Graphen und Eichtheorien für Experimentalphysiker*", 2<sup>nd</sup> edition, Springer, Berlin, Heidelberg (1995)
- [Sch97] N. SCHMITZ: "*Neutrinophysik*", Teubner Studienbücher, Stuttgart (1997)
- [Ste07] X. STEEMANN, faculty for chemistry of the LMU, *private communication*
- [Sue04] F. SUEKANE ET AL.: "*An overview of the KamLAND 1-kiloton liquid scintillator*", arXiv:physics/0404071v2
- [Svo99] R. SVOBODA, <http://elvis.phys.lsu.edu/svoboda/superk/sun.gif>
- [Vog99] P. VOGEL AND J.F. BEACOM: "*The angular distribution of the neutron inverse beta decay,  $\bar{\nu}_e + p \rightarrow e^+ + n$* ", Phys. Rev. D **60**, 053003 (1999) [arXiv:hep-ph/9903554]

- [Voj95] P. VOJTYLA: "*A computer simulation of the cosmic-muon background induction in a Ge  $\gamma$ -spectrometer using GEANT*", Nucl. Instr. Meth. B **100**, 87 (1995)
- [Wei74] S. WEINBERG: "*Recent progress in the gauge theories of the weak, electromagnetic and strong interactions*", Rev. Mod. Phys. **46**, 255 (1974)

# Danksagung

n dieser Stelle möchte ich mich bei all denjenigen bedanken, die einen (größeren oder kleineren) Teil zum Gelingen dieser Diplomarbeit beigetragen haben. An erster Stelle bedanke ich mich bei Prof. Franz von Feilitzsch für die freundliche Aufnahme am Lehrstuhl E15 und die interessanten Diskussionen mit ihm, auch über Themen, die über die Physik hinausgehen. Die Arbeit am Lehrstuhl und die zahlreichen Reisen im Rahmen des DOUBLE CHOOZ Projekts haben mich nicht nur physikalisch weitergebracht.

Meinem Betreuer Prof. Lothar Oberauer danke ich für die Möglichkeit, diese Arbeit anfertigen zu können. Seine Anregungen und Vorschläge zu allen möglichen physikalischen Problemstellungen und Details haben die vorliegende Arbeit entscheidend bereichert. Auch werden mir die zahlreichen lustigen Anekdoten aus der Welt der Physik und der Berge in guter Erinnerung bleiben.

Ein weiteres großes Dankeschön geht an Dr. Walter Potzel, der durch seinen nimmermüden Einsatz (trotz seiner vielen weiteren Verpflichtungen), sein weitreichendes Hintergrundwissen und nicht zuletzt durch seine sehr gründlich durchgeführten Korrekturen maßgeblich zum Gelingen meiner Diplomarbeit beigetragen hat.

Ebenfalls fürs Korrekturlesen und einige interessante Anregungen bedanke ich mich bei Dr. Marianne Göger-Neff. Und natürlich auch für die schönen Tage rund um die Meetings in Madrid und Chooz.

Meinen Bürokollegen Patrick Pfahler, Achim Gütlein und Nils Haag danke ich für die exzellente Zusammenarbeit, die kleinen und großen Verbesserungsvorschläge zu meiner Arbeit und ihren Hilfen mit diversen Computerprogrammen (Achim: C++ und root, Patrick: solidworks). Besonderes Lob geht an dieser Stelle an Patrick für seine Geduld bei den endlosen Fußballdiskussionen, die ich mit dem Achim führen musste.

Beim Thema Computerprogramme muss ich mich natürlich auch bei Teresa Marrodán Undagoitia für die Einstiegshilfen und Tipps zu GEANT4 bedanken.

Dank geht generell an alle "Neutrinos" (Michael Wurm, Jürgen Winter, Timo Lewke, Quirin Meindl, Teresa, Patrick, Achim und Nils) nicht nur für die ein oder andere fachliche Hilfe, sondern vor allem auch für die zahlreichen

Aktivitäten abseits der Physik, sei es nun Kickern, Fußballspielen, Schaffkopfen, Filme schauen, Baden gehen oder einfach nur über Gott und die Welt plaudern. Jürgen bekommt einen ganz besonderes Dankeschön für die tollen Tage, die wir zusammen auf der Krim verbracht haben.

Den "Kryos" Dr. Jean-Côme Lanfranchi, Sebastian Pfister, Sabine Roth, Wolfgang Westphal, Chiara Coppi, Christian Isaila und Christian Ciemniak danke ich für die allseits gute Zusammenarbeit (v.a. Sebastian und Sabine im UGL) und die prima Stimmung am Lehrstuhl. Ebenfalls eine sehr gute Zusammenarbeit im UGL hatte ich mit Dr. Georg Rugel und Ursel Heim, auch hierfür danke.

Ein weiteres Dankeschön geht an Harald Hess, Erich Seitz und Thomas Richter, dem Team aus unserer Werkstatt, für die Hilfe bei allen mechanischen Problemen, sowie Hermann Hagn für die kompetenten Tipps und Tricks bei allen Fragen zur und rund um die Elektronik. Und natürlich auch an Norbert Gärtner für die Orientierungshilfen im Dschungel der Strahlenschutzvorschriften.

Eine ganz große Hilfe bei dieser Diplomarbeit waren mir unsere Sekretärinnen Beatrice van Bellen und Alexandra Földner, die mir unglaublich viel Arbeit beim Ausfüllen von diversen Formularen und beim Bewältigen von organisatorischen Sachen abgenommen haben. Hierfür, und natürlich für die Kekse, auch vielen Dank.

Einige "special thanx" gehen noch an...

- ... die DOUBLE CHOOZ Kollaboration für die freundliche Aufnahme in ihren Kreis
- ... Sandra Morawitz vom Strahlenschutz, die mir sehr schnell und unbürokratisch beim Ausleihen der Eichquellen geholfen hat
- ... Kathrin Hochmuth, für die netten Schaffkopfabende und das ein oder andere Fachgespräch. Nicht böse sein, dass aus mir kein Theoretiker geworden ist!
- ... den FC Bayern München, dass er mir stets einen Anlass dafür gegeben hat, unsere Bayernfans ein wenig zu ärgern
- ... Robert Hölzel vom E19 für seinen genialen Einfall zur Simulation von isotropen Quellen. Und auch für sein Engagement bei unseren Fußballnachmittagen.
- ... Claudia Baier, auch vom E19, für die Abwechslung im tristen S-Bahn-Alltag

- ... den Programmierer des Linux-Minigolfspiels "Kolf"
- ... Michael "Hans-Peter" Willers für die tolle E15-Homepage. Endlich ein Foto von mir im Internet!
- ... die Handballer der zweiten Männermannschaft des TSV Gilching-Argelsried, weil die Zeit im Training und bei den Spielen immer ein prima Ausgleich zum Alltag eines Physikers ist
- ... Achim Gütlein, damit er als einziger fünfmal in den Danksagungen erwähnt ist und somit nicht neidisch auf den Xaver sein muss (siehe [Ste07])
- ... alle meine Freunde und Bekannten
- ... und natürlich alle Sponsoren des Kickerspiels

Der letzte, aber vermutlich größte Dank geht an meine Familie, für ihre immerwährende Unterstützung in jeglicher Hinsicht während der ganzen Zeit (und auch fürs Korrekturlesen). Ohne sie wäre diese Arbeit sicherlich niemals zustande gekommen.

*Nothing shocks me.  
I'm a scientist.*

- INDIANA JONES